The Optical Sensor Mote: A novel device for enabling next generation Wireless Sensor Networks.

by

Hazem Abdul'Aal A. M. Awad

A Thesis

presented to the University of Strathclyde in fulfilment of the requirements for the degree of Doctor of Philosophy

in

Department of Electronic and Electrical Engineering

Centre for Intelligent Dynamic Communications

July 2013

Declaration

This thesis is the result of the author's original research. It has been composed by the author and has not been previously submitted for examination which has led to the award of a degree.

Hazem Abdul'Aal A. M. Awad July 2013

Dedication

To my dad and all my family

Acknowledgments

First, I would like to acknowledge and sincerely thank my two supervisors; Dr. Ivan Andonovoic and Dr. Trevor J. Hall, as well as Dr. Imad Hasan, Dr. Khaled Mnaymne, and Dr. Sawsan Majid who have helped, guided and inspired me throughout my doctoral studies. Their support, encouragement, and kindness have been instrumental in helping me to bring this work to life.

I would like to express my sincere thanks to the following people: Dr. Sofia Paredes for her guidance and with the WSN prototype, Tom Davies (Technix by CBS) for his outstanding help and support with CrystalWave (the primary photonic crystal modelling tool), Nic Oliveri (lab manager) for his great help in and out of the lab, Dan Deptuck and Patricia Greig (CMC), and my colleagues and friends: Dr. Robert Radziwilowicz, Erin Knight and others. I would also like to thank my former colleagues Hassan and Atousa Teimori and Dr. Degui Sun, Dr Mohamed Abdelalim, Dr Jeremy Upham, Huesein Kotob, and Zahirul Alam.

I would also like to express my sincere thanks to all my great friends and colleagues, in particular Ahmad Gharba, Ramy Waleed, Maysra Shams, Mohamed Syed, and many others for all the help, laughter, shared memories, support and encouragement.
Finally and most importantly, I wish to offer my most sincere and heartfelt thanks and gratitude to my amazing family: my father Abdul'Aal, my amazing siblings: Magid, Heba, and Marwa Awad, and my extended family for all their tremendous help, love, and encouragement thought my entire life.

Abstract

Recent advances in micro-electronics and communications have fuelled research in Wireless Sensor Networks (WSNs). WSNs are a collection of low power, low cost, small form factor devices referred to as sensor motes interconnected in a random manner to establish a network. Despite wide ranging research into a range of applications, significant limitations stand in the way of utilizing WSNs to monitor large scale/area environments.

Optical sensing techniques are well suited for monitoring a large variety of environmental variables such as temperature, pressure, humidity, and gas concentrations. However, traditional optical sensing techniques rely on bulky solutions including spectroscopic equipment and fibre based approaches. On the other hand, photonic crystals have caused a revolution in integrated optics as they allow functionalities not possible before; however little has been reported on their use as integrated optical sensors.

The research work combines the diverse but related fields of WSNs, integrated optics, and Photonic Crystals. A novel platform, the optical sensor mote, is proposed and its key building blocks are experimentally demonstrated as a feasibility study. Specifically, multi-gas sensors based on the slow light phenomenon in photonic crystal waveguides are theoretically and experimentally demonstrated. These sensors can sense multiple gases without the need of any physical changes. They can also be integrated with electronics to yield an optical sensor mote of small form factor which is stable, multi-functional, and cost effective.

The optical sensor mote represents a significant step towards enabling the wide spread use of WSNs to monitor large scale/area environments and providing a highly integrated mote platform amenable to mass production and providing multi-functions.

Table of Contents

Chapter 1 Introduction

1.1 Background

Sensors are everywhere and are a fundamental part of life. Sensors play a critical role in all aspects of living organisms. The five senses that most humans enjoy are enabled by extremely sophisticated biological sensors. A sensor can be defined as a device that responds to a physical stimulus (as heat, light, sound, pressure, magnetism, or a particular motion) and transmits a resulting impulse (as for measurement or operating a control). Sensors are often closely associated with actuators. An actuator can be defined as a device for moving or controlling something.

Humans have created a variety of sensors to aid them in their life. Indeed, the topic of Sensors is very vast and a large variety of sensors have been developed over time. Often, sensors are classified according to their sensing mechanism, e.g.: mechanical, biological, chemical, electrical, electronic, and optical to name a few. Within these general classifications, many sub classifications exist as well.

In the sensor field, optical sensing techniques (and optical sensors) are ubiquitous. They are used in a very wide variety of sensing applications including automotive, military, avionics, environmental and biomedical applications to name a few [Giancarlo et al. 2009]. Optical sensors can be generally classified into two categories: 1. Free space sensors (which find wide applications in the areas of spectroscopy and interferometry), and 2. Guided wave based sensors. Guided wave

sensors can further be sub divided into: 2.1) Fibre based optic sensors and 2.2) Integrated optic sensors.

While free space optical sensors were among the first optical sensors to be developed and utilized effectively, they suffer from critical issues that limit their sensing applications, particularly the limitations of line of sight and stringent alignment requirements. These issues make them particularly susceptible to external environmental perturbations which often affect the sensing operation.

Guided wave sensors do not suffer from the limitations of their free space counter parts and have a number of inherent advantages including: immunity to electrical and electromagnetic interference, flexibility in deployment (due to their small size and guided nature), ruggedness (e.g. in resisting ionizing damage), and ease of interface with optical communication systems [Giancarlo et al. 2009] .

The basic principle behind optical sensing with guided wave sensors is as follows: light radiation that is trapped within the dielectric medium of an optical waveguide responds to/is modulated by perturbation in the external environment (e.g. temperature changes, gases, mechanical stresses and strains…etc). The resulting effects of such external perturbation on the guided light radiation can often be used to draw meaningful information about the perturbations themselves, in essence, leading to the sensing of these external perturbations. The external perturbations modulate the guided light in different ways, the most common being: amplitude

(intensity) modulation, phase modulation, wavelength modulation, and polarization modulation.

Fibre optic sensors are currently the most dominant and well developed form of guided wave sensors. This is mainly attributed to the significant research and development that fibre technology underwent (particularly to achieve very low attenuation characteristics) for use in telecommunication applications and the uniqueness of the development platform (fibres for telecommunication and sensing applications are often made mainly from pure silica cores). This uniqueness (which can also be viewed as lack of options from a material perspective) actually helped focus the majority of the research efforts on producing very high quality and pure silica which in turn accelerated the development of fibre technology for telecommunication, and later, sensing applications. Furthermore, speciality fibre and fibre structures for sensing has been developed such as Photonic Crystal Fibres (PCF) and Long Period Optical Fibre Grating sensors (LPFG). Fibre optic sensors have been developed to sense a variety of parameters: temperature, stress and mechanical strains (e.g. for bridges and other infrastructure), biochemical detection of gases and containments (e.g. in drinking water) to name a few.

The biggest draw back of fibre optic sensors is their size or more appropriately, their bulky nature. This makes them difficult and costly to install and deploy as they have to laid-out over the area to monitored (e.g. bridge) and limits their ability to be networked (to form a network of sensors). Furthermore, fibre optic sensors do not lend themselves well to integration with other electronic systems (which may be

used for information processing) and only discrete integration is possible which leads to bulky sensor solutions.

The aforementioned issues severely limit the application of fibre sensors in sensing applications that require the monitoring of large scale areas. Examples include farm monitoring (of both crops and cattle), mine monitoring (for dangerous build-up of gases), forest monitoring (e.g. for fires) and so on. Integrated optical sensors provide an alternative to fibre sensors in these types of applications (and potentially other applications). There exists however, commercial fibre optics products based on spectroscopic gas sensing technologies that have been successfully applied to distributed sensing [OptoSniff]. These approaches utilize fibre cables to transmit data from a large number of sensing points and provide real time and highly accurate sensing capabilities of hazardous gases (methane and natural gas).

Integrated optic sensors operate using the same principle as their fibre sensors cousins. They have, however, developed at a slower pace and for (initially) a different set of applications. In particular, one of the main motivations for the development of integrated optics was for use in multi functional circuits (which may contain electronic components or be all-optical circuits). These circuits will be chip size (i.e. a few cm or mm in dimension) and hold great promise for a wide array of applications such as lab-on-chip and large scale (optical) sensor networks.

Integrated optics however, suffer from an interesting dilemma. Unlike fibre optics which really has only one main material fabrication platform (i.e. high purity silica),

there are many material options for integrated optics (and integrated optic sensors). Some of these material fabrication platforms include: Silicon over Silica (Si over SiO_2), Indium Phosphide (InP), Gallium Arsenide (GaAs), polymers, and even liquid crystals. Furthermore, currently, none of the available material fabrication platforms have achieved dominance yet as the most favourable platform. Such a wide array of material choices led to a slower progress in the field of integrated optics compared to fibre optics while simultaneously offering a great deal of flexibility and a much wider range of applications (including sensing).

Integrated optical sensors have a number of inherent advantages over their fibre optic cousins including: much greater flexibility (thanks to greater material choices), very small size (which makes them ideal for monitoring of large scale areas), and very importantly, the potential for integration with other electronic (or even optical) processing elements. That last point is of great importance because it opens the door for the formation of a wireless network of (optical) sensors nodes/motes more commonly called wireless sensor networks (WSN).

The research is a study into the viability of a specific family of integrated optic sensors -photonic crystal refractive index (RI) sensors – and a characterisation of a new subclass referred to as ‘slow light RI’ based sensors. The sensors offer the potential for new performance advantages and may complement the currently dominant form of optical sensors for chemical and biological detection based on spectroscopy [Pergande et al. 2011; Passaro 2013].

There are several slightly different definitions of a sensor mote [Sensor Mote a], [Sensor Mote b], [Sensor Mote c]. The following general definition is adapted: “A sensor mote/node is a node in a wireless sensor network that is capable of performing some processing, gathering sensory information and communicating with other connected nodes in the network.” [Sensor Mote d]. The sensor mote forms the building block of WSN which are of increasing importance in the area of sensing.

WSN find many current applications in sensing. In particular, WSN are well suited for environmental monitoring of large scale areas including: forest fires, landfills, farms and cattle, structural monitoring (e.g. bridges, ships, and Aircraft), Air pollution (including monitoring of build up of dangerous gases in areas such as mines), military and civilian security, and so on [Hall 2009a; Hall 2009b; WSN Applications a; WSN Applications b]. Furthermore, WSN can include actuators as well as sensors and so have the ability to monitor and manipulate the environment (e.g. in industrial quality and control applications).

It can be argued that the big push in research and development of WSN is actually one of the manifestations of humans to understand and manipulate their environment to be more suitable for them or to achieve a certain set of outcomes. WSN are enabled by many factors including: great advances in miniaturization of electronic components, advances in miniaturized sensors (including integrated optic sensors), and the rise of various communication protocols for the monitoring, analyzing and processing of the sensor data (e.g. ZigBee).

Despite the advances in WSN, several important issues remain which limit their viability [Benini et al. 2006]. Some of these issues include: communication protocols shortcomings, hardware issues, and safety issues. The issue that concerns us the most in this research work however is the sensor mote itself. Specifically, the lack of an appropriate sensing mechanism that is suitable for efficient and accurate monitoring of a large class of important environmental phenomena (with the often additional requirement of large scale / wide area monitoring). In fact, the primary motivation of WSN is the monitoring of large scale / wide areas.

As stated earlier, optical sensing mechanisms are often among the most suitable for the monitoring of various environmental conditions (e.g. temperature, pollution, biological and chemical pollution). It therefore makes a great deal of sense for the sensor mote (which forms the building block of the WSN) to utilize optical sensing as its primary sensing mechanism. Currently however, this is not the case.

Therefore, it is proposed that *the* missing piece to overcoming some of the most critical shortcomings of WSNs is the optical sensor mote: a sensor mote that uses optical sensing as its primary sensing mechanism. Such an optical sensor mote is what this research work discusses.

1.2 Motivation

The preceding section makes it clear that improving the sensor mote itself (primarily, by using optical sensing mechanisms) is a potentially powerful approach to overcoming some of the main challenges that WSNs currently face and significantly

improving their capabilities and adoption. Ideally however, any improvements to the sensor mote itself would NOT take away from its current advantages which include: small size (or foot print), low cost of manufacturing, ease of mass production, ability to communicate with other motes using wireless RF technology (which is critical for cost effective deployment over a wide area), and signal processing capabilities. The biggest drawback of current sensor motes is their sensing mechanisms which are primarily not based on optics.

Purely optical approaches were initially investigated for the sensor mote. That is, the sensing, transmission, and even signal processing will take place in the optical domain. In essence, it was wished to extend the concept of optical wireless [Heatley et al. 1998] to the WSN domain. In essence, the purely optical approach to the sensor mote would be similar to the concept of optical wireless networks but specifically tailored to environmental sensing as opposed to some of the more common applications of current optical wireless research such as cellular over optical wireless networks [Katz et al. 2006].

It was quickly discovered however, that there are many challenges currently facing optical wireless systems in general. Furthermore, these issues increase when applying and extending optical wireless concepts to the WSN domain. This is mainly due to greater and more stringent requirements for the optical sensor mote, especially the signal processing which will have to take place in the optical domain and such technology, while currently existing in various forms [Awad 2006], is still in its infancy and not practical for real world applications.

Furthermore, current optical wireless networks are plagued with issues related to path loss and alignment (to ensure line of sight operation). Additionally, the workarounds to the line of sight challenges are *challenging* in of themselves, particularly, when it is desirable to allow the sensor motes to communicate with each other while monitoring, say livestock, forest fires, or even mine conditions (all of which happen to be attractive WSNs applications). It quickly became clear that alternative approaches are required to actually create an optical sensor mote that solves the basic needs.

1.2.1 The Optical Sensor Mote

Based on the previous sections, the concept of the optical sensor mote is proposed. This is a sensor mote that is similar to currently available sensor motes but makes use of integrated optic sensors as its primary sensing mechanism while keeping all other features the same as current sensor motes (including, using RF for communication and electronics for signal processing).

In essence, the proposed optical sensor mote is based on the (hybrid) integration of integrated optics and electronics technologies on the same chip/wafer [Rubenstein et al. 2011; Wada 2008]. Each technology shall be utilized where it is best suited: RF for wireless transmission (between the sensor motes), electronics for storage and signal processing, and integrated optics for sensing and combine these technologies into a wireless enabled optical sensor mote. This solves the major problem of path loss and line of sight requirements (which plague optical wireless systems) and allows for ease of deployment since there is no longer a need for sophisticated and

costly line of sight systems (e.g. for tracking and alignment). Furthermore, optical sensing is utilized for environmental monitoring of the phenomena over a large scale/wide area (e.g. gas concentrations in mine, forest fires…etc).

1.3 Objectives

The original objective of this research work was a "full" demonstration of an optical sensor mote. More specifically, the goal was the physical demonstration of both the RF communication side and the optical sensing side of the mote (these two sides form the main functionality of the sensor mote and the WSN). Additional functionalities such as signal processing electronics, packaging, storage and others are already well demonstrated in practice and no attempts to reproduce them in this research were carried out.

Due to severe difficulties in the first fabrication run of the optical sensor prototype (outlined in Chapter 3), which were due to errors on the fabrication side (specifically, the company that fabricated the chips missed a critical fabrication step which rendered the sensor useless), the objectives of the research work were scaled back to the partial demonstration of an optical sensor mote. Specifically, the demonstration of the optical sensing component of a sensor mote and the communication component between sensor motes. Furthermore, it is desirable to ensure that both (separate) experimental demonstrations are fabricated from materials that can practically be (hybrid) integrated together to form an actual, single chip which form the proposed optical sensor mote. This is a critical step to proving that such an

optical sensor mote can be built in practice (even though such a full demonstration is not carried out in this research work).

The objectives of this research work is thus summarized as follows:

- Selection of a potential Wireless Sensor Network application to help in the design of the optical sensor mote.
- Review of basic wireless sensor networks and protocols and the selection of a specific protocol.
- Hardware demonstration of a basic WSN using the selected communication protocol and off-the-shelf components.
- Selection of an appropriate optical sensing mechanism to be used in the optical sensor mote.
- Theoretical and experimental demonstration of the optical sensing mechanism.

1.4 Summary of Contributions

The following contributions can be identified as arising from the research:

- Experimental demonstration of a basic Wireless Sensor Network using Zigbee communication protocol and Texas Instruments CC2430 ZigBee Chipset
- Proposal and theoretical investigation of a Silicon-On-Insulator (SOI) Multi-Gas Photonic Crystal (MG-PhC) Sensor.

- Theoretical investigation of enhancing the Q-factor of the SOI MG-PhC Sensor.
- Experimental investigation of the SOI MG-PhC Sensor. Identification of failure causes.
- Proposal and theoretical investigation of an Indium Phosphide (InP) Multi-Gas Photonic Crystal (MG-PhC) Sensor.
- Theoretical investigation of enhancing the Q-factor of the InP MG-PhC Sensor.
- Brief theoretical comparison in basic performance between the SOI and InP MG-PhC Sensors.
- Proposal, introduction, and experimental investigation of a new class of photonic crystal sensors: the slow light refractive index (RI) photonic crystal sensors in InP.
- Theoretical investigation of SOI and InP slow light RI sensors and comparisons of their performance. Theoretical proof of superior sensitivity of SOI over InP sensors.
- Theoretical investigation of the effect of Air hole radius on sensor sensitivity in InP sensors.
- Experimental verification of shift in slow light regime of a photonic crystal gas sensor due to presence of gas.
- Proposal of a wireless enabled Optical Sensor Mote for Gas Sensing. Experimental verification of its two main components: communication protocol and optical sensing.

1.4.1 Publications

At the time of writing of this thesis, the following works have been published:

- Ronald Millett, Hazem Awad, Maxime Poirier, Valery Tolstikhin, Trevor Hall, Karin Hinzer, and Henry Schriemer, "Design and Fabrication of a λ/4 Phase-Shifted 1310 nm Laterally-Coupled Distributed-Feedback Laser," CLEO 2008, San Jose, CA, May 4-9, 2008.
- Hazem Awad, Imad Hasan, K. Mnaymneh, Sawsan Majid, Trevor J. Hall, Ivan Andonovic, "Wireless enabled multi gas sensor system based on photonic crystals," SPIE Photonics Europe 2010, Brussels, Belgium, April 12-16, 2010.
- Hazem Awad, Imad Hasan, K. Mnaymneh, Trevor J. Hall, and Ivan Andonovic, "Gas Sensing using Slow Light in Photonic Crystal Waveguides", 7th workshop on Fibre and Optical Passive Components (WFOPC), Montreal, Canada, 2011, pp. 1-3.

1.5 Structure of the Thesis

This thesis is organized into four chapters. Chapter 1 provides the introduction, motivation, defines the overall structure of the thesis, introduces the important concept of the optical sensor mote, and lists the major accomplishments (including the original contributions). Chapter 2 introduces the problem of gas monitoring in mines and proposes the utilization of Wireless Sensor Networks (WSNs) to solve it and introduces the Texas Instrument CC2430 ZigBee chip, a non optical but standard, sensor mote and discusses the implementation of a representative WSN

that is designed to monitor and control the temperature of an environment. Chapter 3 discusses Photonic Crystals basic theory and suggests them as strong candidates for the optical sensing mechanism of the proposed optical sensor mote. It introduces three novel photonic crystal multi-gas sensors and provides theoretical and experimental investigations of their properties and operation. Chapter 4 concludes the thesis and offers additional suggestions for future work.

Chapter 2 Optical Sensor Mote: Wireless Sensor Networks for environmental monitoring

2.1 Background

As discussed in Chapter 1, Wireless Sensor Networks (WSNs) are finding an increasing number of applications in a variety of fields. In particular, WSNs are well suited for sensing applications that require a distributed approach. Such an approach is often needed to monitor large scale/area environments or in situations where a wired approach is difficult or not cost effective. Furthermore, WSNs continue to decrease in cost thanks to continuous advances in electronics manufacturing which lowers the costs of sensor motes, the building blocks of WSNs.

Another important and very valuable feature of WSNs is their ability to incorporate actuators along with their sensors. This gives them the ability to not only monitor an environment, but to control and manipulate it as well. This is invaluable in almost all fields particularly in industrial control applications.

WSNs are made up of a several sensor motes/nodes. The number of such motes can range from a few to thousands. Each sensor mote has several capabilities including: communication with other motes, sensing, power and energy harvesting, and possibly control through microcontrollers. A WSN will have one or more base stations or master motes. These master motes have greater capabilities than the other motes that make up the WSN and serve as the “brain” of the WSN helping organize

the other motes as well as gateways between the motes and the end user [WSN Applications a].

WSNs were originally developed for military applications to help monitor battlefield conditions. They have since been successfully utilized in various environmental applications including: oceans, volcanos, Air pollution, and greenhouse effect monitoring as well as forest fire detection. Other application areas include machine health monitoring in factories, structural monitoring (e.g. bridges, buildings), water quality monitoring, landfills and waste monitoring, and agricultural applications (e.g. monitoring of crop fields and live animals) [WSN Applications a]. WSNs also find applications in the new research area of smart homes and their management, e.g. interconnectivity between different home appliances with the internet and smart energy management.

WSNs are still a relatively new research area and thus a variety of communication standards exist to facilitate communication between the motes that make up the WSN. This means that most WSNs are incapable of communicating with other WSNs or with other standard systems (e.g. existing computer networks). It is believed that as WSNs develop further, fewer and fewer standards will emerge and an eventual dominant standard will be adopted. The most common WSN communication standards are: 1. WirelessHART, 2. ISA 100, 3. IEEE 1451, and 4. ZigBee / 802.15.4 [WSN Applications a].

2.2 ZigBee Standard

ZigBee is a wireless mesh network communication standard designed for small, low cost, and low power devices. It is based on the IEEE 802 standard for personal area networks and is specifically designed for RF applications that require low data rate, long battery life, and secure networking. ZigBee's defined data rate ranges from 60 to 250 kbps and is best suited for periodic or intermittent data communication [ZigBee]. Various companies (currently numbering over 200) have come together and formed the ZigBee Alliance to maintain and publish the ZigBee standard [ZigBee a].

The ZigBee protocols are based on ad-hoc algorithms which allow it to automatically build a low speed network of nodes. In essence, ZigBee can be used to quickly and easily build a low speed, and low power WSN. ZigBee supports 3 types of motes/nodes, also called ZigBee devices: 1. ZigBee Coordinator, 2. ZigBee Router, and 3. ZigBee End Device [ZigBee].

The ZigBee Coordinator is the most capable device in the ZigBee standard and serves as the master node in a ZigBee network. It forms the root of the network tree and stores all necessary information that allows the network to function correctly and securely. There is always only 1 ZigBee Coordinator per ZigBee network.

The ZigBee Router acts as an intermediary node that routes data and commands between various nodes in a ZigBee network. It is also capable of performing other functions and running applications. Some routers have the capabilities of ZigBee

Coordinators and can serve this function in the event that the original coordinator of the network has failed or ceased operation for any reason. This aids the self-healing process of a ZigBee network [Qiu et al. 2007].

The ZigBee End Device is a node with a basic set of functionalities that allow it to talk to its parent node (in the network tree) as well as run basic functions such as sensing, power and energy harvesting, and possibly very simple control functions. It cannot relay data from other devices in the network. It is often asleep or dormant for most of the time and therefore has a long battery life and is often very cheap to produce.

The ZigBee standard is well suited as a communication standard for WSN applications that monitor large scale/area environments. It is self organizing and designed for low cost, low power, and large number of nodes. It is also very capable yet flexible and easy to utilize. Furthermore, it is currently among the most popular WSN communication standards and a variety of vendors support it and manufacture off the shelf nodes that run the ZigBee standard and are low cost.

One of the objectives of the research was to demonstrate the communication side of the proposed optical sensor mote by building a simple WSN that monitors an environment and manipulate it as needed. The ZigBee standard is chosen as the communication protocol for the WSN.

2.3 WSN Application: Gas monitoring in mines

Mining is an ancient human activity that dates back to prehistoric times. Speaking broadly, mining refers to all extractions of any non-renewable sources [Mining]. Safety has long been a primary issue and concern with mining and modern practices have significantly improved safety in mines. However, mining accidents continue to occur on a regular basis world wide.

As an example, between 2001 and 2005 there were over 31,064 deaths in coal mines in China alone, averaging 17 deaths per day. These fatalities were due to mine explosions and despite that the fact that massive investments have been made in safety of such mines, serious accidents continue to occur and many lives are lost as a result [Liu et al 2009a]. Since 1839, there have been 501 coal mine explosions in the United States that killed at least 5 people each [Coal Mines]. The main causes of mine fatalities are: 1. Methane explosions, 2. Flooding, 3. Fires, and 4. Structural collapse.

Methane explosions are one of the leading causes of mine explosions and fatalities. Methane is a by product of coal and is combustible. Mixtures of about 5 to 15 % of methane in Air are prone to explosions [Coal Mines]. When a methane build up comes into contact with a heat source and there is not enough Air to dilute methane to levels below its explosion point, a methane explosion occurs. Furthermore, it takes little heat to ignite the methane combustion process which gives a methane explosion the ability to accelerate very fast leading to more catastrophic consequences.

WSNs present a new and unique to monitor mines and significantly increase their safety. WSNs can monitor the entire mine area much more effectively and cheaply than a wired solution and are far more convenient to deploy while having a longer service life. Additionally, their distributed nature allows for functionality that a wired solution cannot match, e.g. providing a complete mapping of hazardous gas concentration in a particular mine in real time [Liu et al 2009a; Liu et al 2009b].

There is growing research and commercial interest in utilizing WSNs to monitor mines and underground structures (e.g. pedestrian and water tunnels). [Feng and Jiangfeng 2010] proposed the use of a WSN consisting of Texas Instrument CC2430 ZigBee sensor mote to monitor coal mines. The sensor motes however, are completely electronic and chemical in nature and are thus limited to detecting a single gas, in this case, methane.

[Niu et al. 2007; Tümer and Gündüz 2010] demonstrated WSN systems to monitor methane concentration and leaks in underground coal mines. These systems utilized ZigBee as the communication protocol for the WSN. [Bandyopadhyay et al 2009] developed a WSN that monitors the location of miners and their equipment in order to increase the efficiency of the mining operations and to pinpoint the miners' precise location in disaster situations. [Wang et al. 2007] utilized a WSN to monitor the structural integrity of underground coal mines with great success and much lower cost than existing wired systems. Additional research effort in this growing area continues to take place.

2.4 A basic WSN for environmental monitoring

2.4.1 Background and objective

Initially, the goal was to demonstrate a basic WSN that would monitor gas levels in an environment and have emulated capabilities of controlling the environment (e.g. activate an alarm for dangerous gas levels). This would serve as a demonstration of the communication side of the proposed optical sensor mote. However, at the time of the development of the WSN prototype, the photonic crystal gas sensors (discussed in chapter 3) were not yet developed nor was there access to appropriate equipment to perform gas measurements.

However, access was available to the Texas Instrument (TI) CC2430 ZigBee sensor mote which had been successfully used to create several WSN prototypes [Tümer and Gündüz 2010; Xianli et al. 2011]. Furthermore, the TI CC2430 had on-board temperature sensors and it could be taken advantage of [TI CC2430]. Therefore, a WSN prototype was developed that monitors the temperature of an environment (and ensure that power/energy demands are not exceeded) instead of the gas level.

The WSN prototype serves to illustrate several important points regarding WSNs: 1. they can be used to monitor an environment effectively, 2. they can manipulate the environment to a set of desired conditions, 3. all of this can be done much more cheaply and effectively than a wired approach.

2.4.2 Introduction to WSN

The WSN consists of two TI CC2430 evaluation boards, called SmartRF04EB (Figure 1): 1. the first SmartRF04 acts as an *outdoor* sensor mote, and 2. the second SmartRF04 acts as an *indoor* sensor mote. The second SmartRF04 also acts as the *coordinator* (or master) node of the WSN and includes an emulated actuator to control the indoor temperature.

The developed WSN functions as a smart energy management solution for an environment (e.g. a home or factory) that it monitors. It provides the user with the ability to set the desired environment temperature that will be maintained by the WSN. Additionally, the WSN has an alarm called Peak Demand Alarm that represents a warning signal from an external entity (e.g. a utility company) to indicate that the peak power consumption limit is close to being reached. The WSN responds to this alarm by lowering the environment's temperature by some margin, regardless of user settings but while maintaining a minimum safe temperature for the environment.

The goal was to rapidly prototype a WSN and a number of pre-existing tools were utilized to help achieve this goal. The Texas Instrument CC2430 ZigBee chip is well suited for ZigBee applications as it is optimized for low power and has a number of excellent features, including: 1. a 2.4 GHz IEEE 802.15.4 compliant RF transceiver, 2. a 12-bit ADC with up to eight inputs and configurable resolution, 3. an onboard battery monitor, and 4. an on board temperature sensor [TI CC2430].

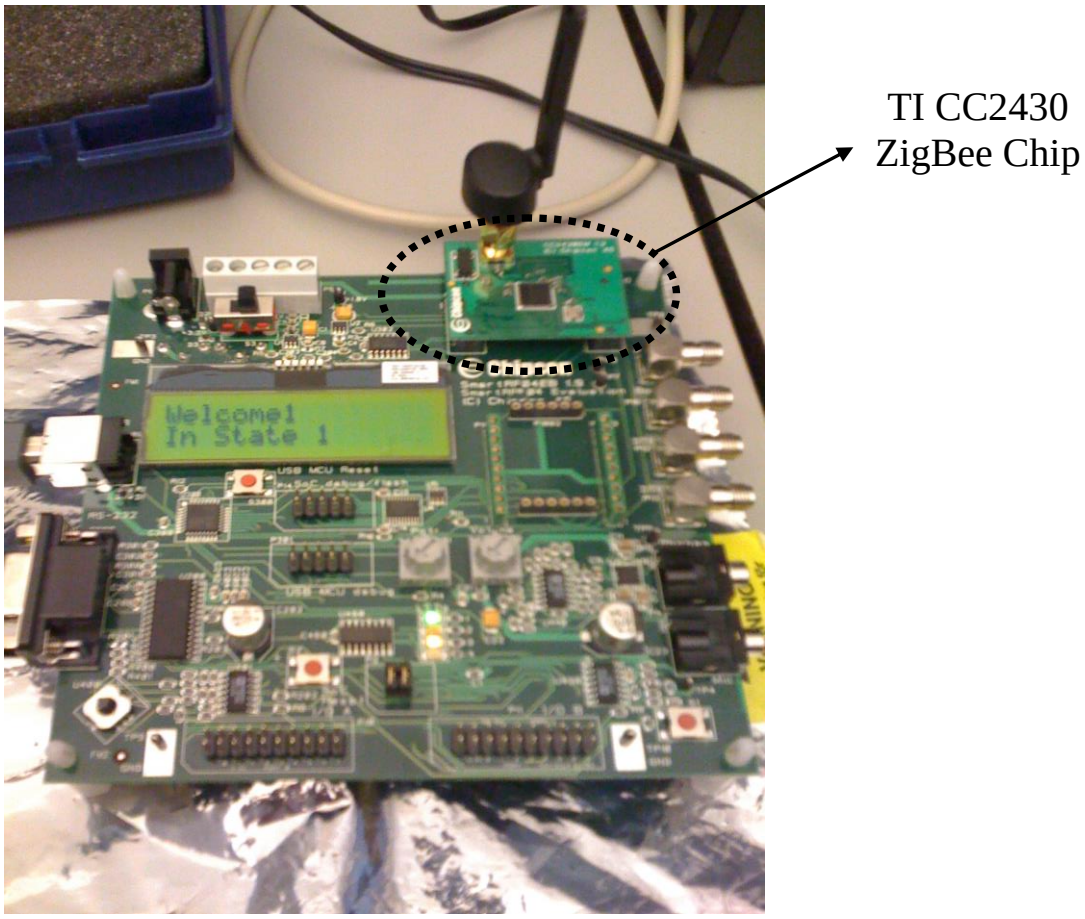

60

Figure 1: Texas Instrument evaluation board, SmartRF04EB, with a mounted Texas Instrument CC2430 ZigBee chip (dashed circle).

The IAR Systems's Embedded Workbench Integrated Development Environment (IDE), EW8051 was used as the main development and coding environment for the TI CC2430 chips [IAR EW]. Texas Instrument recommends EW8051 as the IDE of choice for most of its chips and its powerful features allowed us to quickly get acquainted with the TI CC2430 basic functions.

Texas Instrument produced the Z-stack, its own implementation of the ZigBee protocol stack [TI Z-Stack]. The Z-stack also comes with several sample applications designed for use with EW8051 IDE. One of these applications was called SimpleApp: it creates a basic WSN with ZigBee as its communication protocol.

A Finite State Machine (FSM) was programmed to the WSN. FSMs are well suited for modelling systems that can be in different states and change states due to some input, often called a transition [FSM].

FSM can be coded manually; however this process is prone to errors particularly as the number of states grows. Furthermore, manual testing of a FSM is often very difficult as the designer will have to manually test every single possible situation/state the FSM could be in. It is often better to use specific tools that aid in the design of the FSM and automate the process such as IAR Systems' visualSTATE. It is a highly visual tool; the designer builds the FSM by drawing out the state diagram and visualSTATE auto generates all the necessary code [IAR vstateTATE]. IAR's visualSTATE is well suited for the design of the FSM for the WSN: 1. it has powerful capabilities to perform full exhaustive tests (i.e. testing every possible state of the FSM) in a very short time, due to proprietary algorithms, 2. it is tailored for the design of embedded systems' FSMs where code size is a main constraint, and 3. it integrates well with IAR EW8051, the main IDE. visualSTATE was used to design the finite state machine of the WSN.

2.4.3 WSN implementation

The WSN implementation consists of hardware and software components as shown in Figure 2.

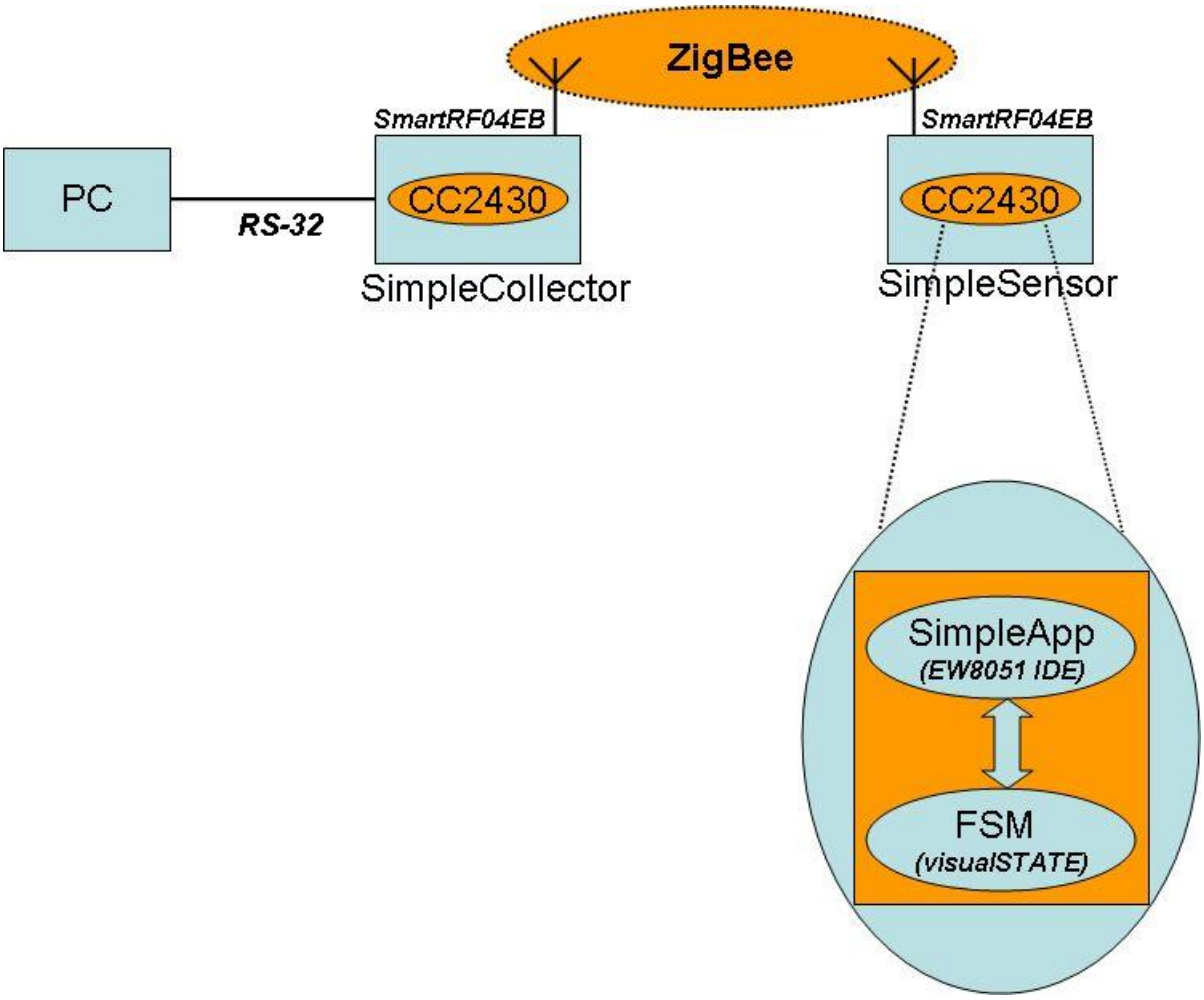

Figure 2: WSN Implementation block diagram showing the hardware and software components. RS-32 is a communication protocol between computers and external devices (e.g. evaluation boards).

2.4.3.1 Hardware

The WSN consists of two Texas Instrument (TI) SmartRF04EB evaluation boards. Each of these boards has a CC2430 ZigBee chip attached to it (Figure 1). Each of these CC2430 has a different ZigBee application profiles running on them: 1. SimpleCollector is the application profile for the ZigBee Coordinator (which serves as the brain of the WSN), and 2. SimpleSensor is the application profile for the ZigBee End device (which serves as the sensing node of the WSN). For simplicity, the WSN coordinator is referred to as SimpleCollector and to the WSN sensing node as SimpleSensor.

2.4.3.2 Software

From a software perspective, the WSN is divided into two main parts: 1. the SimpleApp application (coded using EW8051 IDE), and 2. the FSM (designed using visualSTATE).

SimpleApp is a ZigBee application that is part of the Z-stack, Texas Instruments implementation of the ZigBee protocol stack. As provided by Texas Instruments, SimpleApp has limited functionality: it simply forms the WSN ZigBee network and handles issues such as nodes binding to/or leaving the network as well as wirelessly transmit data from SimpleSensor to SimpleCollector (which optionally transmits the data to a PC or an external computer system).

The FSM adds additional functionality to SimpleApp. The FSM turns SimpleSensor into a smart sensor where additional operations, other than transmitting sensor data to SimpleCollector, can take place. SimpleApp was modified (using EW8051 IDE) in order to integrate the FSM code.

2.4.4 WSN Software: SimpleApp

SimpleApp is a ZigBee application designed by Texas Instrument and distributed as part of their Z-stack. It creates a simple WSN consisting of (at minimum): 1. a SimpleSensor, which acts as an end device/sensor node in the WSN, and 2. a SimpleCollector, which acts as the coordinator of the WSN (see Figure 2).

SimpleCollector forms the ZigBee network and performs all associated operations of node binding and dealing with dropped nodes and other ZigBee functions (e.g. security, interface to end user and external devices).

SimpleSensor performs several simple tasks including: 1. measuring the surrounding temperature using the CC2430 onboard temperature sensor, and 2. reporting the temperature measurement continuously to SimpleCollector.

2.4.4.1 Calibrating the CC2430 Temperature Sensor

The CC2430 has an onboard temperature sensor that is capable of measuring the temperature of the surrounding environment. The sensor however, should be calibrated regularly to ensure high accuracy of the measurements. There are different

calibration procedures; one of which is the 1-point calibration method which is the suggested method by Texas Instruments [TI DN102]. The error in the 1-point calibration method is ±2 °C which is acceptable.

The environment's temperature, T, as measured by the CC2430 sensor, can be given by this equation [TI DN102]:

$$T = \frac{Output\ voltage\ (mV) - Output\ voltage\ at\ \mathbf{0}^{\circ}C\ (mV)}{Temperature\ Coefficien\ t\ (mV/^{\circ}C)} \qquad (1)$$

Now, the following design choices are made for the CC2430 Analog-Digital Converter (ADC) parameters to aid us in evaluating Equation (1):

1. Set the ADC reference voltage to 1.25 V. This is convenient since there is an internal voltage supply of 1.25V in the CC2430 which can be used as the reference voltage and eliminates the need for an external reference voltage source. Also, the temperature ranges of interest can be achieved with the 1.25V internal reference voltage.
2. Set the ADC resolution to its highest value, 12 bits. The ADC value is always given in 2's complement, so for a 12 bit resolution, the maximum ADC value is 2^{11}=2047.

The output voltage of the CC2430 temperature sensor is given by [TI DN102]:

$$Output\ \ voltage_{temp\ \mathbf{sensor}} = ADC\,Value_{2's\,complement} \bullet \frac{reference\ voltage\,(mV)}{Max\ ADC\ value} \qquad (2)$$

However, the actual CC2430 chip may have an offset output voltage and therefore a 1-point calibration was performed to take that offset into account. It is easiest to perform the 1 point calibration at 25 °C.

The CC2430 offset output voltage is given by [TI DN102]:

$$Offset\ voltage_{CC2430}[mV] = Measured\ Output\ voltage\ at\ 25^{\circ}C\,[mV] - \left(Temp\ Coeff\ \ [mV/^{\circ}C] \bullet Temp\,[^{\circ}C] + Output\ \ Voltage\ at\ 0^{\circ}C\,[mV]\right) \qquad (3)$$

For the CC2430, the necessary parameters to evaluate equations (1) and (3) are given in [TI CC2430]: 1. output voltage at 0 °C = 743 mV, and 2. the temperature coefficient = 2.45 mV/°C

Recalling Equation (2), which gives the output voltage of the CC2430 temperature sensor at a given temperature (in this case 25 °C); Equation (3) can be rewritten as:

$$Offset\ voltage_{CC2430}[mV] = ADC\,Value \bullet \frac{1250\,(mV)}{2047} - (2.45 \bullet 25 + 743) \qquad (4)$$

Finally, Equation (1) is rewritten using Equations (2) and (3) to give the temperature reading of the CC2430 sensor:

$$T = \frac{Output\ voltage\,(mV) - \left(Output\ voltage\ at\ 0^{\circ}C\,(mV) + Offset_{CC2430}\right)}{Temperature\ Coefficien\,t\,(mV/^{\circ}C)} \qquad (5)$$

2.4.4.2 Example 1-Point calibration of a CC2430 chip, ID: 0BE4

An example of performing a 1-point calibration on the CC2430 chip that performs the SimpleSensor functions is given using the chip with a manufacture's ID of 0BE4. This calibration process was repeatedly performed throughout the prototyping of the WSN to ensure accurate temperature readings.

The $CC2430_{0BE4}$ ADC value at 25 °C = **1324**, which was found by displaying the contents of the chip's ADC register on the SmartRF04's (evaluation board that carries the chip) LCD (see Figure 1).

Now, using Equation (2):

$$Output\ voltage\ of\ sensor\ at\ 25℃ = 1324\ x\ (1250\ mV/2047) = 808.5\ mV \qquad (6)$$

And, using Equations (3) and (4):

$$Offset\ voltage\ of\ CC2430_{0BE4}\ at\ 25℃ = 808.5\ mV - (2.45\ x\ 25+743) = 808.5 - 804.25 = 4.25\ mV \qquad (7)$$

Finally, using Equation (5), the temperature of $CC2430_{0BE4}$ temperature sensor is calculated:

$$T_{CC2430_{0BE4}} = \frac{808.5 - (743 + 4.25)}{2.45} = 25\,°C \qquad (8)$$

I.e. the $CC2430_{0BE4}$ temperature sensor is now calibrated and set to 25 °C, the standard value for room temperature. This calibration process was verified by measuring the room temperature with an external sensor. The result was 25.5 °C which means that the $CC2430_{0BE4}$ temperature sensor reading had a 0.5 °C error, well within the margin of error of the 1-point calibration method. This concludes the 1-point calibration of the CC2430.

As shown in Figure 1, the FSM, which algorithmically models the WSN functionality, must be run by SimpleSensor; i.e. it needs to be activated from inside SimpleApp. This was successfully accomplished by integrating the FSM code (generated by visualSTATE) with the SimpleApp's software function that performs the temperature measurements and wirelessly transmits the results to SimpleCollector.

2.4.5 WSN Software: Finite State Machine (FSM)

The FSM consists of 3 main states (and 5 sub-states): 1. Startup State, 2. NormalOP State, and 3. PDemandOP state. Figure 3 shows the FSM state diagram. The FSM changes state based on external inputs. In the implementation, the external inputs are provided by a Joystick in the SmartRF04 evaluation board. External events such as

the Peak Demand Alarm were emulated by the same Joystick. Table 1 gives a list of external events and their corresponding Joystick positions.

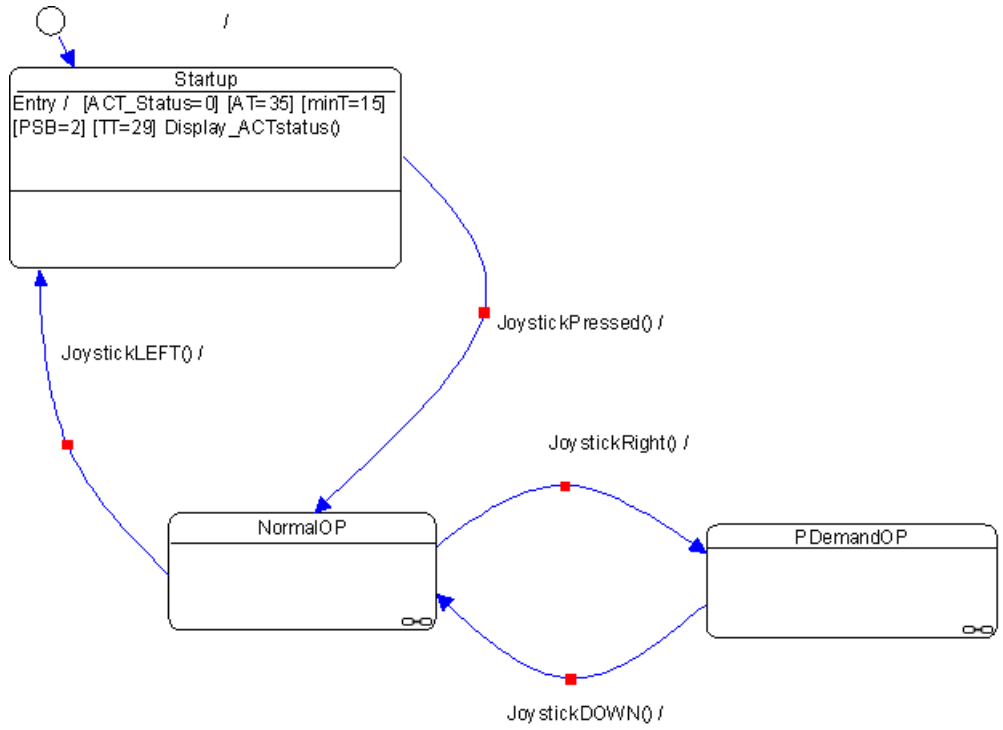

Figure 3: FSM State diagram showing all 3 main states of the FSM.

Table 1: List of external events simulated by the Joystick.

Event	Explanation
JoystickDOWN	Simulates the clearing of the Peak Demand Alarm (i.e. PDA = 0)
JoystickLEFT	Causes the FSM to return to Startup state, i.e. a reset for FSM.
JoystickPressed	Starts the FSM operation (after initialization has taken place).
JoystickRight	Simulates the presence of the Peak Demand Alarm (i.e. PDA = 1).

2.4.5.1 Startup State

The Startup State represents the initial state of the WSN. The FSM is initialized and all variables are set to their default values including:

1. ACT: the state (ON or OFF) of the emulated thermostat,
2. AT: the actual/current temperature of the environment,
3. PSB: the predefined set back point, i.e. the number of degrees Celsius the temperature must go down by when Peak demand Alarm (PDA) is ON,
4. TT: the target temperature and,
5. minT: the minimum safe environment's temperature. The thermostat must turn ON if minT is reached regardless of the presence of the Peak Demand Alarm.

2.4.5.2 NormalOP State

In the Normal Operation (NormalOP) state, the FSM is in the Normal Operation mode. This mode means that the Peak Demand Alarm (PDA) is OFF. The WSN maintains the environment's temperature by regularly performing temperature measurements and turning ON/OFF the emulated thermostat (variable ACT) as needed to maintain the target temperature (variable TT). Figure 4 shows the state diagram of the NormalOP state. NormalOP consists of two sub states; 1. Wait_NOP, and 2. Set_NOP_Timer.

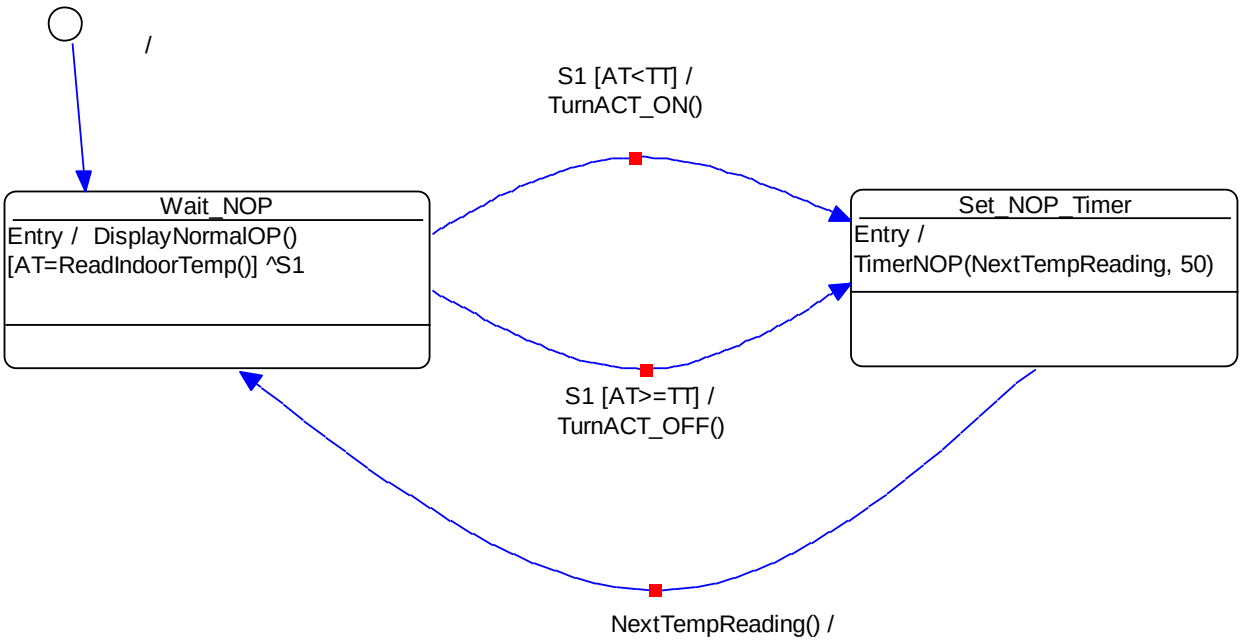

Figure 4: NormalOP state diagram showing its two sub states.

- ***Wait_NOP Sub state:***

Wait_NOP is the default state of the NormalOP state. In this state, the environment's temperature is measured using the CC2430 temperature sensor. The result is assigned to the variable AT (actual temperature) and displayed for the user on the SmartRF04's LCD. If AT is lower than the target temperature (TT), the WSN transitions to the Set_NOP_Timer state and the emulated thermostat is turned ON. If, on the other hand, AT is greater or equal to TT, the WSN transitions to the Set_NOP_Timer state and the emulated thermostat is turned OFF.

- ***Set_NOP_Timer:***

In this state a timer is set and once it expires, the WSN returns back to the Wait_NOP state and process continues until the Peak Demand Alarm is raised (i.e.

PDA = 1) at which point, the WSN transitions to PDemandOP state. The timer value is set to 50 milliseconds for illustration purposes.

2.4.5.3 PDemandOP State

In Peak Demand Operation (PDemandOP) state, the FSM is in the Peak Demand mode. The WSN transitions into this state whenever the Peak Demand Alarm (PDA) is ON. It maintains the environment's temperature according the rules of Peak Demand mode and disregards the user settings. Figure 5 shows the state diagram of the PDemandOP state.

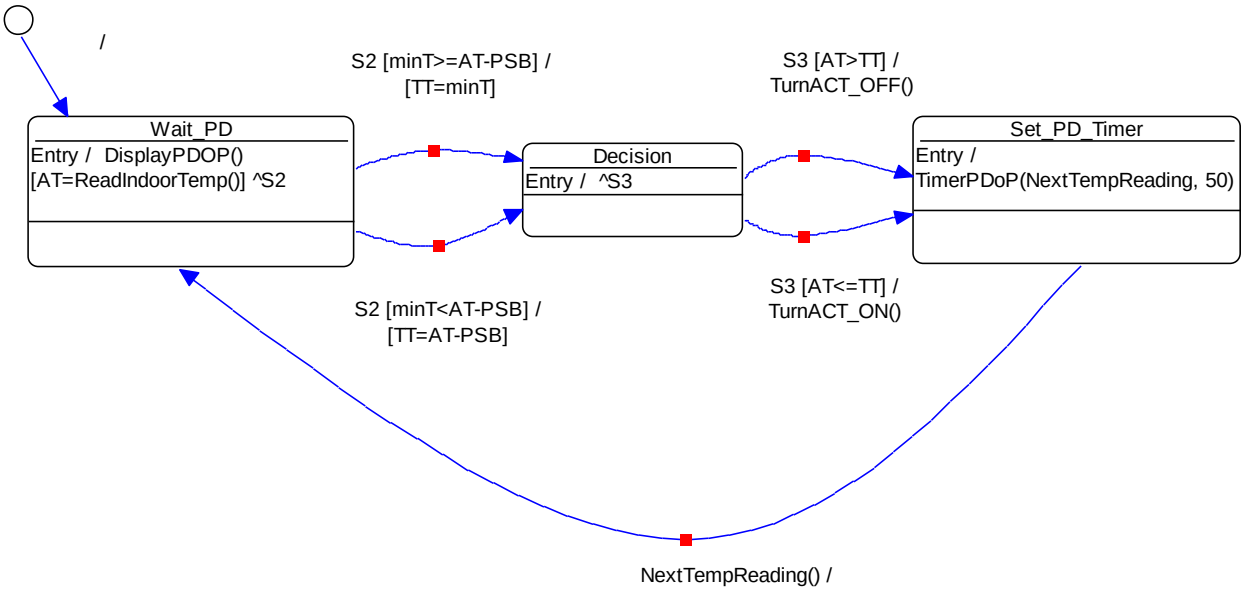

Figure 5: PDemandOP state diagram showing its two sub states.

The peak demand conditions are set by an external entity (e.g. a utility company). In the WSN implementation, the PDA variable represents peak demand conditions and is set by the Joystick of the SmartRF04 evaluation board. PDemandOP state consists of three sub states; 1. Wait_PD, 2. Decision, and 3. Set_PD_Timer:

- ***Wait_PD:***

Wait_PD is the default state of the PDemandOP state. In this state, the environment's temperature is measured using the CC2430 temperature sensor. The result is assigned to the variable AT and displayed for the user on the SmartRF04's LCD. The FSM creates an internal signal, S2, for the purposes in helping the FSM to make a logical decision.

The WSN transitions from the Wait_PD state to the Decision state in one of the following mutually exclusive conditions (i.e. Wait_PD always transitions to Decision):

1. minT ≥ AT-PSB: i.e. the minimum (safe) environment's temperature (minT) is greater or equal to the difference between the between the actual temperature and the predefined setback point (AT-PSB). In this condition, the FSM sets the target temperature (TT) to minT.
2. minT < AT-PSB: i.e. the minimum (safe) environment's temperature (minT) is smaller than to the difference between the between the actual temperature and the predefined setback point (AT-PSB). In this condition, the FSM sets

TT = AT-PSB to ensure the environment's temperature is always kept above the minimum safe temperature.

- ***Decision:***

This is a logical decision state. In visualSTATE, it is NOT possible to make more than 1 logical decision (e.g. a comparison between two variables) per state. However, the FSM needs to make two logical decisions while in the PDemandOP state. Therefore, the first logical decision is made on the transitions from the Wait_PD to the Decision state. Then, the second logical comparison is made on the transitions from the Decision state to the Set_PD_Timer state.

The WSN transitions from the Decision state to the Set_PD_Timer state in one of the following mutually exclusive conditions (i.e. Decision always transitions to Set_PD_Timer):

1. AT > TT: i.e. the actual environment's temperature is greater than the target temperature. In this condition, the FSM turns OFF the emulated thermostat.
2. AT ≤ TT: i.e. the actual environment's temperature is smaller or equal to the target temperature. In this condition, the FSM turns ON the emulated thermostat.

- Set_PD_Timer:

In this state a timer is set and once it expires, the WSN returns back to the Wait_PD state and process continues until the Peak Demand Alarm is cleared (i.e. PDA = 0) at which point, the WSN transitions to the NormalOP state. The timer value is set to 50 milliseconds for illustration purposes. This concludes the discussion of the WSN and its implementation.

2.4.6 WSN: Typical Results

In this section, some typical results from the WSN prototype are showcased. All possible states of the WSN are demonstrated by setting the appropriate variables and observe the WSN's responses on the SmartRF04's LCD (which serves as the WSN-End user interface). Such responses prove the successful demonstration of the WSN prototype. For convenience purposes, the state diagram for each of the WSN states is shown.

2.4.6.1 Startup State Results

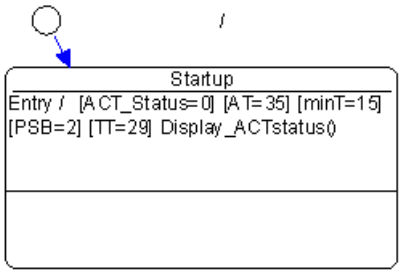

Figure 6: WSN Startup State Diagram (single state).

In the startup state, the FSM is initialized and the emulated thermostat (ACT variable) is set to OFF. This is displayed to the end user. Figure 7 confirms the correct operation of the startup state.

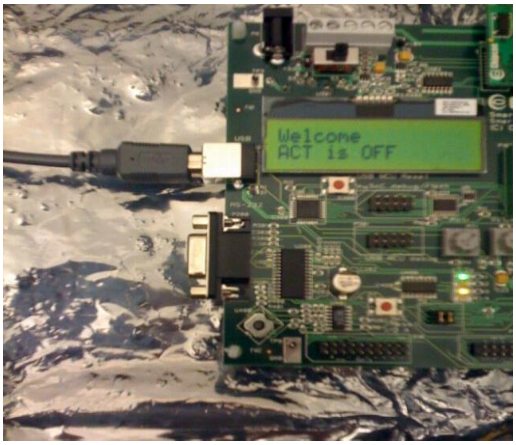

Figure 7: WSN Startup State Diagram (single state).

2.4.6.2 NormalOP State Results

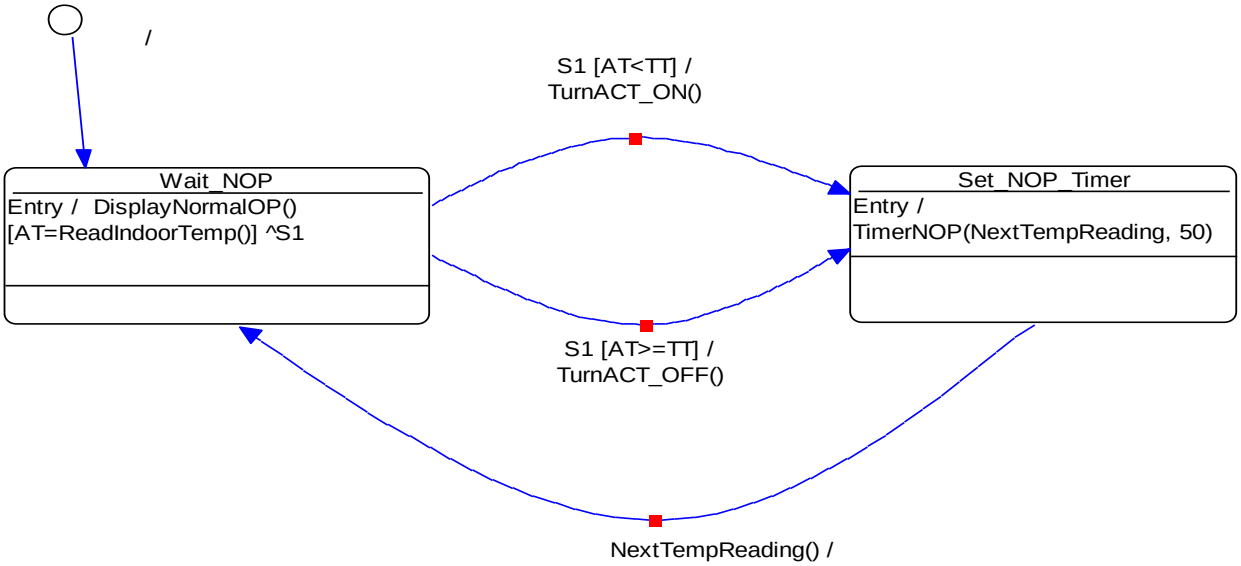

Figure 8: WSN NormalOP state diagram.

There are two sub states in the NormalOP state. Correct WSN operation is demonstrated by setting the appropriate variables.

2.4.6.2.1 Case 1: AT<TT.

Settings: To achieve this case, the following variables are: 1. minT = 15 °C, 2. PSB = 2 °C, and 3. TT = 30 (°C).

Expected result: The WSN turns ON the emulated thermostat. I.e. ACT ON is displayed on the LCD.

Measurement: The CC2430 temperature sensor reading is 29 °C (i.e. AT = 29 °C).

Figure 9: Environment's temperature measured by CC2430. WSN is in NormalOP.

WSN prototype result: Correct operation demonstrated.

Figure 10: WSN's correct response to Case 1 in NormalOP.

2.4.6.2.2 Case 2: AT ≥ TT.

Settings: To achieve this case, the following variables are set: 1. minT = 15 °C, 2. PSB = 2 °C, and 3. TT = 25 (°C).

Expected result: The WSN turns OFF the emulated thermostat. I.e. ACT OFF is displayed on the LCD.

Measurement: The CC2430 temperature sensor reading is 29 °C (i.e. AT = 29 °C).

Figure 11: Environment's temperature measured by CC2430. WSN is in NormalOP.

WSN prototype result: Correct operation demonstrated.

Figure 12: WSN's correct response to Case 2 in NormalOP.

2.4.6.3 PDemandOP State Results

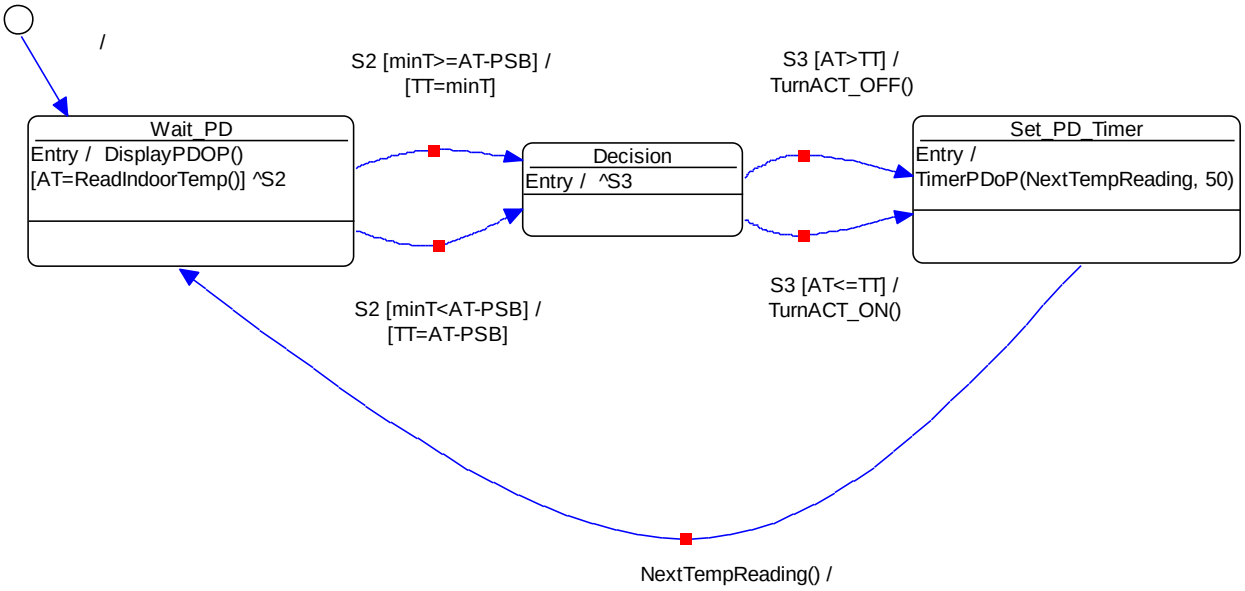

Figure 13: WSN Startup State Diagram (single state).

There are three sub states in the PDemandOP state. Correct WSN is demonstrated by setting the appropriate variables. Note that the Decision state does not have any

associated action that is shown to the end user on the LCD screen. Nonetheless, its correct operation is verified by the correct operation of the other two sub states: Wait_PD, and Set_PD_Timer.

2.4.6.3.1 Case 1: minT ≥ AT-PSB and AT>TT

Settings: To achieve this case, the following variables are set: 1. minT = 25 °C, 2. PSB = 5 °C, and 3. TT = 25 (°C).

Expected result: The WSN turns OFF the emulated thermostat. I.e. ACT OFF is displayed on the LCD.

Measurement: The CC2430 temperature sensor reading is 29 °C (i.e. AT = 29 °C).

WSN prototype result: Correct operation demonstrated.

Figure 14: WSN's correct response to Case 1 in PDemandOP.

2.4.6.3.2 Case 2: minT ≥ AT-PSB and AT ≤ TT

Settings: To achieve this case, the following variables are set: 1. minT = 30 °C, 2. PSB = 5 °C, and 3. TT = 30 (°C).

Expected result: The WSN turns ON the emulated thermostat. I.e. ACT ON is displayed on the LCD.

Measurement: The CC2430 temperature sensor reading is 29 °C (i.e. AT = 29 °C).

WSN prototype result: Correct operation demonstrated.

Figure 15: WSN's correct response to Case 2 in PDemandOP.

2.4.6.3.3 Case 3: minT<AT-PSB and AT>TT

Settings: To achieve this case, the following variables are set: 1. minT = 15 °C, 2. PSB = 2 °C, and 3. TT = 27 (°C).

Expected result: The WSN turns OFF the emulated thermostat. I.e. ACT OFF is displayed on the LCD.

Measurement: The CC2430 temperature sensor reading is 29 °C (i.e. AT = 29 °C).

WSN prototype result: Correct operation demonstrated.

Figure 16: WSN's correct response to Case 3 in PDemandOP.

2.4.6.3.4 Case 3: minT<AT-PSB and AT≤TT

Settings: To achieve this case, the following variables are set: 1. minT = 15 °C, 2. PSB = 0 °C, and 3. TT = 29 (°C).

Expected result: The WSN turns ON the emulated thermostat. I.e. ACT ON is displayed on the LCD.

Measurement: The CC2430 temperature sensor reading is 29 °C (i.e. AT = 29 °C).

WSN prototype result: Correct operation demonstrated.

Figure 17: WSN's correct response to Case 4 in PDemandOP.

2.5 Conclusion

In this chapter, Wireless Sensor Networks (WSN) were introduced and their distinct advantages (compared to traditional, wired solutions) and rapidly growing role in a wide variety of applications including environmental monitoring and control of large scale/area environments were highlighted. The ZigBee standard was introduced as one of the most promising communication standards for WSNs and its key features and advantages were briefly discussed. A basic WSN prototype was introduced and experimentally demonstrated. It monitors and controls the temperature of an environment. This prototype was built using commercial low power, low cost, and small size sensor nodes. The WSN prototype serves as a practical demonstration of the communication side of the proposed optical sensor mote which is envisioned to be built as a low power, low cost, and small size sensor node.

Chapter 3 Optical Sensor Mote: Photonic Crystal structures for Multi-Gas sensing

3.1 Background

In the Chapter, the theoretical, numerical, and experimental investigation of Photonic Crystal structures for applications as multi-gas sensors is presented. A brief introduction to photonic crystal theory is given following established approaches reported in the literature [Joannopoulos et al. 2008; NAir and Vijaya 2010] together with the state-of –the-art in the field of photonic crystal sensors. The material considerations that led to the selection of the silicon-on-insulator (SOI) platform **[**Shinya, et al. 2002] for the first photonic crystal gas sensor prototype are discussed, as well as the initial design and numerical simulation of its waveguiding performance. Then the fabrication detail and experimental characterisation results of the SOI gas sensor are presented.. The numerical simulation of the performance of a second gas sensor prototype based on InP is detailed. Finally, the Chapter closes with an introduction to a Slow Light Photonic Crystal Multi-Gas Sensor, providing an experimental investigation of its performance and drawing conclusions on its applicability.

3.2 Introduction to Photonic Crystal Theory

Photonic crystals have grown in research popularity ever since they were first proposed and demonstrated in 1987 [Joannopoulos et al. 2008]. They represent a new class of optical materials with their ability to control a photon's properties in a

manner analogous to the way semiconductor materials control electron properties. Indeed, photonic crystals are to optics, what semiconductor materials are to electronics.

Photonic crystals consist of a periodic arrangement of high and low dielectric (could also be metallic) regions. Such an arrangement creates a situation where photons of a certain wavelength are allowed to propagate in the photonic crystals, while other photons are prohibited from propagating. This occurs because photons behave as waves and only certain wavelengths (that meet certain criteria) are allowed to travel through the periodic structure of the photonic crystal without being scattered. This situation gives rise to the concept of the **Photonic Band-Gap**, a region where bands of wavelengths are forbidden from propagating in the crystal structure [Joannopoulos et al. 2008]. The periodicity can take place in one, two, or in all three physical dimensions, giving rise to the 1-D, 2-D, and 3-D photonic crystals classification.

Photonic crystals represent a revolution in the field of (integrated) optics and photonics. Their novel properties, including their ability to strongly confine and localize light, very small "foot print" (orders of magnitude less than ordinary optical devices), and the very presence of a photonic band-gap, all lead up to the creation of a versatile class of devices that find a wide array applications, both conventional and novel. Some of these applications include optical waveguides, optical sensors, (add/drop) filters, slow and superluminal propagation, super-prism and super-collimators, high Q resonators, micro-cavities, lasers, and others [Pavesi and Guillo 2006; Giancarlo et al. 2009].

Additionally, Photonic Crystals allow the study and to better understand light-matter interactions with novel phenomena such as slow and superluminal light waves [Galisteo-López et al. 2007]. The novel properties of photonic crystals and their integrated nature make them ideal candidates for the optical sensing component of the proposed ***optical sensor mote***. Most importantly, photonic crystals offer a versatile and compact sensing platform to build miniaturized and high performance sensors that are currently not possible in other technologies or by other approaches [Passaro 2013].

The propagation of light through a periodic dielectric structure may be analyzed in a manner similar to the propagation of electrons through a periodic arrangement of atoms. Therefore concepts like the Bloch theorem, energy bands, and Brillouin zones are applicable to the case of photonic crystals [Joannopoulos et al. 2008; NAir and Vijaya 2010]. The relation between the wavevector **k** and the frequency ω results in the dispersion relation for light propagating in free space given by:

$$\omega = ck \qquad (1)$$

where:

- *k*: the magnitude of wavevector, also referred to as wavenumber and equal to $\frac{2\pi}{\lambda}$,
- *c*: speed of light in vacuum.

When light is incident on a periodic structure, it gets reflected from each interface. These reflected waves, under suitable conditions, interfere constructively according to the well-known Bragg condition. This is given by (modified for the photonic crystals) [NAir and Vijaya 2010]:

$$m\lambda = 2n_{eff}d \qquad (2)$$

where:

- m: the diffraction order,
- λ: wavelength of reflected light,
- n_{eff}: the effective refractive index of the periodic structure i.e. the photonic crystal,
- d: the lattice period of the crystal in the direction of propagation of light.

Thus light incident on a photonic crystal, certain wavelengths will get reflected according to Equation (2). The key parameters that determine the value of these wavelengths are the effective index of the photonic crystal and its period. The peak in the reflection will be associated with a trough in the transmission and the wavelengths at which this happens are referred to as the photonic stop band. When this stop band is valid for all directions of propagation and both polarization states of light, then this forbidden band in transmission is referred to as a complete photonic band gap [Joannopoulos et al. 2008; NAir and Vijaya 2010]. It is important to note that the wavelengths which are absent in the transmission are not absorbed by the photonic crystal unlike in semiconductors, where the band gap wavelength or energy

corresponds to the absorption band of light by the material. In a photonic crystal however, the band gap refers to a range of wavelengths which are not allowed to propagate through the structure resulting in high reflection.

Propagation of light in a medium can be explained using the well known Maxwell's equations for electric and magnetic fields given by:

$$\nabla \bullet \boldsymbol{B}(\boldsymbol{r},t) = 0 \qquad (3)$$

$$\nabla \times \boldsymbol{H}(\boldsymbol{r},t) - \frac{\partial \boldsymbol{D}(\boldsymbol{r},t)}{\partial t} = 0 \qquad (4)$$

$$\nabla \bullet \boldsymbol{D}(\boldsymbol{r},t) = 0 \qquad (5)$$

$$\nabla \times \boldsymbol{E}(\boldsymbol{r},t) + \frac{\partial \vec{B}(\boldsymbol{r},t)}{\partial t} = 0 \qquad (6)$$

where:

- $\boldsymbol{E}(\boldsymbol{r},t)$: the electric field,
- $\boldsymbol{H}(\boldsymbol{r},t)$: the magnetic field,
- $\boldsymbol{D}(\boldsymbol{r},t)$: the electric displacement,
- $\boldsymbol{B}(\boldsymbol{r},t)$: the magnetic induction field.

Assuming that the material of interest (i.e. photonic crystals) is non-magnetic (with a magnetic permeability of $\mu = \mu_{\circ}$) linear, isotropic, real, and lossless and that the dielectric constant is frequency independent, then;

$$\boldsymbol{B}(\boldsymbol{r},t) = \mu_{\circ}\, \boldsymbol{H}(\boldsymbol{r},t) \quad (7)$$

$$\boldsymbol{D}(\boldsymbol{r},t) = \varepsilon_{\circ}\varepsilon(\boldsymbol{r})\, \boldsymbol{E}(\boldsymbol{r},t) \quad (8)$$

$$n = \sqrt{\varepsilon(\boldsymbol{r})} \quad (9)$$

where:

- $\varepsilon(\boldsymbol{r})$: the dielectric constant,
- $\varepsilon_{\circ}$: vacuum's permittivity,
- $\mu_{\circ}$: vacuum's permeability,
- n : the refractive index.

Combining Equations (3) to (9) gives the wave equation for the magnetic field [Joannopoulos et al. 2008; NAir and Vijaya 2010] as:

$$\nabla \times \left[\frac{1}{\varepsilon(\boldsymbol{r})} \nabla x \boldsymbol{H}(\boldsymbol{r},t) \right] = \frac{-1}{c^2} \frac{\partial^2 \boldsymbol{H}(\boldsymbol{r},t)}{\partial t^2} \quad (10)$$

Assuming harmonic time dependence for the fields at a frequency of ω, $\boldsymbol{E}(\boldsymbol{r},t)$ and $\boldsymbol{H}(\boldsymbol{r},t)$ can be written as:

$$\boldsymbol{E}(\boldsymbol{r},t) = \boldsymbol{E}(\boldsymbol{r}) e^{-i\omega t} \quad (11)$$

$$\boldsymbol{H}(\boldsymbol{r},t) = \boldsymbol{H}(\boldsymbol{r}) e^{-i\omega t} \quad (12)$$

Thus, Equation (10) can be expressed in a simplified form known as the wave equation for a photonic crystal or the master equation for a photonic crystal:

$$\nabla \times \left[\frac{1}{\varepsilon(\boldsymbol{r})} \nabla x \boldsymbol{H}(\boldsymbol{r}) \right] = \frac{\omega^2}{c^2} \boldsymbol{H}(\boldsymbol{r}) \qquad (13)$$

Equation (13) is an eigenvalue equation with eigenfunction $\boldsymbol{H}(\boldsymbol{r})$ and eigenvalue $\frac{\omega^2}{c^2}$. The master equation is set in terms of $\boldsymbol{H}(\boldsymbol{r})$ instead of $\boldsymbol{E}(\boldsymbol{r})$ because the operator acting on $\boldsymbol{H}(\boldsymbol{r})$ is Hermitian [Joannopoulos et al. 2008] which simplifies the problem significantly. Some common ways of solving Equation (13) include: the plane wave expansion method [Shi et al. 2004], Finite Difference Time Domain (FDTD) [Sullivan 2000; Qiu 2001] method and others exist [Joannopoulos et al. 2008; NAir and Vijaya 2010] .

In a photonic crystal, discrete translational symmetry can exist in up to 3 directions, i.e. for a 3D photonic crystal. The basic step length is the lattice constant "a", and the basic step vector is referred to as the primitive lattice vector. In Equation (8), owing to this discrete symmetry, $\varepsilon(\boldsymbol{r}) = \varepsilon(\boldsymbol{r} + \boldsymbol{a})$ and if this translation is repeated, $\varepsilon(\boldsymbol{r}) = \varepsilon(\boldsymbol{r} + \boldsymbol{R})$ for any **R** that is an integral multiple of a.

In such a situation, the Bloch-Floquet theorem for periodic eigen-problems [Ashcroft and Mermin 1976; Joannopoulos et al. 2008] states that the solutions to Equation (13) can be written in the form:

$$\boldsymbol{H}(\boldsymbol{r}) = \boldsymbol{U}_{\boldsymbol{k},n}(\boldsymbol{r})e^{i\,\boldsymbol{k}\,\boldsymbol{r}} \qquad (14)$$

where:

- $\boldsymbol{U}_{\boldsymbol{k},n}(\boldsymbol{r})$: a periodic envelope function at the same periodicity as that of the lattice, $\boldsymbol{U}_{\boldsymbol{k},n}(\boldsymbol{r}) = \boldsymbol{U}_{\boldsymbol{k},n}(\boldsymbol{r}+\boldsymbol{a})$,
- $\boldsymbol{k}$*:* the wavevector in the first Brillouin zone.

Furthermore, due to the translational periodicity of the photonic crystal lattice, the solutions of Equation (14) can be constrained to the first Brillouin zone and each band can be labelled with an integer, "n".

It is important to note that the dispersion relation for a periodic structure like a photonic crystal is different from that for a homogenous medium. In a homogenous medium, the dispersion has a linear relationship between the frequency and the wavevector for all values of the frequency. In a periodic structure however, the dispersion relation shows forbidden frequencies at **k** values of $k = \frac{\pi}{a}, \frac{2\pi}{a}, ..., \frac{n\pi}{a}$ with "n" being an integer. When the wavevector reaches values which are integral

multiples of $\frac{\pi}{a}$, light is reflected according to the Bragg condition of Equation (2) and this results in a high reflection band for those frequencies, occurring whenever the wavevector reaches the Brillouin zone boundary of the photonic crystal [Joannopoulos et al. 2008; NAir and Vijaya 2010].

Waves in a photonic crystal may be referred to as Bloch waves as described in Equation (14). Such waves are naturally propagating away from the forbidden zone but near the zone boundaries they become standing waves. Bloch wave vectors are imaginary in the forbidden zone and have real values away from the zone boundaries. Numerical field calculations show that waves at the low frequency band edge concentrate their energy in low index regions of the photonic crystal [Joannopoulos et al. 2008]. On the other hand, Bloch waves at frequencies in the forbidden zone i.e. inside the band gap exhibit a decaying behaviour in the photonic crystal structure.

3.2.1 Photonic Crystal Slabs

In this research work the attention is focused on photonic crystal slab structures, also known as planar photonic crystals and sometimes referred to more specifically as 2D photonic crystal slabs [Joannopoulos et al. 2008]. These structures are selected over, e.g. a 3D photonic crystal or a quasi photonic crystal because they are currently among the most practical photonic crystal structures to fabricate and serve the purpose of demonstrating a realization of the optical sensor element of the optical sensor mote.

Photonic crystal slabs can be described as photonic crystals with periodicity in two dimensions (length and width, i.e. the plane), and finite thickness in the third dimension (height, i.e. the vertical direction). They are similar to 2D photonic crystals but the presence of the finite thickness in the vertical direction leads to a hybrid structure with interesting and qualitatively different behaviours compared to 2D photonic crystals. In particular, in photonic crystal slabs, two different light guiding mechanisms are used: 1. photonic band gap guiding in the planar direction and, 2. index guiding in the vertical direction (to ensure the light does not radiate out of the plane) [Johnson et al. 1999; Jamois et al. 2002; Joannopoulos et al. 2008]. This way, photonic crystal slabs confine light in all 3 directions (planar and vertical), facilitating the realisation of a practical photonic devices.

This hybrid guiding of photonic crystal slabs ensures that light is confined and guided in photonic crystal structures and devices without the need of a full, i.e. 3D photonic bandgap which increases complexity of manufacture [Joannopoulos et al. 2008]. Such 3D photonic crystals are quite expensive and the fabrication yields are not yet sufficient for mass production. On the other hand, photonic crystal slabs are relatively easy to fabricate (since they are just planar photonic circuits), a major advantage currently making photonic crystal slabs ideal for the majority of applications requiring a photonic crystal approach. In essence, 2D photonic crystal slabs serve as a practical alternative to the full 3D light confinement offered by 3D photonic crystals. The main draw back to photonic crystal slabs is that extra care needs to be taken in their design to ensure proper operation and to minimize losses

that arise due to, among other things, the break in periodicity in the vertical direction [Jamois et al. 2002**;** Joannopoulos et al. 2008].

From the above discussion it is concluded that photonic crystal slabs are ideal candidates for the realization of the optical sensing element in the proposed optical sensor mote, combining photonic bandgap guiding with the ease of fabrication of planar photonic devices. Furthermore, discussed in more detail in subsequent sections, photonic crystals potentially make excellent candidates for multi gas sensors, the application chosen to experimentally demonstrate the sensing functionality of the proposed optical sensor mote. The approach of using the slow light mode in photonic crystals to sense gases in presented in Section 3.6

3.3 Photonic Crystals and Gas Sensing

3.3.1 Photonic crystals as a versatile sensing platform

Photonic crystals form a truly versatile sensing platform and find wide ranging applications in many different sensing disciplines [NAir and Vijaya 2010]. To date, photonic crystals have been successfully demonstrated as chemical, surface wave, biological (including virus detection), humidity , pressure, image, vapour, ionic, gas, refractive index, oil, and temperature sensors with new demonstrations continuing to appear in literature [Lee and Fauchet 2007; Buswell et al. 2008; Dorfner et al. 2008; Falco et al. 2008; Jensen et al. 2008; Sünner, et al. 2008; Dorfnera et al. 2009; Falco et al. 2009; Dahdah 2010; Jágerská et al. 2010; Jágerská et al. 2010b; Kang et al. 2010; NAir and Vijaya 2010; Wang et al. 2010; Fan and White 2011; Lai et al. 2011;

Li Junhua et al. 2011; M.G. Scullion et al. 2011; Pergande et al. 2011; Zaho et al. 2011; Chakravarty et al. 2012; Hosseinibalam et al. 2012; Liu and Salemink 2012; Ralf Luckluma et al 2012; Zaho et al. 2012; Zhang et al. 2012; Passaro et al. 2012a; Passaro et al. 2012b; Passaro et al. 2012c; Passaro 2013; Passaro et al. 2013]. Very recently, photonic crystal sensors are being offered as commercial products [PRN 2013a; PRN 2013b].

To date, photonic crystals have been successfully demonstrated experimentally as gas sensors [Dorfner et al. 2008; Falco et al. 2008; Jensen et al. 2008; Sünner, et al. 2008; Falco et al. 2009; Dahdah 2010; Jágerská et al. 2010b; Kang et al. 2010; Lai et al. 2011; NAir and Vijaya 2010; Wang et al. 2010 ; Pergande et al. 2011; Zaho et al. 2011; Zaho et al. 2012; Zhang et al. 2012; Passaro et al. 2012a; Passaro et al. 2012b; Passaro et al. 2012c; Passaro 2013; Passaro et al. 2013]. [NAir and Vijaya 2010; Zaho et al. 2011; Passaro et al. 2012a; Passaro et al. 2013] provide an excellent summary of the state of the art of photonic crystal gas sensors.

Photonic crystals were also successfully demonstrated as liquid and biosensors [Buswell et al. 2008; Dorfnera et al. 2009; Li Junhua et al. 2011; M.G. Scullion et al. 2011; Chakravarty et al. 2012; Hosseinibalam et al. 2012; Liu and Salemink 2012 ;Ralf Luckluma et al 2012] as well as for single particle detection [Lee and Fauchet 2007; Fan and White 2011]. In a key paper, [Lee and Fauchet 2007] experimentally demonstrated a photonic crystal sensor with an active sensing volume of $\sim 0.15 \mu m^3$ that was capable of detecting ~1 fg (femto-gram) of matter. Its performance was tested with latex spheres with sizes that fall in the size range of a variety of viruses

including the Hepatitis virus (50 nm in diameter), Influenza A (100 nm in diameter), and Vaccinia virus (300–450 nm by 170–260 nm and brick shaped) [Lee and Fauchet 2007]. [Fan and White 2011] provides an excellent summary of the state of the art of photonic crystal liquid and biosensors.

3.3.1.1 Photonic crystals as gas sensors

As previously discussed in Chapter 1 and Chapter 2, environmental gas sensing using distributed techniques is an emerging and exciting field in the engineering discipline and represents an ideal reference to demonstrate the ***optical sensor mote*** concept, which has the potential to complement traditional gas sensors currently fielded in large scale environments such as farms and mines [Hall 2009a; Hall 2009b].

Gas sensors find a wide range of applications in many fields of science, engineering, health, and the environment as well as commercial applications. Many gas sensing technologies have been developed including semiconductor, solid state and spectroscopy based sensors [Moseley 1997; Yamazoe 2005]. In particular, spectroscopic techniques play a significant role in gas sensing and are capable of very high sensitivities, approaching parts per trillion [Wehrspohn et al. 2005; Pergande et al. 2011]. Currently, spectroscopic techniques offer the highest sensitivity and most accurate gas sensing technologies (detecting a gas based on its unique optical absorption spectrum) and are expected to continue to do so in the future.

The main drawbacks of spectroscopic techniques include the need for long interaction lengths ranging from meters to kilometres and severe demands on the optical components of the spectroscopic system. The interaction of light with gases is weak in nature compared to its interactions with liquids or solids. Therefore, long interaction lengths and large interaction volumes are required to achieve sufficient interaction strengths for meaningful and practical sensing [Robinson et al. 2008]. As a consequence, spectroscopic systems are often bulky and very expensive [Pergande et al. 2011]. This makes the typical spectroscopic gas sensors impractical for distributed gas sensing of large scale areas and the development of alternatives to realize distributed gas sensing. is a worthwhile area of research.

Commercial products based on spectroscopic gas sensing technologies that have been successfully applied to distributed sensing are currently being offered [OptoSniff]. These approaches utilize fibre cables to transmit data from a large number of sensing points and provide real time, highly accurate sensing of hazardous gases (methane and natural gas). The proposed optical sensor mote, based on photonic crystals (utilizing refractive index sensing to detect different gases) potentially offers a more compact (integrated) form utilizing RF signals to transmit the data between the sensing nodes/points. The advantages of the concept are far lower cost potential owing to the fact that it is amenable to mass production, label free (multi gas sensing capabilities) and more applicable to wider environments where the use of fibre cables can become difficult or impossible to deploy. However, there are several existing drawbacks which will be discussed later, but among the most significant, is the inherent lower accuracy of the approach compared to

spectroscopic approaches especially for gas sensing; purely spectroscopic gas sensing techniques will continue to be the most accurate technologies for the future.

Photonic crystals have emerged as potential candidates for the realization of very compact, robust, and very low cost gas sensors [Wehrspohn et al. 2005]. By using photonic crystals three main challenges with spectroscopic gas sensors can be overcome: 1. the weakness of light-gases interactions (which necessitates the need for long interaction length), and 2. bulkiness/large form factor, and 3. cost, which can be significant for spectroscopic gas sensors Thus, photonic crystals have the pathway to create low cost, small form factors gas sensors that can be used as distributed gas sensors.

3.3.1.2 State of the art for photonic crystals gas sensors

To date, many different types of photonic crystal sensors have been reported in literature. A useful way to categorize these sensors is to examine the sensing principle employed [Zaho et al. 2011; Passaro 2013]. The most common types of photonic crystal sensors demonstrated include: refractive index (RI) sensors, optical absorption sensors, opto-mechanical sensors, nonlinear effects sensors, and photonic crystal fibre sensor. In the following discussion, various types of photonic crystal sensors are briefly discussed and a new class of sensor based on slow light refractive index changes is proposed.

3.3.1.2.1 Refractive Index based sensors

RI based sensors are the most common type of photonic crystal sensors currently studied, realised in a variety of different configurations such as (straight) waveguides, interferometric, and microcavities (L3, L5, H5...etc) [Chalcraft et al. 2007; Kicken et al. 2008]

A range of advantages are cited driving their development such as being label free (i.e. no need to coat the sample with any florescent agent), offering high sensitivity and selectivity, and real time capabilities [Passaro 2013]. Their sensing principle is based on measuring RI changes of a bulk reference solution (e.g. Air or water) due to the presence of a chemical (or biological) analyte (e.g. a gas) of different refractive index. RI sensors have been studied extensively and are capable of detecting very minute concentrations of chemical and biological species [Dorfner et al. 2008; Falco et al. 2008; Jensen et al. 2008; Sünner, et al. 2008; Wehrspohn 2005; Wang et al. 2008; Robinson et al. 2008; Sünner, et al. 2008; Falco et al. 2009; Awad et al. 2010; Dahdah 2010; Jágerská et al. 2010b; Kang et al. 2010; Lai et al. 2011; NAir and Vijaya 2010; Wang et al. 2010 ; Pergande et al. 2011; Zaho et al. 2011; Zaho et al. 2012; Zhang et al. 2012; Passaro et al. 2012a; Passaro et al. 2012b; Passaro 2013; Passaro et al. 2013]

[Lee and Fauchet 2007] experimentally demonstrated a photonic crystal sensor capable of single particle detection. For an active sensing volume of ~0.15μm^3, the device was capable of detecting ~1 fg of matter; its performance was tested for the detection of viruses (e.g. Influenza). More recently, [Lin et al. 2012] successfully

demonstrated an RI based photonic crystal sensor capable of detecting single molecules and proteins (e.g., streptavidin, DNA, mRNA), surface or volumetric density.

Photonic crystal RI sensors harness two fundamental sensing principles: 1. Surface sensing, and 2. Homogeneous sensing [Passaro 2013]. In surface sensing, the photonic crystal holes are initially coated by receptor molecules properly chosen in order to selectively adsorb the target analytes in a complex solution. When the sensor is exposed to a chemical/biological sample, the target molecules are immobilized by the receptor molecules on the sensor hole inner surfaces. The adsorbed layer induces a localized refractive index change around the hole region and measuring that RI change allows the detection of the target molecules and their concentration.. In homogenous sensing, the effective index of the propagating optical mode changes because of changes in the cover RI induced by chemical or biological samples properly concentrated in the cover (cladding) medium, where the photonic sensor is exposed. Thus, a homogenous sensitivity, S_h, may be defined as [Passaro 2013]:

$$S_h = \frac{\partial n_{eff}}{\partial n_c} \qquad (15)$$

where:

- n_{eff}: the effective refractive index of the propagating optical mode;
- n_c: the cover refractive index.

There exists two main interrogation approaches for extracting the sensing data from photonic crystal RI based sensors (micro-resonators, cavity, or waveguide based): 1. Wavelength interrogation, and 2. Intensity interrogation. In wavelength interrogation, the sensing data is obtained by monitoring the sensor output via an optical spectrum analyzer (OSA). In intensity interrogation, the intensity changes of the output signal of the sensor by using a photo detector (PD) are monitored.

A fundamental parameter for quantifying the sensor performance in the case of the wavelength interrogation approach is the wavelength sensitivity, S_λ, and has units of nm/RIU (refractive index unit) and is defined as [Passaro 2013]:

$$S_\lambda = \frac{\Delta\lambda}{\Delta n} \qquad (16)$$

where:

- $\Delta\lambda$: the shift of the resonant wavelength;
- Δn: the change in the reference/background refractive index.

A second fundamental parameter that drives the design of a photonic crystal cavity RI sensor is the Quality factor (of the cavity), Q, defined as (applicable to high Q values) [Passaro 2013]:

$$Q = \frac{f_o}{\Delta f} \qquad (17)$$

where:

- f_o : the resonant frequency;
- Δf: the peak bandwidth.

Photonic crystal cavities are capable of very high Q values, with reported experimental values from 2000 to 7.5 x 10^5 [Akahane et al. 2003; Vahala 2003; Benson 2006; Robinson et al. 2008; Deotare et al. 2009; Passaro 2013]. This presents a great advantage enhancing the inherent weakness of light and gas interactions without the need for long interaction lengths (e.g. several meters in typical spectroscopic sensors compared to a few μm or less in a photonic crystal cavity).

[Wang et al. 2008] theoretically demonstrated an ultra-compact gas sensor based on a two dimensional point-defect photonic crystal resonance micro-cavity. The sensor had a small sensing area of ~10 μm^2 and requires only ~ 1fL of sample analyte to operate. The sensor had a calculated sensitivity of 330 nm/RIU. [Sünner, et al. 2008] experimentally demonstrated a photonic crystal cavity gas sensor where a change of the refractive index by 10^{-4} led to a shift of the resonance of the cavity by 8 pm, easily detectable due to the high quality factor of the cavity. Based on this foundation research, a multi gas sensor system (Section 3.3) formed by a L3 resonant cavity sandwiched between two W1.06 waveguides in a 2D photonic crystal slab was introduced and theoretically demonstrated [Awad et al. 2010; Zaho et al. 2011]. FDTD simulation results show that the wavelength sensitivity of the sensor could reach as much as 3000 nm/RIU (Section 3.3.6).

[Passaro et al. 2012c] demonstrated a generalized approach for the design of photonic crystal RI gas sensors based on multiple ring resonators configurations in the mid-IR wavelength range. These sensors had record high sensitivities of the order of 10^5 nm/RIU. A theoretical approach based on a linear interpolation of the refractive indices of the target gases indicated that these sensors are able to detect mixtures of methane and ethane gases in Air as shown:

$$n_{mix} = n_{gas} \bullet C_{gas} + n_{air} \bullet C_{air} \quad (18)$$

$$C_{air} = 1 - C_{gas} \quad (19)$$

where:

- n_{gas}, n_{Air}, n_{mix}: the refractive indices of the target gas to be detected, Air, and the mixture (of Air and gas) respectively,
- C_{gas}, C_{Air}: concentration of target gas (to be detected) and Air respectively in the mixture (of Air and gas).

For example, utilizing a RI sensor to detect methane (CH_4) in Air in order to provide low level and high level alerts (similar to the principle demonstrated in Chapter 2) of methane concentrations between the explosion limits i.e. lower explosion limit (LEL) of 5% and upper explosion limit (UEL) of 15%), and assuming n_{CH4} = 1.000444 and n_{Air} = 1, using equation (18) and (19), the refractive index for the two explosion limits, $n_{LEL\ mix}$ and $n_{UEL\ mix}$ can be calculated as shown in Equation (20) and Equation (21). The analysis indicates that a RI based sensors are able to distinguish between the two limits [Passaro et al. 2012c]:

$$n_{LEL\ mix}(5\%\ CH_4, \text{Air}\ 95\%) = 1.0000222 \quad (20)$$

$$n_{UEL\ mix}(15\%\ CH_4, \text{Air}\ 85\%) = 1.0000666 \quad (21)$$

Photonic crystal RI based sensors with various advanced configurations (e.g. cascaded micro-resonators, slot cavity photonic crystals) and in different materials (e.g. SOI, and InP) have been reported in literature with wavelength sensitivities ranging from 26 nm/RIU to 610 nm/RIU [NAir and Vijaya 2010; Zaho et al. 2011; Passaro et al. 2012a; Passaro et al. 2012b; Passaro 2013; Passaro et al. 2013].

It is important to note that the refractive index in a photonic crystal is dependant on several parameters including: semiconductor material, pressure, temperature, and the material that surrounds and fills the photonic crystal and its holes [Wehrspohn 2005]. This dependence of the RI on several parameters presents both an advantage and a disadvantage: it makes photonic crystal RI sensors truly versatile sensing platforms that can be adapted to sense many parameters of interest but only if care is taken to ensure that only the parameter of interest is actually sensed. Thus, to sense gases, the sensor temperature, pressure and other parameters must be maintained at a reference level so the only change in RI is due to the change in the gas.

3.3.1.2.2 Optical absorption based sensors based on slow light

Many gas and liquid molecules absorb radiation in the near- and mid-infrared wavelength range, allowing their detection using spectroscopic techniques. When the natural frequencies or resonances of the irradiated molecules is matched by the optical signal (wavelength), the energy states of vibrating atoms change in discrete

steps. These resonance frequencies depend on the number and mass of atoms in molecules as well as the number and strength of chemical bonds [Passaro et al. 2012a]. Infrared (IR) spectroscopy is among the simplest and the most reliable spectroscopic sensing technique. Recently, a number of experimental and theoretical demonstrations of gas sensing in photonic crystal gas cells have emerged. These approaches take advantage of enhanced light-matter interactions due to low group velocities (i.e. slow light) in photonic crystals to effectively increase the interaction length of the gas with light [Jensen et al. 2008; Pergande et al. 2011].

[Lambrecht et al. 2007] designed and experimentally demonstrated an ultra-compact photonic crystal gas sensor based on slow light in 2D silicon photonic crystals. The experimental results with CO_2 showed an enhancement of the absorption by a factor of more than 2 when compared to a traditional (reference) gas cell, the first evidence that enhancement of absorption can be achieved in photonic crystals. Building on this, [Pergande et al. 2011] experimentally demonstrated another ultra-compact photonic crystal gas sensor based on slow light within a straight waveguide but with low reflectivity antireflection layers (to increase the coupling efficiency of the light in and out of the waveguide). Enhancement of CO_2 IR absorption by factors of 2.6-3.5 (compared to an empty reference gas cell) was demonstrated.

[Chakravarty et al. 2011] proposed and experimentally demonstrated an on-chip spectroscopic photonic crystal sensor based on slot waveguides. The experimental response of the sensor followed the linear Beer-Lambert function for low concentrations of methane in nitrogen, with 100 ppm being the lowest detectable

methane concentration. [Lai et al. 2011] also experimentally demonstrated an on-chip spectroscopic sensor. The sensor was a 300 μm long silicon photonic crystal slot waveguide device and utilized infrared absorption spectroscopy for the detection of methane gas. To increase the optical absorption path length, the sensor combined slow light in the photonic crystal waveguide with the high electric field intensity afforded by the slow waveguide. Methane concentrations of 100 ppm in nitrogen were measured.

3.3.1.2.3 Slow light refractive index based sensors

In an effort to overcome the fabrication challenges of the original photonic crystal gas sensor (which was based on the resonant cavity approach), an alternative principle (to spectroscopic absorption) based on using slow light as a sensing mechanism in photonic crystals and applied to gas sensing was proposed, designed and experimentally validated. The approach developed here is different than the existing surveyed work as it does not aim to enhance the optical absorption, but rather, it relies on changes in the refractive index. Thus, the proposed sensor can be classified as a ***slow light refractive index photonic crystal sensor***. The sensor is presented in detail in Section 3.6, the initial findings published in [Awad et al. 2011]; more recent results are provided in Section 3.6 of the Thesis.

3.3.1.2.4 Other approaches: photonic crystal fibres, non RI based photonic crystal sensors

There exist many other mechanisms for gas and liquid sensing using photonic crystals. Some of the most commonly reported include fluorescence, Surface Enhanced Raman Scattering (SERS), Four Wave Mixing (FWM), and Surface Plasmon Resonance (SPR) [Passaro 2013; Zhao et al. 2011]. Additional sensors based on the Self Collimation effect (SC) and Surface Electromagnetic Waves (SEMs) have also been reported [Zhao et al. 2011].

Photonic crystal fibres have a long history of being used as physical, chemical, and biological sensors with great success including the sensing of Methane, Ethane and Acetylene. Photonic crystal fibres sensors can also utilize both linear and nonlinear effects (FWM, SERS, and SPR) for sensing [Passaro 2013]. They have proven to be very efficient sensing solutions for a wide range of practical applications including industrial, medical and environmental applications, often employed for remote and dangerous environments. Their biggest advantage is their fabrication simplicity (thanks to the long history of the fibre industry), high fabrication tolerances and immunity to external perturbations [Passaro 2013; Passaro et al. 2012c]. In essence, photonic crystal fibres borrow all of the best characteristics of standard fibres and add great versatility afforded by the photonic band gap effect. However, their biggest draw back (just like their fibre cousins) is their inability to be integrated with electronics, RF and memory elements to form an optical sensing node/head (Chapter 1).

3.3.1.2.5 Current challenges facing photonic crystal sensors

Photonic crystals are still a relatively new field and, despite intense research efforts world wide, they suffer from several major challenges that limit (but do not preclude) their wide scale adoption and deployment outside research labs in real world applications. Three major challenges currently face photonic crystal devices (sensors and others): 1. Fabrication tolerance 2. Coupling losses and 3. Signal detection [Zhao et al. 2011; Passaro 2013]. In fact, in the experimental phases of this research work, all of these issues represented significant challenges. Photonic crystal fibre sensors do not suffer from these challenges but cannot be integrated with electronics.

A large number of parameters affect photonic crystal device performance including: dielectric constants, materials, lattice and Air hole uniformity [Passaro 2013]. All of these parameters affect the transmission characteristic of photonic crystals and are fabrication dependant and thus, any imperfections will lead to performances that are less than ideal. Although there exist high performance fabrication methods that minimize these imperfections, they are currently very expensive and thus this issue will continue to persist until inexpensive methods are developed [Zhao et al. 2011] or economies of scale bring down the price of such methods.

The transmission of light in a photonic is executed via a Block wave [Joannopoulos et al. 2008], different than the transmission that occurs in standard single mode fibres, which guides the light via total internal reflection. Thus, coupling issues due to mode mismatching arise when coupling light between photonic crystals and

standard fibres. To complicate matters further, typical photonic crystal waveguide widths are on the order of 1 μm where as typical widths of single mode fibres are on the order of 2-9 μm. This creates a serious mode mismatch between the modes in photonic crystal waveguides and single mode fibres and leads to significant coupling losses. Many solutions have been proposed to deal with this issue [Zhao et al. 2011; Passaro 2013]. The most common include interface resonant mode, J-coupler structures, and adiabatic coupling. Adiabatic coupling is among the most promising but requires strict fabrication tolerances. This issue remains a major challenge for photonic crystal research and commercial deployment.

Finally, many problems related to signal detection continue to plague current photonic crystal systems. Typically, photonic crystals are interrogated by either wavelength or intensity interrogation techniques which require high resolution/sensitivity optical spectrometers and detectors and are easily affected by environmental factors (pressure, temperature, moisture levels...etc). This necessitates strict environmental control which can be difficult and expensive. However, due to the great promise and many potentially revolutionary applications of photonic crystals, world wide research effort continue unabated into photonic crystal and their systems.

3.4 SOI Multi-Gas Photonic Crystal Sensor (MG-PhC)

3.4.1 Background

As discussed in chapter 1, one of the primary objectives of this research work is to propose and experimentally demonstrate a novel optical gas sensor (which can be "easily" integrated with RF and electronics). Such an optical sensor is the most integral part of the proposed ***optical sensor mote*** because it is the main differentiating factor from existing sensor motes, which, as was argued in chapter 1, are inadequate for the task of environmental monitoring of large scale areas.

The first attempt at building such an optical gas sensor was to build upon the existing gas sensing approach using localized resonant cavities in photonic crystals [Wehrspohn 2005; Wang et al. 2008; Robinson et al. 2008; Sünner, et al. 2008; Jágerská et al. 2010]. These approaches all focused on sensing a single gas (e.g. Methane or Nitrogen) and only proved the concept without any attempts at optimization. Furthermore, there was no attempt at integrating the sensor with electronics and RF (or even a proposal of such an attempt).

The objective thus became to demonstrate a sensor that can sense multiple gases and be "easily" integrated with electronics so as to form the ***optical sensor mote***.

3.4.2 Material consideration

The proposed multi gas sensor is based on a 2D photonic crystal slab structure. The sensor is able to sense any gases (instead of being specifically tied to one gas) as

long as the refractive index change (from the reference refractive index) induced by the gas falls within the detectable range of the sensor. The sensor's material is silicon (Si) and the fabrication architecture is Silicon on Insulator (SOI) [Chrostowski et al 2010; Jamois et al. 2002; Shinya, et al. 2002]. That is, the photonic crystal itself is fabricated in silicon which sits on top of a silicon oxide (SiO_2, the insulator) layer and the entire structure has a silicon substrate. This fabrication architecture is schematically illustrated in Figure 1.

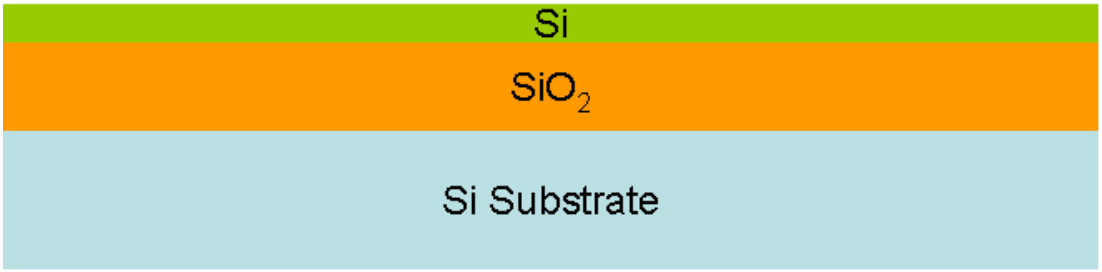

Figure 1: Cross section schematic view of Silicon on Insulator architecture.

There are several important reasons for these material and architectural choices:

1. Silicon is a mature fabrication technology: it is cheap, easy to mass produce with high yields, and almost all electronics are fabricated in silicon. This makes the integration of the photonic crystal gas sensor with other electronic components (e.g. RF, power circuits, and logical gates) easy and cost effective [Pavesi and Guillot 2006; W. Bogaerts et al. 2006]. This further ensures that the feasibility of the full demonstration of the optical sensor mote (which includes photonic sensing and electronics and RF).
2. SOI technology is now mature and preferred for many photonic devices. It provides a strong refractive index contrast to silicon. This greatly helps in

ensuring strong confinement in the vertical direction of the guided light in photonic devices (e.g. waveguides) which are often created in the Si layer [Roelkens et al. 2007; Pavesi and Guillot 2006; W. Bogaerts et al. 2006]. This, "index guiding" mechanism is critical to the correct operation of any 2D photonic crystal slabs. Furthermore, the greater the index contrast, the greater the photonic bandgap will be [Mnaymneh 2003; Joannopoulos et al. 2008]. This gives the sensor a wider range of RI changes to sense which makes it able to distinguish and sense more gases.

The above reasons make SOI technology ideal for the realization of the proposed multi gas photonic crystal sensor (MG-PhC).

3.4.3 Sensor Structure

A top view of the MG-PhC sensor configuration is shown in Figure 2. It consists of: 1) a 2D photonic crystal slab with a triangular lattice structure, 2) two photonic crystal waveguides: a top/input waveguide, and a corresponding bottom/output waveguide, 3) an L3 cavity that couples the light between the input and output waveguides. The separation between the L3 cavity and waveguides is 4 Air hole rows. The sensor configuration is designed to be similar to a telecommunication Add-Drop filter structure. The sensor fabrication architecture is SOI and a side view/cross section is show in Figure 3.

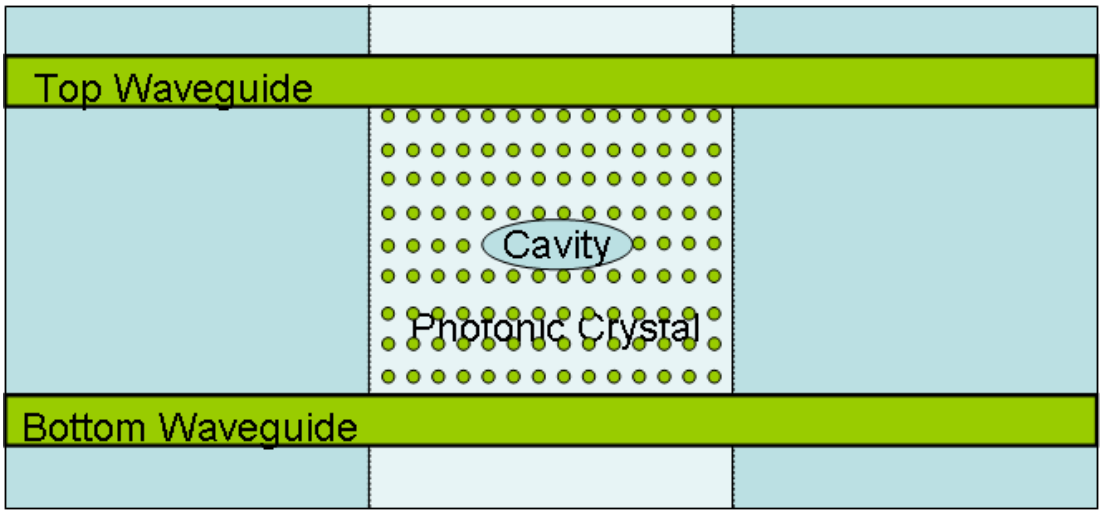

Figure 2: Top view schematic of MG-PhC gas sensor.

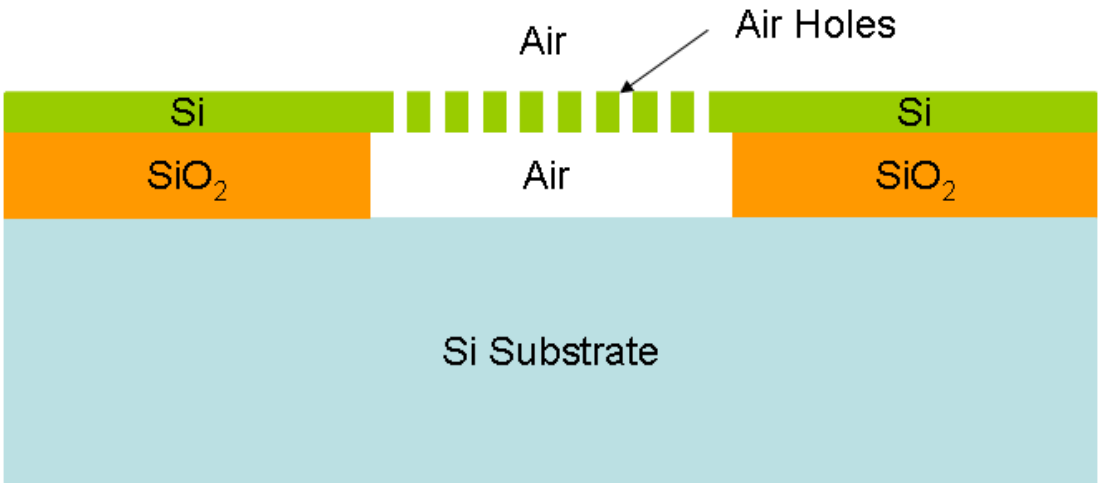

Figure 3: Side view schematic of MG-PhC gas sensor.

3.4.4 Theory of Operation

The sensor functions in a similar fashion to a telecommunication add/drop channel filter. A broadband pulse of light (containing many different wavelengths) propagates through the top waveguide of the sensor (input waveguide); some of the wavelengths excite the cavity resonances which then couple to the bottom waveguide

(output waveguide) and exit the sensor. The cavity resonances are determined by the cavity's physical structure and the refractive index. The refractive index itself is dependant on several factors including: the cavity physical structure (e.g. L3 vs. H1), the photonic crystal material (e.g. Silicon vs. InP), and also on the material that fills the cavity and Air holes (e.g. liquids or gases). If a different kind of gas (other than a reference gas which is typically Air) is present in the photonic crystal's Air holes and cavity, the cavity's refractive index will change which will also cause a change/shift in the cavity's resonances. When this shift happens, the broadband light pulse will excite the new cavity resonances which will in turn couple/decay to the bottom waveguide and exit the sensor. The different gases are identified by observing the output of the sensor. As a result, the sensor is able to sense multiple gases without any change to its configuration which makes it much more versatile compared to other published work [Awad et al. 2011; Zaho et al. 2011].

The critical difference, and key innovation, of this sensor structure compared to the previously published work lies in the presence of the broadband source at the input. The previous sensors relied on a single wavelength laser source (sometimes tunable) that was set or tuned to the cavity's resonance at a certain condition, i.e. the resonance when the target gas is present in the cavity and the whole photonic crystal. The output of the sensor will therefore be "on" (i.e. there is light out of the output waveguide) if the gas to be sensed fills the cavity and "off" in all other conditions. Thus, such sensors are only single gas sensors. By a simple modification of using a broadband light, the sensor becomes a multi-gas sensor.

The sensor can be theoretically analyzed by applying basic micro-resonator theory [Chalcraft et al. 2007; Robinson et al. 2008; Sünner, et al. 2008; Wang et al. 2008; Mnaymneh 2009]. Figure 4 shows a schematic illustration of the sensor to better explain the theory. A broadband pulse consisting of many wavelengths is coupled to the input (top) waveguide of the sensor. If a certain wavelength, say λ_i, satisfies the resonance condition of the micro-resonator, then the coupling of the wave with λ_i will be enhanced while all others will be suppressed. Therefore, λ_i only will couple from the point defect to the bottom output waveguide and exit the sensor. In the presented sensor, the point defect is a L3 photonic crystal cavity [Chalcraft et al. 2007].

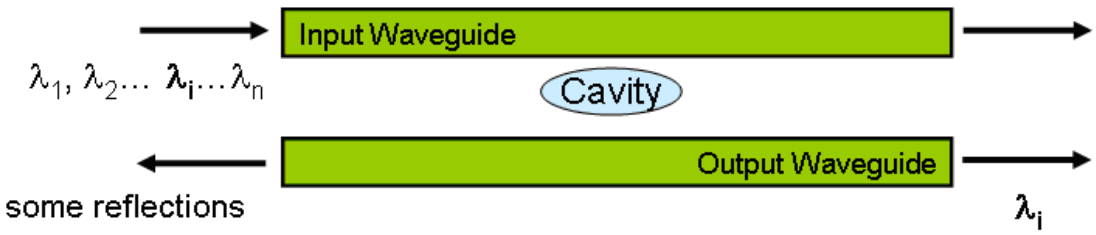

Figure 4: Schematic illustration of the gas sensor as an add/drop filter.

The mth resonance frequency of the L3 cavity can be expressed as [Haus 1985]:

$$f_m = \frac{mc}{2nl} \qquad (22)$$

where:

- f_m: the mth resonance frequency of the cavity,
- m: an integer,

- n: refractive index of the cavity,
- l: optical length of the cavity,
- c: the speed of light in vacuum.

Furthermore [Krauss 2007; Joannopoulos et al. 2008; Robinson et al. 2008; Sünner, et al. 2008; Wang et al. 2008]:

$$\frac{\Delta\omega}{\omega_\circ} = -\frac{\Delta n}{n_\circ} \qquad (23)$$

where:

- ω: the resonance angular frequency of the L3 cavity,
- ω_o: the initial resonance angular frequency of the cavity due to reference conditions,
- n: the refractive index of the cavity,
- n_o: the initial refractive index of the L3 cavity (due to reference conditions),

Combining Equations (22) and (23) yields a relationship in the resonant wavelength, the initial refractive index (of the L3 cavity), and the change in refractive index due to the presence of a gas as [Haus 1985; Sünner, et al. 2008; Robinson 08]:

$$\frac{\Delta\lambda}{\Delta n} = \Gamma\frac{\lambda_\circ}{n_\circ} \qquad (24)$$

where:

- λ_o: the initial resonance wavelength of the L3 cavity (due to reference conditions, e.g. Air),
- n_o: the initial refractive index of the L3 cavity (due to reference conditions),
- Δn: the change in refractive index of the L3 cavity (due to presence of new gas),
- $\Delta\lambda$: the change in resonance wavelength of the L3 cavity (due to presence of new gas).
- Γ = the proportionality constant defined as the interaction factor of the guided modes in the photonic crystal [Robinson 08; Sünner, et al. 2008; Wang et al. 2008]. It is related to the photonic crystal structure and L3 cavity size and geometry. Also called the response factor of the resonator [Sünner, et al. 2008].

Equation (24) is the key equation for understanding how the sensor works: when a new gas is present and fills the photonic crystal holes and the L3 cavity, it changes the refractive index of the cavity from the initial value of n_o to the new value of $\Delta n+n_o$. This in turn changes the resonant wavelength of the L3 cavity from λ_o to $\Delta\lambda+\lambda_o$. Clearly there is a linear relation between Δn and $\Delta\lambda$ which means that the gas sensor is a linear sensor system.

The above analysis is basic and approximate; in particular, the "Γ" factor is a complicated integral that requires a numerical solution [Robinson 08; Sünner, et al. 2008]. In addition, the eventual goal is to fabricate the gas sensor and experimentally

verify its operation and this requires the analysis of the full structure of the sensor including the waveguides and their coupling with the cavity. The best approach in such cases is to perform a numerical Finite Difference Time Domain (FDTD) modelling of the sensor structure to fully understand its behaviour. FDTD is ideal for such purposes and ensures that all behaviours of interest are modelled accurately with the accuracy dependant only on computational power and time constraints [Sullivan 2000]. Its major draw back is that it requires extensive computational power, often in the form of clustered computers and considerably long periods of time to complete the modelling. Over 400 hours were spent modelling various different configurations for the sensor with a decent sized cluster.

3.4.5 Initial Design

An initial "paper" design was carried out to get the initial values for the photonic crystal parameters. Then, these initial values were used to perform a basic FDTD simulation to achieve a better estimate of the values and then performed full FDTD simulations. The tool was CrystalWave made by Photon Design, www.photond.com. It is an FDTD software package that is specifically designed for photonic crystal modelling.

To design and fabricate a photonic crystal, a few critical parameters are required [Joannopoulos et al. 2008]:

1. The dimensional structure: e.g. 2D slab, 3D...etc,
2. The lattice structure: e.g. square, hexagonal,

3. The lattice physical arrangement: e.g. Air holes in a dielectric, dielectric rods in Air,
4. The lattice constant: a,
5. The Air hole radius: r,
6. Slab thickness: t,
7. The operating wavelength bandwidth and specifically, the centre wavelength: λ_c.

The design requirements for the photonic crystal gas sensor include:

1. Band-gap of the photonic crystal should be in the C to L band wavelength range, i.e. 1530 to 1630 nm. This is due to the ease of availability of fibres, laser sources, detectors, and other necessary equipment (e.g. optical spectrum analyzers) in this range. This wavelength range represents the most common operating window for telecommunication and optical networking. Furthermore, this will make it easy to fabricate the gas sensor on a large scale since most of the fabrication technology is optimized for this wavelength range.
2. Sensor should be polarization independent. This is for the laser source part of the sensors. Lasers which do not have their TE vs. TM polarization set are typically cheaper and more widely available.
3. Sensor should be capable of sensing multiple gases. This significantly increases the flexibility of the sensor and allows it to be deployed across different environments with minimum physical changes while keeping the cost low.

4. Temperature independent. Changes in temperature do have an effect on photonic crystals. The best way to achieve temperature independence is to make use of temperature controllers which are standard technology.
5. Pressure independent. Changes in pressure also have an effect on photonic crystals. [Sünner, et al. 2008] observed that the refractive index of photonic crystal resonators has a linear relationship with the ambient pressure. Again, the best way to deal with this is to ensure uniform pressure or alternatively, take into account the pressure effect when observing the output of the sensor.

The requirements above led to the choice of a triangle lattice (also called hexagonal) for the photonic crystal. This has several advantages: first, it has a bigger bandgap and so allows us more flexibility in the selection and optimization of other design parameters, second, a bigger bandgap allows the sensing of a wider range of refractive index changes (from the reference refractive index, e.g. Air) and this allows the sensor to sense a wider range of gases, finally, it is polarization independent compared to the square lattice.

It should be noted that fabrication imperfections will lead to an imperfect triangular lattice which means, among other things, that the photonic crystal gas sensor will not be truly polarization independent; however, the effect is quite small and insignificant for practical purposes, given acceptable fabrication tolerance.

With the aid of Figure 5, which gives a bandgap map of a triangular lattice of Air holes in Silicon [Joannopoulos et al. 2008], the lattice constant of the photonic crystal and the radius of the Air holes can be determined. The TE bandgap is used since it is quite large for the triangular lattice and allows the sensing of more gases. The frequency of 0.25 (i.e. $\frac{\omega a}{2\pi c} = 0.25$) is chosen, since it is near the centre of the TE bandgap and provides maximum tolerance against fabrication imperfections and ensures the photonic crystal has a bandgap when it's fabricated. Using the same logic and $\frac{\omega a}{2\pi c} = 0.25$, a value of 0.3 for the filling factor, i.e. $\frac{r}{a} = 0.3$ is selected.

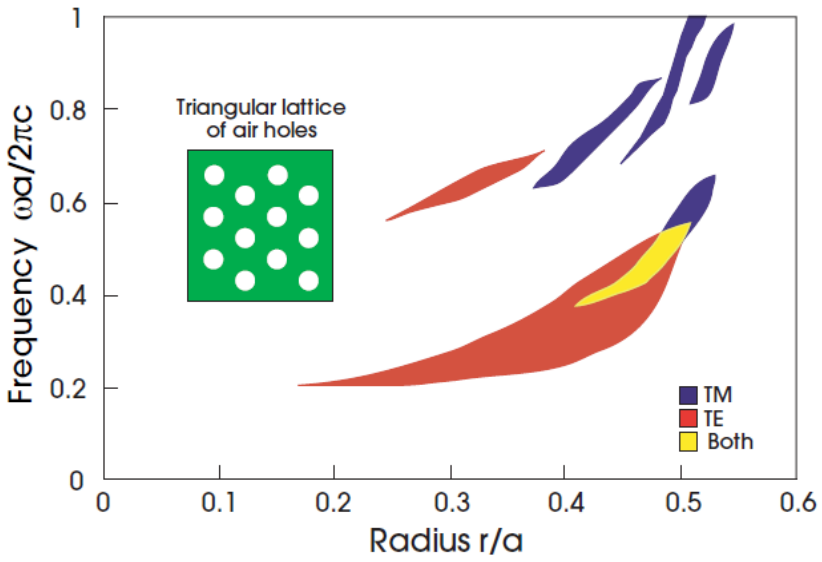

Figure 5: Bandgap map for a triangular lattice of Air holes in silicon (ε = 11.3) [Joannopoulos et al. 2008].

$\frac{\omega a}{2\pi c}$ is called the normalized frequency and can be expressed in another way [Joannopoulos et al. 2008]:

$$\frac{\omega a}{2\pi c} = \frac{a}{\lambda} \qquad (25)$$

Therefore the lattice constant is:

$$0.25 = \frac{a}{\lambda} \qquad (26)$$

$$a = 0.25\lambda, \qquad \lambda_c = 1550nm$$

$$a = 387nm \qquad (27)$$

The initial value of r, the Air hole radius of photonic crystal is thus:

$$\frac{r}{a} = 0.3 \qquad (28)$$

$$r = 0.3a, \qquad a = 387nm$$

$$r = 116nm \qquad (29)$$

The input and output waveguides of the photonic crystal gas sensor is chosen to be a W1.06 [Han et al. 2011]. This means that one row of Air holes is removed and the neighbouring rows are further shifted away by 0.06a. This is chosen over the typical

W1 waveguide (i.e. one row of Air holes removed to form the waveguide) because it has a wider transmission bandwidth (i.e. it can guide more wavelengths) while still maintaining the single mode operation characteristics of the W1 waveguide [Mnaymneh 2009].

The slab thickness of the sensor (i.e. the thickness of the "guiding" layer, which is Silicon in SOI architecture) is chosen to be 0.6a. This value gives the largest bandgap size for a triangular lattice photonic crystal [Johnson et al. 1999]. This is desirable because it increases the sensor bandwidth and allows it to sense a wider range of gases and eases the fabrication tolerances (so fabrication imperfections do not lead to a photonic crystal with no bandgap).

Therefore, t, the slab thickness of the photonic crystal is:

$$t = 0.6a \qquad (30)$$

$$a = 387nm$$

$$t = 232nm \qquad (31)$$

It was learned afterwards that the design rules of the foundry that will fabricate the photonic crystal required a silicon layer thickness of 220 nm [Chrostowski et al. 2010]. Furthermore, this value was set and no additional optimization of it was possible due the fabrication constraints. This required the optimization of other photonic crystal parameters while keeping the slab thickness set at 220 nm.

Since the lattice constant, a, is 387 nm, a 220 nm slap thickness corresponds to a value 0.56a. Fortunately, this is close to the optimal value of 0.6a and also ensures a large bandgap size and therefore should not affect the characteristics of the sensor [Johnson et al. 1999].

Therefore, the new slab thickness of the photonic crystal is:

$$t = 220nm \qquad (32)$$

$$a = 387nm$$

$$t = 0.56a \qquad (33)$$

Finally, the Air bridge structure (also called the Air membrane structure / suspended membrane structure) [Joannopoulos et al. 2008; Han et al. 2011] was chosen. This means that the entire photonic crystal is a membrane (i.e. Air or gas is present on top and bottom of it). This ensures that the photonic crystal is completely symmetric. This is very critical because an asymmetric structure such as Air on top and a semiconductor (e.g. SiO_2) runs the real danger of having no photonic bandgap [Shinya, et al. 2002]. It goes without saying that without a photonic bandgap, the photonic crystal gas sensor will not function. It takes careful design and fabrication efforts to ensure that a photonic bandgap exists for asymmetric structures [Shinya, et al. 2002].

A symmetric structure on the other hand, does not suffer from this issue. This considerably simplifies the design and simulation of the photonic crystal as the field profile is now symmetric and the propagating light experiences the same refractive index. The main drawback of this approach is that it makes the device, less mechanically stable, easier to damage, and it requires more fabrication steps. In fact, the first device fabricated actually failed because the foundry that fabricated it did not carry out the processing step that creates the Air bridge (despite documented requests from the researcher) and a new device was fabricated but with InP instead of SOI due to lack of fabrication facilities as will be discussed later. Figure 6 shows a schematic of Air bridge structure of the photonic crystal sensor. Table 1 summarizes all the initial parameters of the photonic crystal gas sensor.

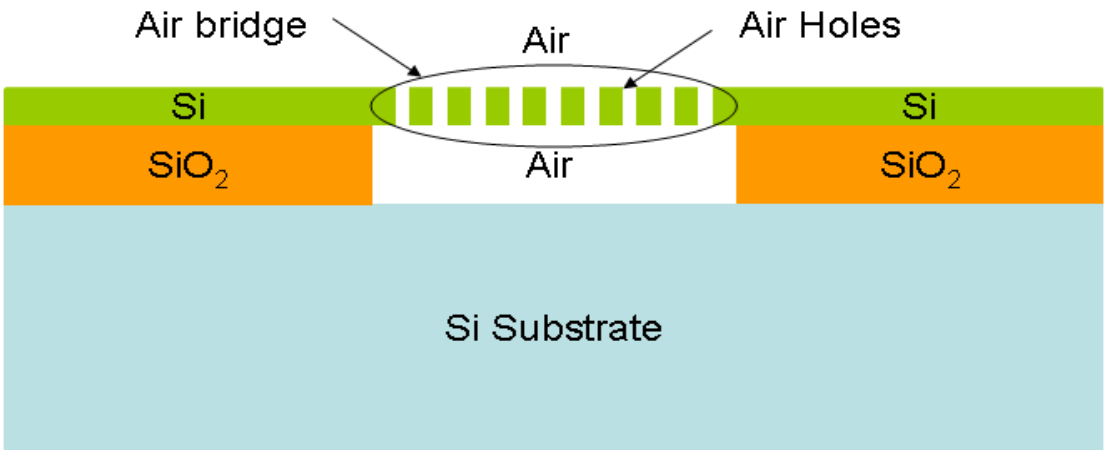

Figure 6: Side view schematic of MG-PhC gas sensor showing the Air bridge.

Table 1: PhC initial parameters.

PhC Parameter	Value
Structure	Air Bridge
Centre wavelength, λ_c	1550 nm
Lattice constant, a	387nm
Filling Ratio, $\frac{r}{a}$	0.3
Hole Radius, r	116 nm
Slap thickness, t =0.56a	220 nm
Input/Output Waveguides	W1.06

Since all the critical parameters have been figured out, the next step is to perform a FDTD simulation to determine the photonic bandgap of the photonic crystal. As mentioned previously, the tool of choice is CrystalWave, a powerful FDTD simulator from www.photond.com that is specifically designed for photonic crystal simulations. FDTD simulations are either 2D or 3D and since the gas sensor is a 2D photonic crystal slab, 2D simulations are appropriate for determining its bandgap. 3D bandgap simulations using CrystalWave will not work because there is no 3D photonic crystal bandgap (i.e. a complete bandgap) in a 2D photonic crystal slab and the sensor structure is a photonic crystal slab.

To perform 2D FDTD simulations for the photonic crystal slab, the effective index method is utilized and effective index values for all interfaces of interest is calculated [Winick 1992; Hammer and Ivanova 2009]. Referring to Figure 6, the effective index for two interfaces needs to be calculated: 1. Air/Si/Air interface (which forms the photonic crystal itself), and 2. Air/Si/SiO2 interfaces (which forms the waveguide). Afterwards, the full sensor structure needs to be simulated in 2D and its photonic bandgap calculated. The effective index for the aforementioned interfaces is calculated using another tool, FIMMWAVE, also from www.photond.com and the results are shown in Table 2.

Table 2: Effective index value for 2D FDTD simulation.

Interface	Effective Index Value
Air / Si / Air (suspended photonic crystal)	2.812763
Air/Si/SiO2 (input/output waveguides)	2.830606

Figures 7 and 8 show the photonic crystal unit cell defined in CrystalWave and the corresponding Brillouin zone (and Γ-K-M direction) respectively. The unit cell must be properly defined in order to accurately simulate the photonic bandgap.

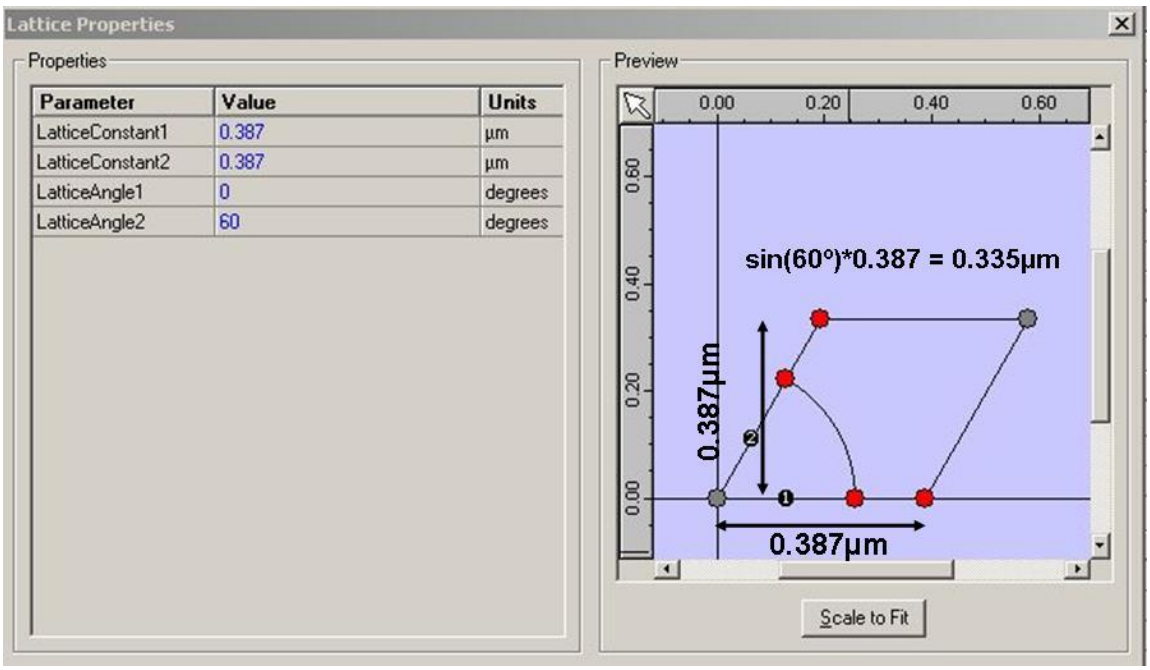

Figure 7: Triangular lattice unit cell of PhC in CrystalWave.

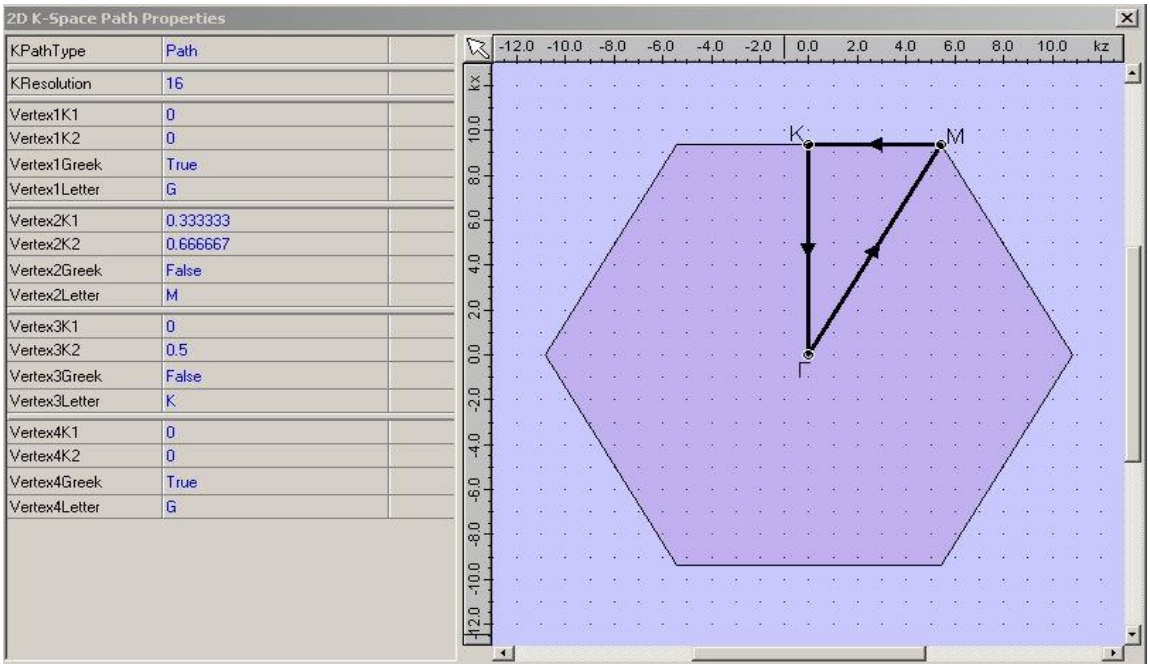

Figure 8: Brillouin zone of the PhC.

Figure 9 shows the simulated photonic crystal bandgap of the sensor with the initial parameters from Table1.

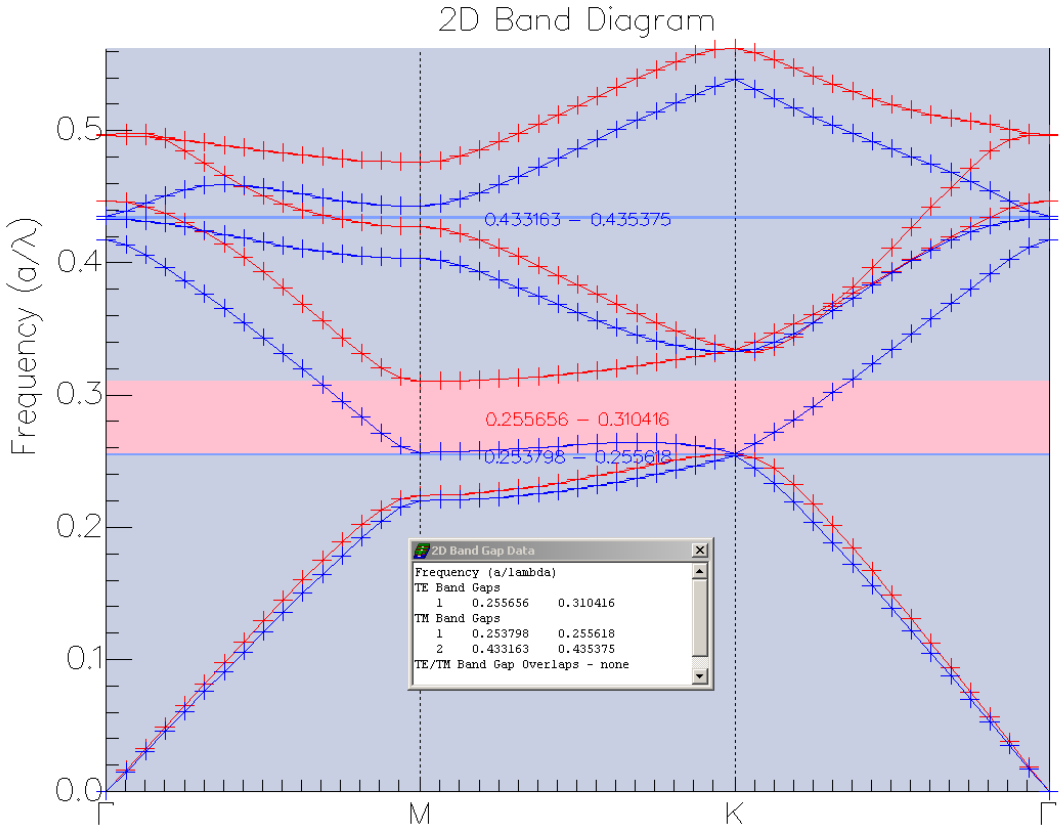

Figure 9: Bandgap of PhC with parameters from Tab e1: a = 387 nm, r = 116 nm.

From Figure 9, it can be clearly seen that several photonic bandgaps exist: one large TE bandgap and two small TM bandgaps with no overlap between TE and TM bandgaps. These results agree with the expected theoretical results of a triangular lattice photonic crystal slab structure [Joannopoulos et al. 2008]. Table 3 gives the normalized frequency ($\frac{a}{\lambda}$) range, of the photonic bandgaps and the corresponding wavelengths range.

Table 3: Photonic bandgap of PhC with parameters from Table 1.

Photonic bandgap	Normalized Frequency range	Wavelength range (μm)
TE	0.255656 to 0.310416	1.2467 to 1.5138
TM 1	0.253798 to 0.255618	1.5140 to 1.5248
TM 2	0.433163 to 0.435375	0.8889 to 0.8957

Recalling that a key design requirement of the photonic crystal gas sensor was that the centre wavelength be 1550 nm, i.e. λ_c =1.55 μm, it can be clearly see from Table 3 that the initial parameters selected for the photonic crystal gas sensor do not give a photonic bandgap that matches this key requirement. Therefore, new parameters need to be selected that will ensure a photonic bandgap which includes λ_c =1.55 μm.

There are three parameters which have the greatest impact on the photonic bandgap: 1. Lattice constant, a, 2. Air hole Radius, r, and 3. Slab thickness, t. The slab thickness is already set by the foundry to 220 nm so the only remaining options are changing the lattice constant and/or the Air hole radius.

A more detailed literature review of previous triangular photonic crystal parameters revealed that a normalized frequency value, $\frac{a}{\lambda} = 0.287$, leads to a photonic band gap that covers the 1.55 μm wavelength, while keeping the filling factor at its original value, $\frac{r}{a} = 0.3$.

Therefore the new lattice constant, and Air hole radius are:

$$0.287 = \frac{a}{\lambda} \qquad (34)$$

$$a = 0.287\lambda, \qquad \lambda_c = 1550nm$$

$$a = 445nm \qquad (35)$$

$$r = 0.3a, \qquad a = 445nm$$

$$r = 133nm \qquad (36)$$

With the new values for a and r, another simulation was run in CrystalWave to determine the 2D photonic bandgap for the photonic crystal. Figure 10 shows the results.

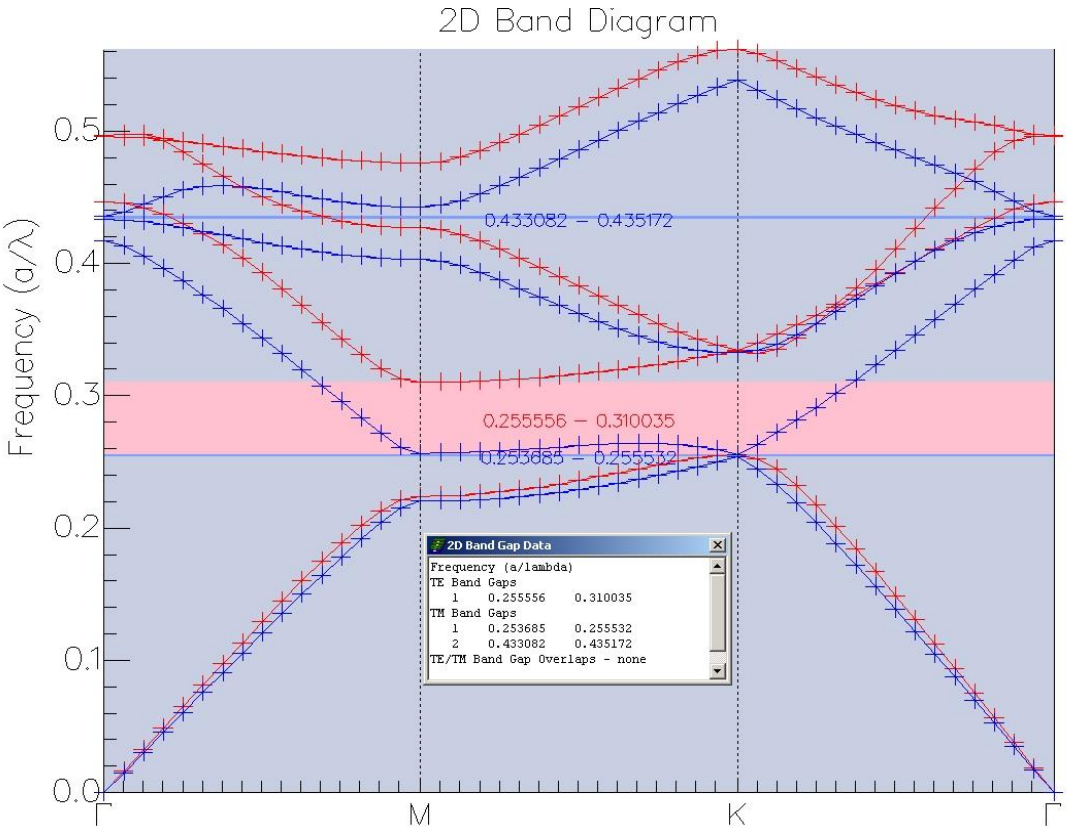

Figure 10: Bandgap of PhC with new parameters: a = 445 nm, r = 133 nm.

From Figure 10, it can be clearly seen that, similar to Figure 9, several photonic bandgaps exist: one large TE bandgap and two small TM bandgaps with no overlap between them. Table 4 gives the normalized frequency ($\frac{a}{\lambda}$) range of the photonic bandgaps and the corresponding wavelengths range.

Table 4: Photonic bandgap of PhC with new parameters a = 445 nm, r = 133 nm.

Photonic bandgap	Normalized Frequency range	Wavelength range (μm)
TE	0.255556 to 0.310035	1.4353 to 1.7413
TM 1	0.253685 to 0.255532	1.7415 to 1.7541
TM 2	0.433082 to 0.435172	1.0275 to 1.0456

It can be clearly seen from Table 4 that λ_c = 1.55 μm falls within the TE bandgap and thus the new parameters of a = 445 nm, and r = 133 nm help satisfy all initial design requirements for the gas sensor. Table 5 summarizes the new and final parameters for the gas sensor. The next step is to perform full 3D FDTD simulations to explore and optimize its behaviour.

Table 5: PhC final parameters.

PhC Parameter	Value
Structure	Air Bridge
Centre wavelength, λ_c	1550 nm
Lattice constant, a	445 nm
Filling Ratio, $\frac{r}{a}$	0.3
Hole Radius, r	133 nm
Slap thickness, t =0.49a	220 nm
Input/Output Waveguides	W1.06

It is worth noting that the ratio of the slab thickness t to the new value of the lattice constant a is: $\frac{t}{a} = 0.49$, which also ensures a large bandgap size and therefore, the sensor's performance does not suffer any serious degradation [Johnson et al. 1999].

3.4.6 FDTD Simulations

3.4.6.1 Initial simulation results

Recall that the gas sensor is based on a photonic crystal slab which uses a hybrid light guiding mechanism: 1. photonic bandgap guiding in the planar direction, and 2. index guiding (i.e. total internal reflection) in the vertical direction. 2D FDTD simulations (which are much faster than their 3D cousins) are not appropriate in this case because they do not model the index guiding in the vertical direction which

affects the input and output waveguides as well as the L3 cavity of the gas sensor. Unfortunately, 3D FDTD simulations are much more time consuming and require significantly greater computing powers than 2D simulations but there is no avoiding them in this case [Sullivan 2000; Qiu 2001]. CrystalWave is capable of running both 2D and 3D simulations in single PC and clustered PC modes. Figure 11 shows the top view of the photonic crystal gas sensor as defined in CrystalWave.

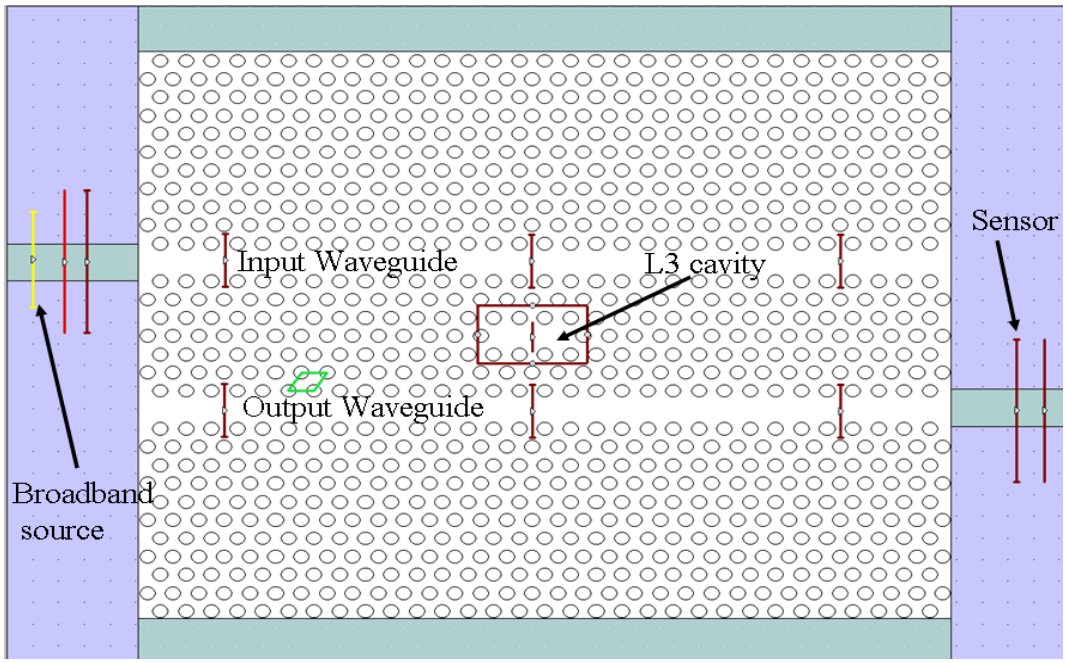

Figure 11: Top view of PhC gas sensor as defined in CrystalWave

Figure 12 shows a side view section of the photonic crystal gas sensor as defined in CrystalWave. The slab thickness (i.e. Silicon layer thickness) was 220 nm, while the SiO_2 layer thickness was 1 μm. The substrate thickness has been set to 1 μm as per the design rules of the foundry.

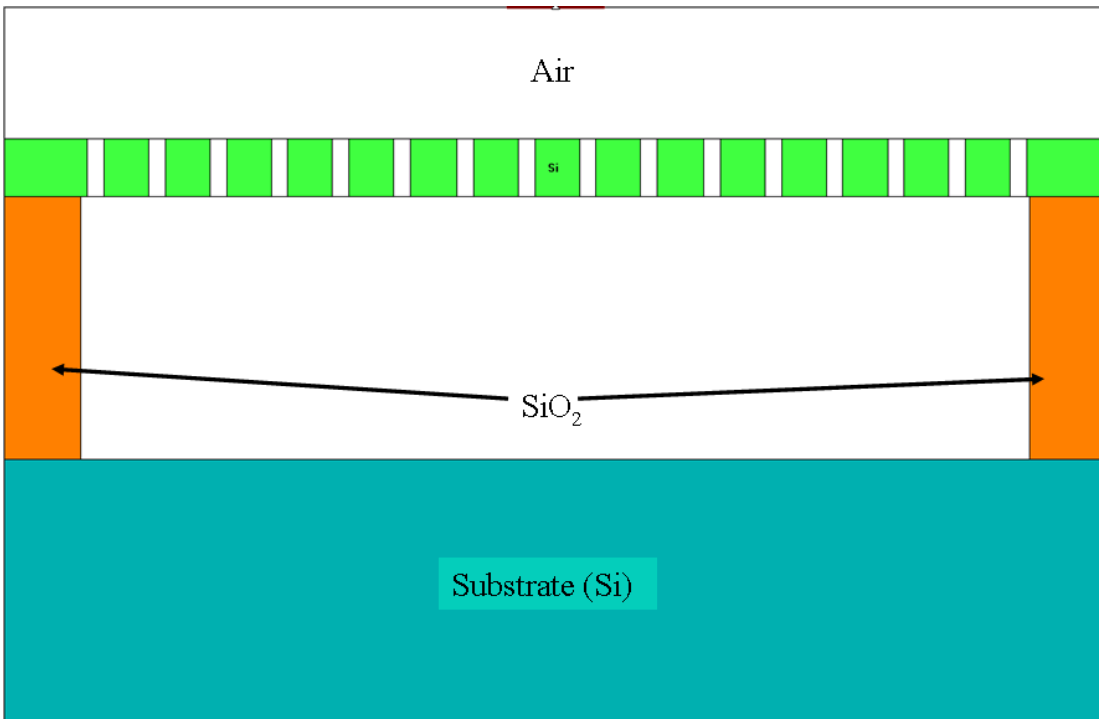

Figure 12: Side view of PhC gas sensor as defined in CrystalWave.

There are a number of key parameters that are essential to any FDTD simulation including: 1. Grid Size, and 2. Simulation time [Sullivan 2000; Qiu 2001]. The grid size determines the accuracy of the simulation, if it is not chosen carefully; the simulation results may be erroneous. The simulation time must be long enough to allow the simulation to reach steady state results. Ideally, it is desirable to reduce the grid size and increase the simulation time to get more accurate results. However, doing so would exponentially increase the time required to complete a FDTD simulation because it require exponentially greater computing power.

Since photonic crystals are periodic structures, it makes sense to choose grid sizes that are fractions of the lattice constant, a. The most commonly used grid sizes seen in literature are: 1. $\frac{a}{12}$, 2. $\frac{a}{16}$, and 3. $\frac{a}{20}$. Other grid sizes are also possible but the

cost in time and computing power exponentially increases as the grid size is reduced. For example, given the same simulation time of 4000 femtoseconds (fs), a simulation of the photonic crystal in Figure 11 with a grid size $\frac{445nm}{12}$ took around 25 hours to complete while a simulation with a grid size of $\frac{445nm}{16}$ took around 45 hours (recall from Table 5 the value of the lattice constant, a = 445 nm).

Various simulation run times were investigated to decide on an appropriate value. Typical FDTD simulations are in the thousands or tens of thousands of fs, particularly for complicated structures like photonic crystals. The appropriate simulation time depends on the simulated structure and is often found by some trial and error until the desired simulation result is obtained [Sullivan 2000; Qiu 2001]. Simulation times of 1000, 2000, 4000 fs for the SOI simulations were investigated.

Initially, the lack of a computer cluster severely limited the ability to run simulations. Often, FDTD simulations are run by a cluster of multi-processor computers to reduce the time requirements. The necessary hardware was not available and CrystalWave did not have (at the time of these simulations) a cluster option. Thus, single pc simulations were run which created severe limitations on the simulation times that could be run. As an example, a single pc could not run any 3D FDTD simulation longer than 4000 fs.

Different approaches were tried to get around this problem by experimenting with different approaches which could reduce the computation and time requirements. The first attempt was to run 2D simulations instead of 3D but with effective refractive indices (see Table 2). A 2D simulation for n = 1 (Air) was run and its results compared with a 3D simulation for n = 1 but the results were significantly different. Different simulation run times and grid sizes were investigated but it was not possible to match the results of the two simulations which convincingly proved that 2D simulations (even with effective indices) are not accurate in this case. The explanation lies in the fact that the Q-factor values in SOI structures are typically high and so out of plane (i.e. in the vertical direction) radiation will be significant. As an example, a value of 4000 was calculated for the Q-factor of the L3 cavity in 3D simulations. This means that 2D simulations, which do not take into account the vertical dimension, will always yield inaccurate results compared to 3D simulations.

Increasing the grid size of the 3D FDTD simulations was attempted as it greatly reduces the time and computation requirements. 3D simulations of the photonic crystal gas sensor (Figure 11) with a grid size of $\frac{445nm}{12}$ were run (it was within the available computational capabilities). However, results for different refractive indices did not show any shift in the resonances of the L3 cavity no matter how long the simulation time (recall the 4000 fs limit due to single pc configuration). It was later found out (after the appropriate simulation parameters were discovered and successful simulations were run) that the $\frac{445nm}{12}$ grid size is too coarse to detect the resonance shift for the gas sensor.

The previous efforts made it clear that the simulations will only be successful if: 1. Grid size of $\frac{445nm}{16}$ and smaller was used, 2. 3D simulations were performed, and 3. Simulation run times of 2000-4000 fs or greater were run. All of this ideally required a cluster of computers and at minimum, required a more powerful single pc with multiple processors. Such a computer was finally secured (dual core with greater memory capacity) and the aforementioned parameters were used for all subsequent simulations discussed in this section. However, 4000 fs run time limit still held.

Simulations were carried out to compare the response of the sensor to two refractive indices: 1. n = 1 (Air, reference), and 2. n = 2. These values were chosen to investigate the sensor's performance at the extreme edges of potential refractive index values and to obtain a quick confirmation of theory of operation of the sensor. It is worth noting that a refractive index of 2 is only possible for some liquids and not gases. The L3 cavity's resonances for both values of refractive index are shown in Figure 13 and Figure 14.

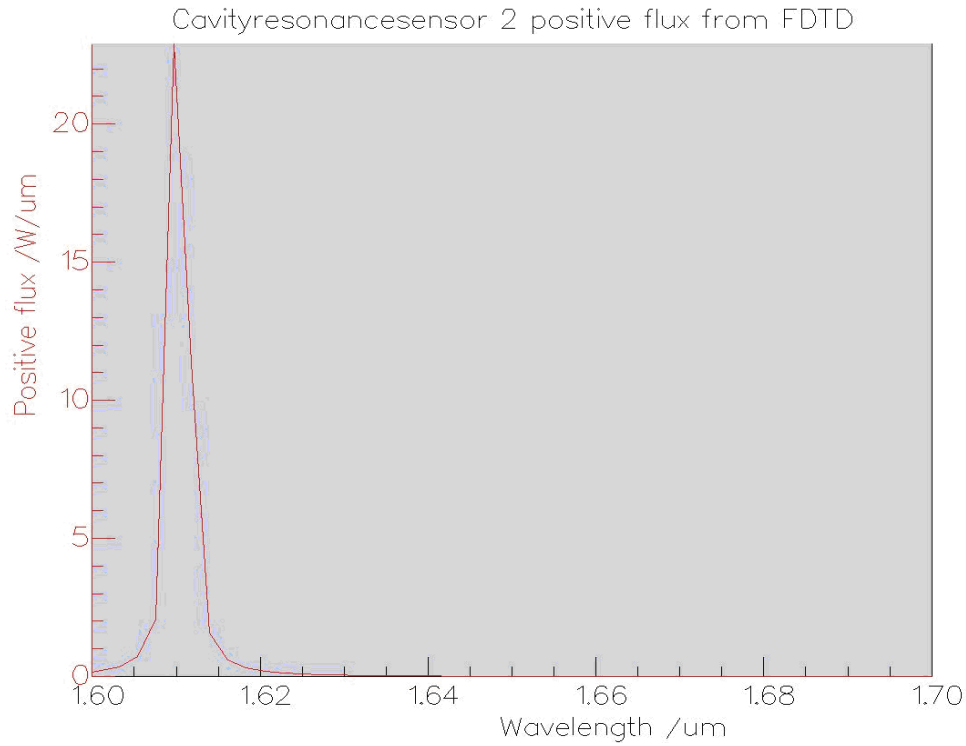

Figure 13: PhC L3 cavity resonance for refractive index value n = 1.

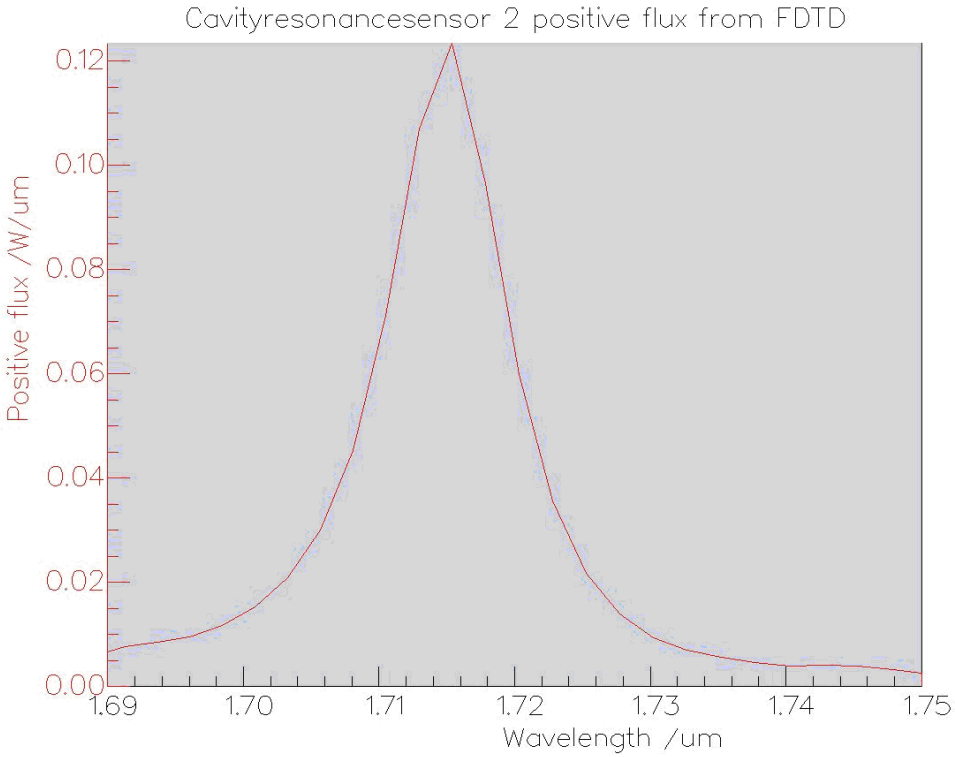

Figure 14: PhC L3 cavity resonance for refractive index value n =2.

The last two figures confirm the basic operation of the sensor: a change in the refractive index of the photonic crystal (due to presence of a new gas) leads to a change in the resonance of the L3 cavity. A refractive index change of $\Delta n = 1$ leads to a resonant wavelength change of $\Delta\lambda = 1$ μm approximately.

The next step is to select a candidate gas to test the sensor's performance and then optimize the L3 cavity performance by increasing its Q-factor. Increasing the Q-factor of the L3 cavity will increase the interaction between light and matter which enhances the sensor's performance. Methyl ether gas was selected, with refractive index, n = 1.000891 [Gas Refractive Index]. This gas was selected as it provides one of the largest refractive index differences from Air and would make the optimization of the L3 cavity easier. Future simulations (with InP photonic crystals, discussed in later sections in this chapter) were carried out with other gases that were easier to obtain for lab testing. However, the results from methyl ether simulations are representative of the sensor's performance and provide insight into its capabilities.

3D FDTD simulations of the sensor in Figure 11 for n = 1 (Air) and n = 1.000891 (methyl ether) were performed. The simulation parameters were: 1. 4000 fs run time, and 2. $\frac{445nm}{16}$ grid size. Table 6 summarizes the results. Simulations with with grid size $\frac{445nm}{24}$ were also performed but provided identical results.

Table 6: PhC gas sensor L3 cavity resonance, linewidth, and Q-factor.

Gas	Resonance (nm)	Linewidth (nm)	Q-factor
Air (n = 1)	1616.2	0.403	4010.8
Methyl Ether (n= 1.000891)	1618.6	0.400	4042.1

It is also worth noting that, as typical of cavities, there are some additional "side" resonances but they are very weak and their Q-factors are sub 200 according to the simulation results.

From Table 6, it can be clearly seen that sensor successfully works: for Δn = 0.000891 ($1.000891_{\text{methyl ether}} - 1_{\text{Air}}$), there is a $\Delta\lambda$ = 2.4 nm ($1618.6_{\text{methyl ether}} - 1616.2_{\text{Air}}$). This is an excellent result: a 2.4 nm shift is easily detectable with an Optical Spectrum Analyzer (OSA). Furthermore, the Q-factors of the resonances for both Air and Methyl Ether are high which ensures strong confinement of the light. This important result confirms the operation of the proposed photonic crystal sensor. From Table 6 and using Equation (16), the sensor's sensitivity is calculated to be 3000 nm/RIU, a high value [Zaho et al. 2011]. See Table 24 at end of this chapter provides a comparison of the sensor with other reported work.

Other gas sensing approaches using photonic crystal cavities (of different configurations) reported in literature show wavelength shifts in the 0.1-0.4 nm range which are more difficult to detect with OSA [Sünner, et al. 2008; Jágerská et al.

2010]. The L3 cavity allows for better light matter interactions and thus a greater shift in wavelength for the same refractive index change.

Additionally, this result was obtained with an integrated optical device with dimensions in the millimetres range and a potential cost of a few cents to a few dollars and with low power requirements. Contrasting this with standard gas sensing techniques using spectroscopic approaches which are bulky, heavy, and costs tens of thousands of dollars (and beyond), the proposed photonic crystal gas sensor is a viable alternative to spectroscopic gas sensing techniques which cannot be easily integrated with RF and electronics and are not capable of being used in a wireless sensor network architecture. Finally, the proposed sensor is capable of sensing multiple gases simultaneously with high sensitivity [Awad et al. 2010; Zaho et al. 2011].

3.4.6.2 Optimization of L3 Cavity Q-factor

Several simulations to optimize the Q-factor of the L3 resonances in Table 6 were performed. The goal was to increase the Q-factor of the cavity as much as possible. Increasing the Q-factor ensures a stronger confinement of light in the cavity which increases the light-matter interaction and increases the strength of the coupled light from the cavity to the bottom waveguide in the sensor. Doing so will increase the overall sensor efficiency as well as increase its sensitivity and extend its sensing range.

However, building a high Q-factor nanoscale cavity is challenging. When the cavity size is on the same scale as the optical wavelengths of interest, radiation losses dramatically increase in inverse proportion to the cavity size. This makes it very difficult to build a cavity that is both very small in size and very high in Q-factor [Akahane et al. 2003]. A solution to this trade off was presented in [Akahane et al. 2003], where the Q-factor of a L3 photonic crystal cavity was maximized by gently confining the light in the cavity. This is done by shifting the outermost Air holes that define the L3 cavity by various distances, often different multiples of the lattice constant of the photonic crystal. This approach has proven successful both theoretically and experimentally and was utilized it to dramatically increase the Q-factor of the resonances in Table 6. Figure 15 shows a schematic depiction of the approach in [Akahane et al. 2003] as it applies to the gas sensor as defined in CrystalWave.

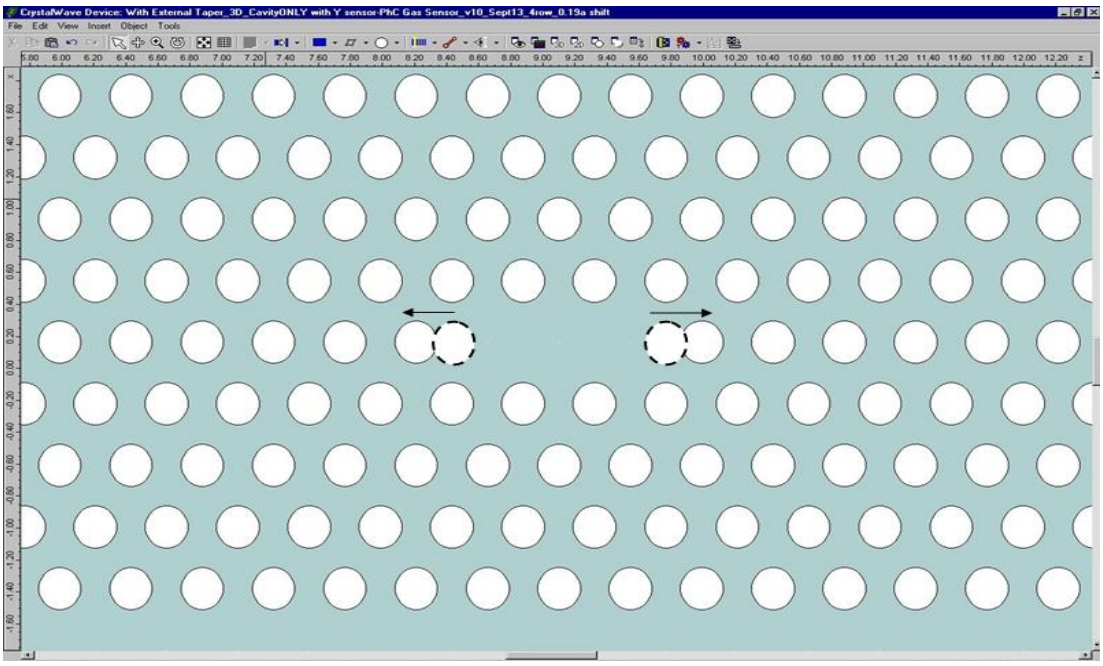

Figure 15: The original (dashed) and final, shifted positions of the outermost Air holes of L3.

Several 3D FDTD simulations were performed to test this concept with n = 1 (Air). Figure 16 shows a graph of the calculated Q-factor vs. the L3 cavity Air hole shift and Table 7 summarizes the full results.

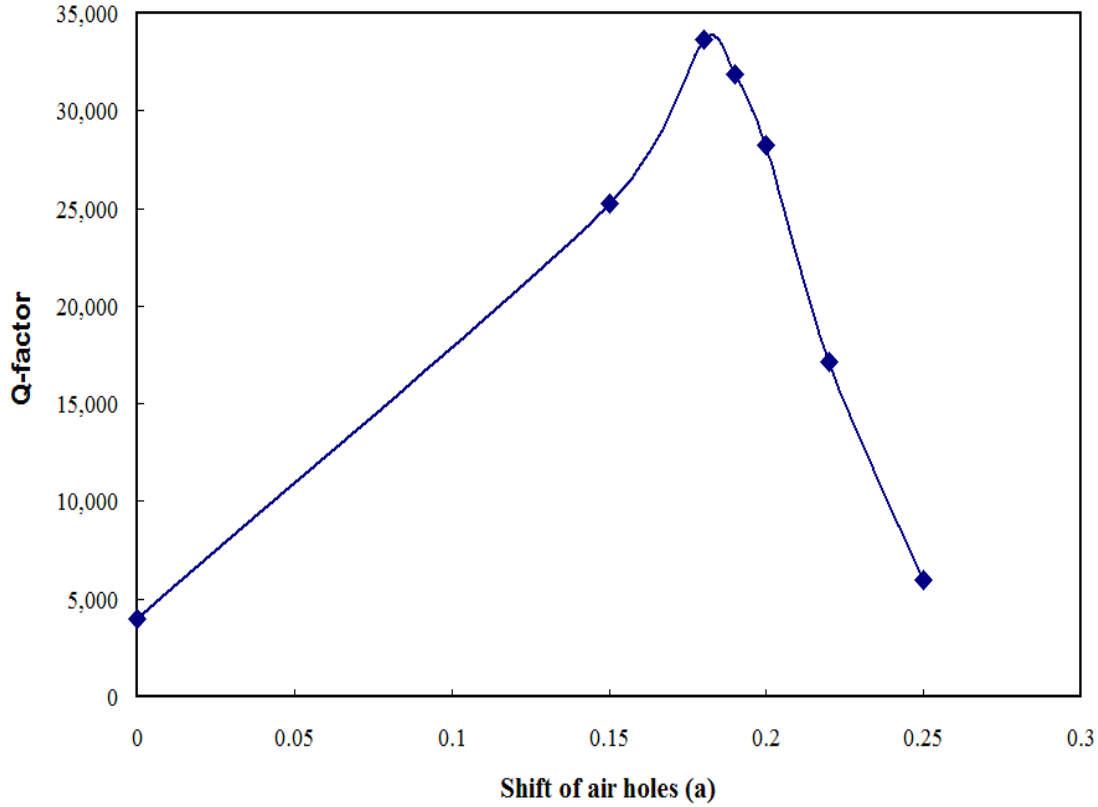

Figure 16: Q-factor of the resonances of L3 cavity due to shifting of the outermost Air holes for n =1 (Air)

Table 7: Air hole shift, L3 cavity resonance, linewidth, and Q-factor for n = 1 (Air).

Air holes shift (a)	Resonance (nm)	Linewidth (nm)	Q-factor
0	1616.2	0.403	4,013.2
0.15	1626.8	0.064	25,269
0.18	1627.8	0.048	33,665
0.19	1628.2	0.051	31,902
0.2	1628.4	0.057	28,246
0.22	1628.8	0.095	17,121
0.25	1628.6	0.297	5,945.8

Clearly, the Q-factor of the cavity increased significantly, from ~ 4000 with no shift up to ~33,000 with a 0.18a shift (corresponding to ~ 80 nm). This is an 8 fold increase! However, increasing the shift past a certain optimum distance causes degradation in both the Q-factor and linewidth of the L3 resonance. This behaviour is similar to what was reported in [Akahane et al. 2003].

Therefore, from the simulation results, it can be concluded that, to optimize the L3 cavity of the gas sensor, an outwards shift of 0.18a (80 nm) of the Air holes that define the L3 cavity is needed. This will result in a resonance with a Q-factor of 33,665 and 0.048 nm linewidth which are the optimum values for the gas sensors (these values are based on n = 1).

Finally, FDTD simulation of the gas sensor with the optimized L3 cavity but with methyl ether gas (n = 1.000891) were carried out in order to compare the results with Air. Table 8 gives a comparison between the un-optimized and optimized L3 cavities for Air and methyl ether. In both cases, the shifting of the L3 cavity outwards by 0.18a dramatically increases the Q-factor.

Table 8. Comparison of PhC L3 resonances for Air and Methyl Ether.

Gas	Shift (a)	Resonance	Linewidth (nm)	Q-factor	$\Delta\lambda$
Air	0	1616.2	0.403	4,010.8	$\Delta\lambda$ = 2.4 nm
Methyl Ether	0	1618.6	0.400	4,042.1	
Air	0.18	1627.8	0.048	33,665	$\Delta\lambda$ = 2.5 nm
Methyl Ether	0.18	1630.3	0.048	34,175	

Table 8 also shows the effect of optimizing the Q-factor on the performance of the gas sensor. Increasing the Q-factor by 8 fold (from ~ 4000 to ~ 33,000), increased the wavelength shift, $\Delta\lambda$ by 0.1 nm (from 2.4 to 2.5 nm). While this value may seem small, it is important to compare it to other published results which have gas sensors with $\Delta\lambda$ on the order of 0.2-0.4 nm and so the increase is significant [Sünner, et al. 2008; Jágerská et al. 2010]. Furthermore, such a dramatic increase on the Q-factor helps to significantly increase the coupling efficiency from the L3 cavity to the output waveguides which increases the overall efficiency of the gas sensor. This concludes the simulations of the SOI gas sensor.

3.4.7 Mask Design

A fabrication mask for the multi-gas photonic crystal (MG-PhC) sensor was designed using a specialized physical layout and verification software for micro-electronics and photonic circuits called dw-2000^{TM}. It is built by Design Workshop technologies (www.designw.com).

Our research group; the Centre for Research in Photonics, CRPuO (www.photonics.uottawa.ca), had formed a partnership with CMC Microsystems (www.cmc.ca), a quasi autonomous non-governmental organisation which provides access to microsystems technology. CMC and the University of British Columbia created a partnership that offered a unique graduate course in silicon nanophotonics fabrication [Chrostowski et al. 2010]. All fabrication efforts for the SOI photonic crystal gas sensor were carried out at IMEC (www.imec.be), Europe's largest independent research centre in nano-electronics and nanotechnology [Chrostowski et al. 2010].

The research group took part of this course and CMC subsidised the fabrication costs for the SOI photonic crystal gas sensor (the InP gas sensor was fabricated elsewhere as discussed in a later section). The gas sensor was part of a multi-project SOI wafer (there was a total of 23 designs on the wafer) that was fabricated using IMEC's passive photonic SOI process, which was accessed through the European silicon photonics prototyping service ePIXfab [Chrostowski et al. 2010].

IMEC's technology is based on a CMOS process, the lithography relies on a 193 nm deep UV lithography which enables features as small as 120 nm (which are well below the photonic crystal critical features). The designs were fabricated on 200 mm SOI wafers with a 220 nm crystalline top silicon film (which, in this case, forms the photonic crystal slab) and a 2000 nm buried oxide. The IMEC foundry is quite flexible and offers a variety of choices in process steps including both shallow and deep etches. The process yields waveguides with propagation losses of 2.5 dB/cm [Chrostowski et al. 2010].

The unit cell design of the gas sensor is shown in Figure 17. Tapered waveguides for the input and output of the photonic crystal were used in order to ensure smooth transitions and mode matching between the optical mode of the fibre and the fundamental mode of photonic crystal waveguides.

Two different sections on the wafer were assigned for different design variations of the gas sensor. Their dimensions were 2 x 6 mm. Several different design variations were created including: varying the separation distance between the waveguides and the L3 cavity from 4 to 10 Air holes rows (to test waveguide/cavity coupling behaviour), varying the L3 Air hole shift (to test various Q-factors), and varying the width of the waveguides (W1.06 and W1.09) . In total, 40 variations were created. Tables 9 and 10 summarize all the design variations that were created in dw-2000 and were fabricated in the mask.

Table 9: Summary of all PhC structures that form section 1 of the fabrication mask.

Structure	Symbol	# of rows	Shift (a)	Waveguide width
1	4-0-.6	4	no	1.06
2	4-18-.6	4	0.18	1.06
3	4-18-.9	4	0.18	1.09
4	4-16-.6	4	0.16	1.06
5	4-15-.6	4	0.15	1.06
6	5-0-.6	5	no	1.06
7	5-18-.6	5	0.18	1.06
8	5-18-.9	5	0.18	1.09
9	6-0-.6	6	no	1.06
10	6-16-.6	6	0.18	1.06
11	6-16-.9	6	0.18	1.09
12	7-0-.6	7	no	1.06
13	7-18-.6	7	0.18	1.06
14	4-18-6F	7	0.18	1.06
15	8-0-.6	8	no	1.06
16	8-18-.6	8	0.18	1.06
17	9-0-.6	9	no	1.06
18	9-18-.6	9	0.18	1.06
19	10-0-.6	10	no	1.06
20	10-18-.6	10	0.18	1.06

Table 10: Summary of all PhC structures that form section 2 of the fabrication mask.

Structure	Symbol	# of rows	Shift (a)	Waveguide width
21	4-18-.6S	4	0.18	1.06
22	5-18-.6S	5	0.18	1.06
23	6-18-.6S	6	0.18	1.09
24	7-18-.6S	7	0.18	1.06
25	8-18-.6S	8	0.18	1.06
26	9-18-.6S	9	0.18	1.06
27	10-18-.6S	10	0.18	1.06
28	+++	NA	NA	NA
29	R T	NA	NA	NA
30	++	NA	NA	NA
31	T W1.06	NA	NA	NA
32	W1.06 PC	NA	NA	NA
33	5-18-.9-L.6	5	0.18	1.09
34	4-0-.6-L.6	4	no	1.06
35	4-18-.6-L.6	4	0.18	1.06
36	4-18-.9-L.6	4	0.18	1.09
37	4-18-.6-L.9	4	0.18	1.06
38	7-18-.6-L.6	5	0.18	1.06
39	9.18-.6-L.6	5	0.18	1.06
40	10.18-.6-L.6	5	0.18	1.06

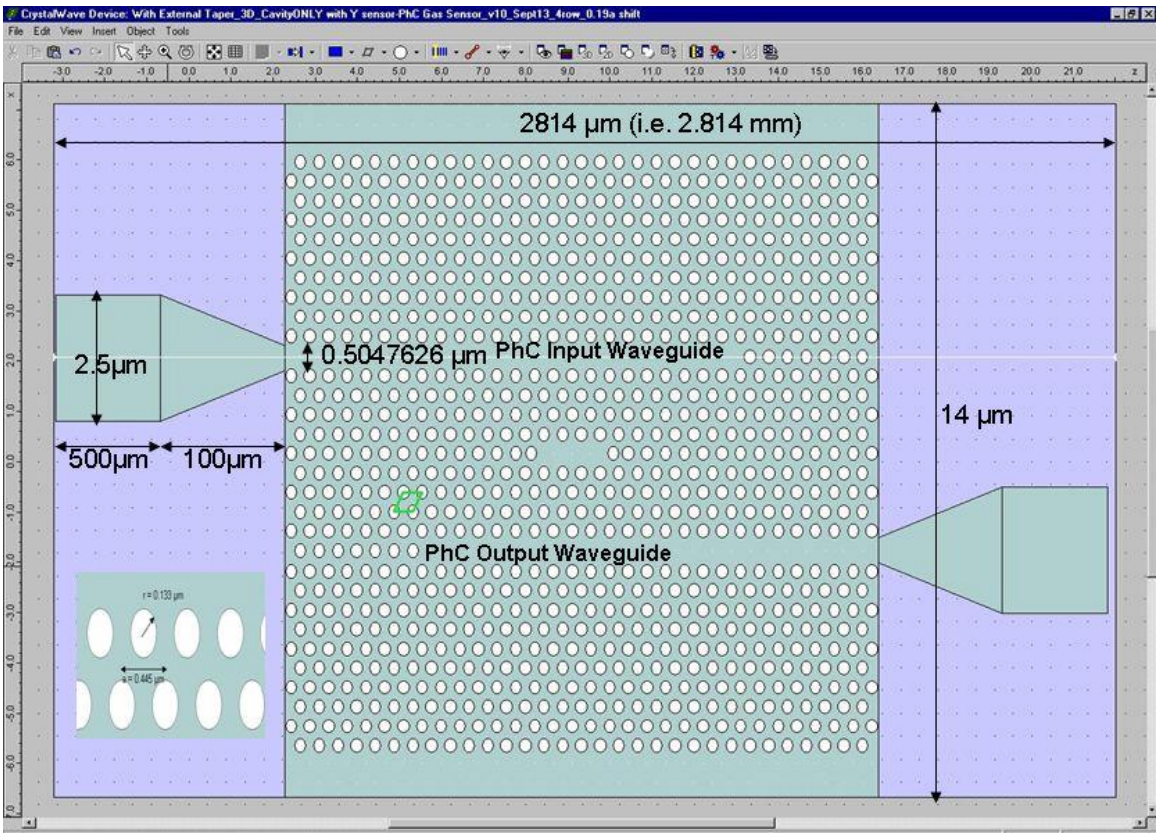

Figure 17: Full MG-PhC gas sensor with dimensions (one single unit). Insert shows dimensions of photonic crystal.

The top part of figure 18 shows the complete SOI wafer that was fabricated by IMEC, with all the 23 different student designs [Chrostowski et al. 2010]. The two sections that make up the 40 design variations are marked by dashed circles. The bottom part of Figure 18 shows an enlarged view of section 1 of the design (in dw-2000 for better illustration). This corresponds to design variations 1 to 20 of Table 9. Figure 19 shows Figure 18: **Bottom** divided into two sections: left hand side, and right hand side to better illustrate the features of the gas sensor.

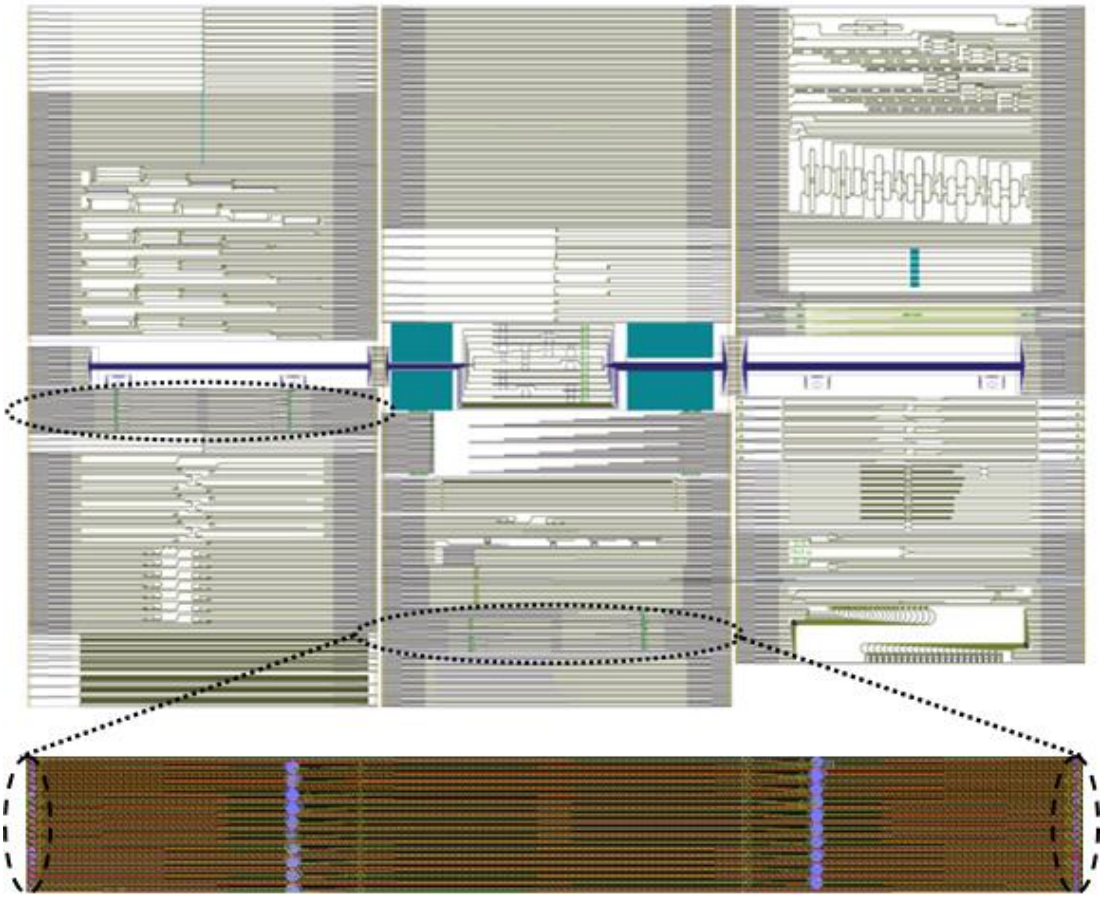

Figure 18: **Top:** Complete SOI wafer fabricated by IMEC showing all student designs. Our two sections are in dashed circles [Chrostowski et al. 2010]. **Bottom:** Enlarged view of section 1 of our designs shown in dw-2000. This section corresponds to design variations 1 to 20 in Table 9. The vertical fibre coupler array is marked by dashed circles.

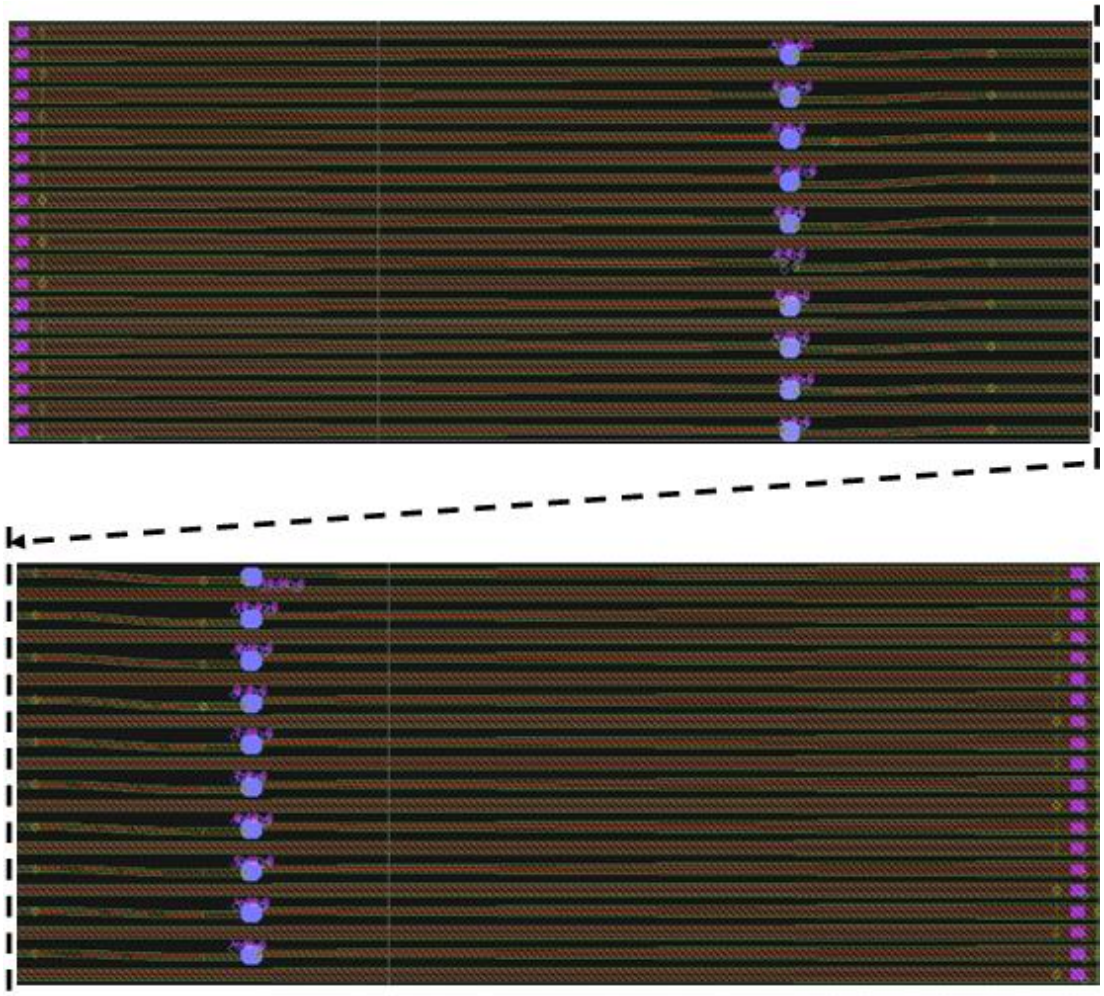

Figure 19: **Top:** Left hand side of Figure 18 bottom in dw-2000. **Bottom**: Right hand side of Figure 18 bottom in dw-2000.

One of the main draw backs of high index contrast structures, such as SOI, is the large mismatch in the mode size and mode shape of the fundamental mode of SOI photonic crystal waveguides and the mode of optical fibres. Furthermore, photonic crystals and other structures like photonic wire waveguides are often small in dimensions. This creates many challenges in coupling the light from single mode fibre to photonic crystal waveguides using the traditional, edge/planar coupling

techniques, even with the use of tapered fibres. Precise alignment is crucial and any misalignments, even very minor ones, lead to significant coupling losses.

Vertical fibre grating couplers have been proposed to deal with these challenges and are designed to make it easier to couple light into and out of photonic crystal waveguides [Roelkens et al. 2007; Vertical Coupler 1; Vertical Coupler 2; Vertical Coupler 3]. They are very compact and have a large optical bandwidth and have the added advantage of not requiring the cleaving of the devices for optical coupling, which enables wafer-scale testing of the integrated circuits, a key requirement for low cost packaging. The SOI wafer fabricated by IMEC made use of vertical fibre coupler technology [Chrostowski et al. 2010]. They were predefined as part of the master mask as an array on both sides of the mask as shown by dashed circles in Figure 18: **Bottom**. Figure 20 shows some vertical grating couplers as designed in dw-2000.

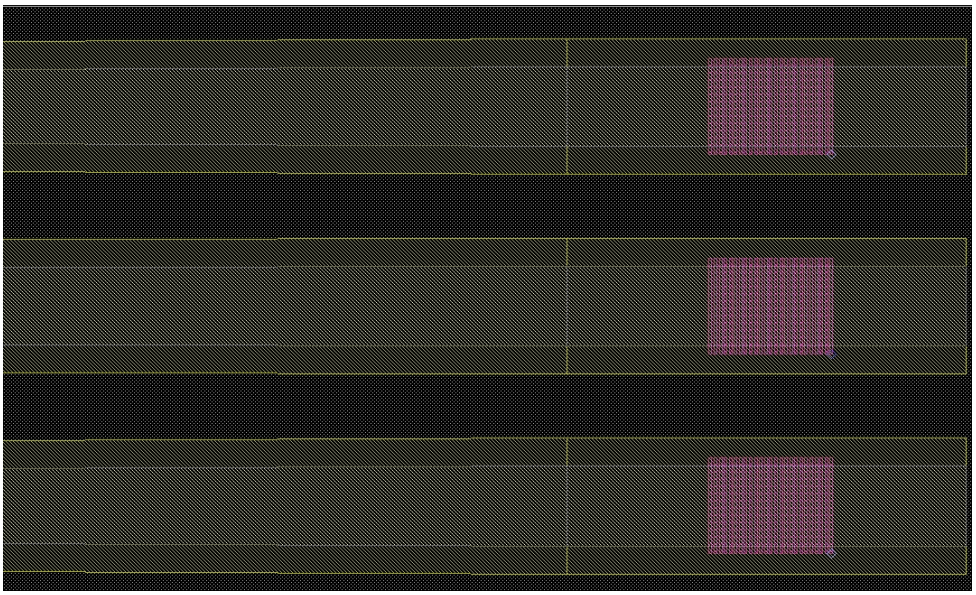

Figure 20: Vertical grating couplers as designed in dw-2000.

Figure 21 shows an enlarged view of a part of section 1 of the design as created in dw-2000. Design variations #2, #6, #10, and #16 from Table 9 are shown. The S-bend structure was used to ensure that both the input and output tapered waveguides of the photonic crystal are aligned with the vertical coupler array that came predefined by IMEC's master mask. The S-bend allows for a smooth transition that minimizes losses. This concludes the fabrication discussion.

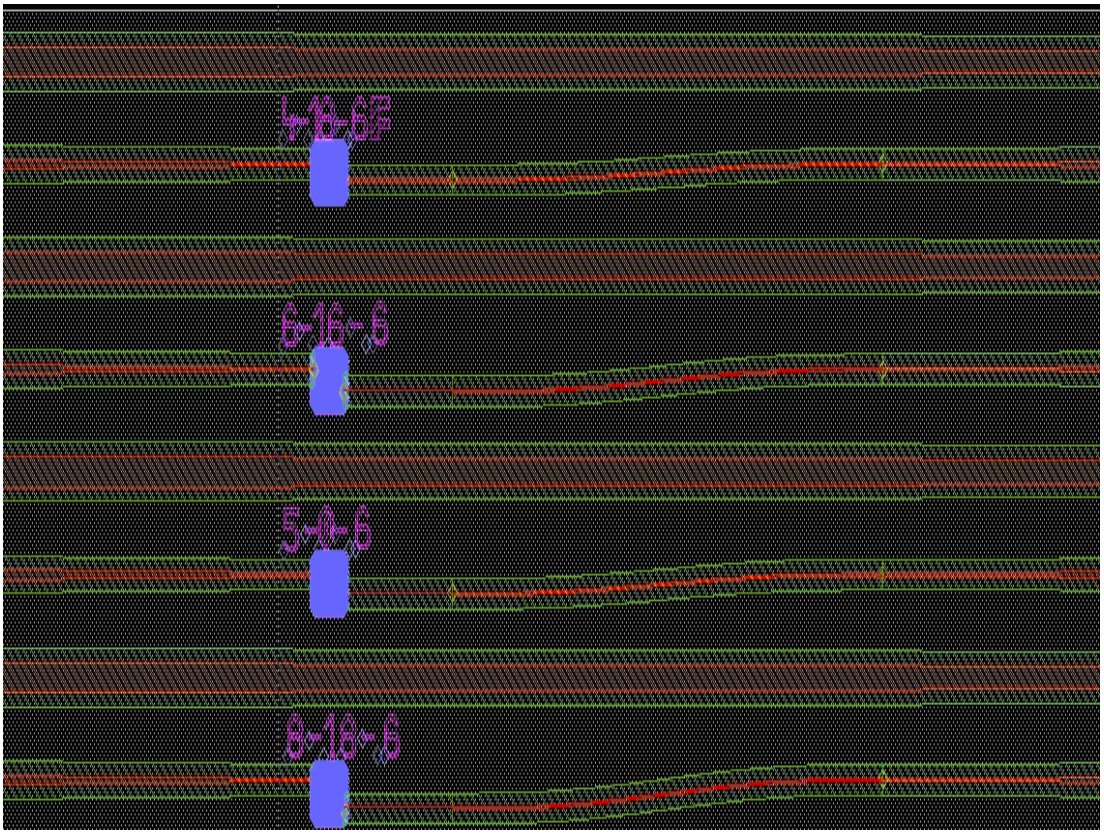

Figure 21: Enlarged view of section 1 of PhC mask showing design variations #2, #6. #10 and #16 from Table 9 as created in dw-2000 software.

3.4.8 Experimental Results

In this section, the experimental results of testing the SOI multi-gas photonic crystal sensor are discussed. 40 variations of the sensor were designed in two separate sections (20 design variations each) in the complete SOI wafer (Figure 18). Figure 22 shows the actual image of the complete SOI wafer using a microscope. Due to field of view limitations, the complete wafer image was divided into 4 parts. The photonic crystal gas sensors are marked with dashed circles.

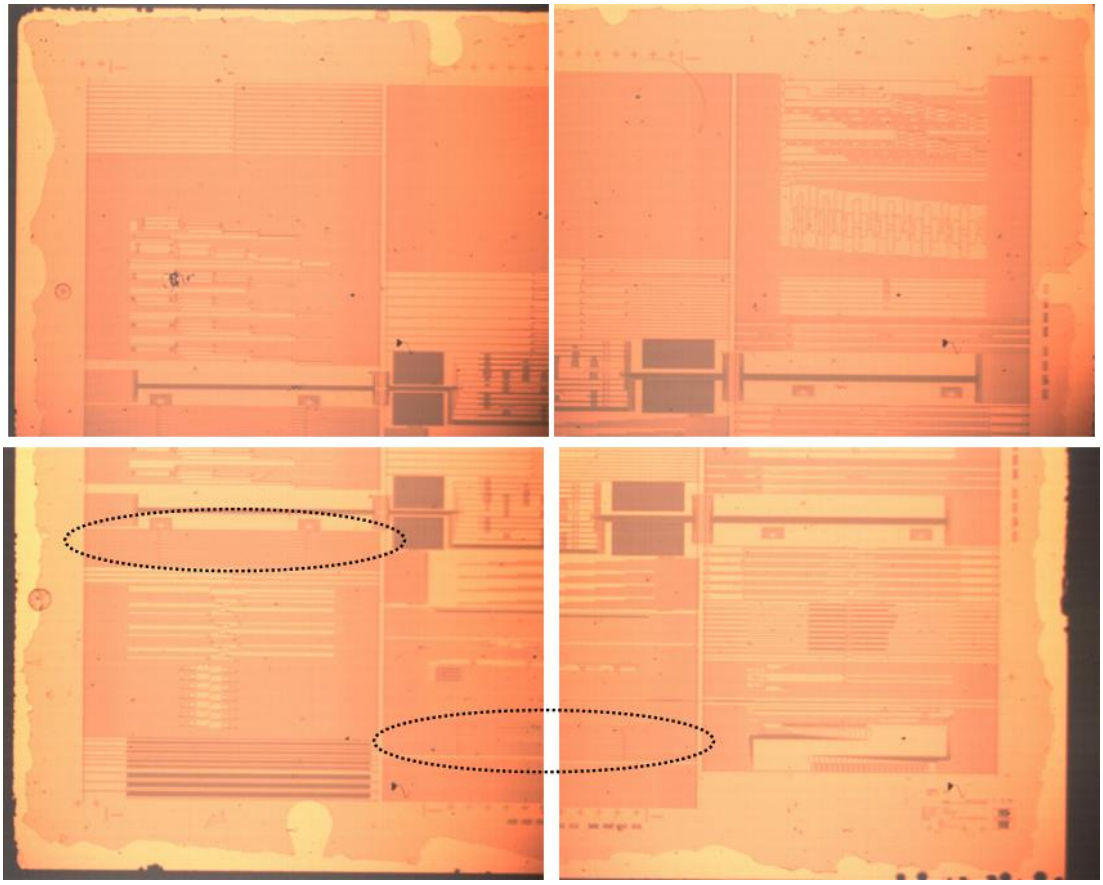

Figure 22: Microscope view (divided into 4 parts) showing the complete SOI wafer fabricated by IMEC with all 23 student designs. The PhC gas sensors are marked in dashed circles.

Great difficulties were encountered in the initial testing of the SOI chip at the home laboratory. Aligning the input fibres to the vertical grating coupler was very difficult due to the nature of the gratings and the lack of a proper alignment setup. The gratings had very small dimensions and required very precise alignment: any minor vibrations in the fibres led to misalignment and it was impossible to couple light from the input tapered fibre to the input photonic crystal waveguide. Ironically, vertical grating couplers were supposed to solve this exact issue, however due to the dimensions of the photonic crystal, they were of little help (compared to the traditional in-plane coupling). It is important to note that the lack of a nano-precision mechanical vertical fibre alignment setup (the setup at the home laboratory was obsolete and not precise enough) was the main culprit for the great difficulties encountered in the initial setup.

It was decided to continue the testing at a different facility. CMC Microsystems operated a photonics laboratory called Advanced Photonics Systems Lab, APSL (www.cmc.ca/en/whatweoffer/test/nmptc/apsl.aspx) at Queens University and kindly offered its use. They had access to better equipment including a better positioning system. At APSL, coupling light to and from the photonic crystal waveguides was finally successful, although the process was very tedious and time consuming. Their positioning system was designed for in-plane light coupling and had to be modified for vertical light coupling which significantly complicated and lengthened the process. Figure 23 shows the setup used for testing at APSL. Two pre-amplifiers, JDS OAB 1590 and JDS OAB 1594, were used to boost the signal from the input broadband laser source, JDS BBS 1590. This laser source emitted between 1440 and

1630 nm. An Optical Spectrum Analyzer (OSA) with a built in but separate power meter, Agilent 8164B, was used to aid in coupling the input light to the vertical grating while a wavelength meter, Agilent 86122A, was used to accurately measure the wavelength of the output signal. A CMC designed test fixture held the photonic crystal chip sample and two positioner fixtures (for vertical coupling) were used for input and output fibre alignment. The Agilent 86122A wavelength meter had a noise floor of -50 dBm, while the Agilent 8164B power sensor had a noise floor of -110 dBm.

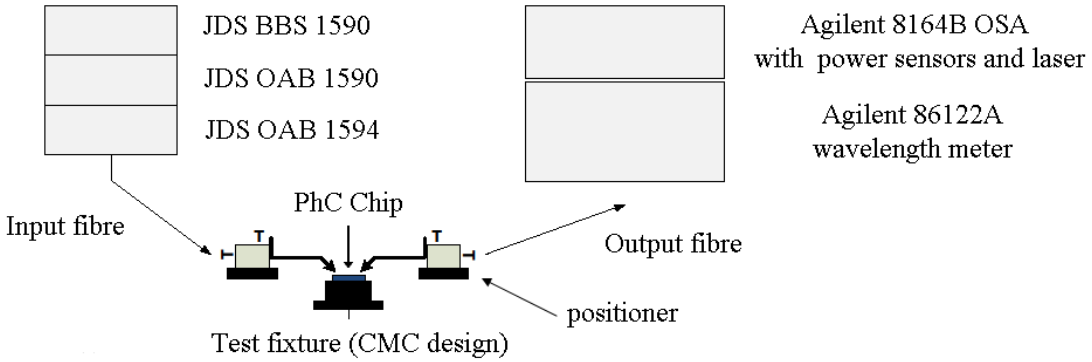

Figure 23: Test setup for PhC SOI chip at CMC's APSL at Queen's university

The simulations in section 3.4.6 predicted that the resonance of the un-shifted L3 cavity of the photonic crystal gas sensors would be in the L-band, around 1616 nm for Air (Table 6). With the setup in Figure 23, the input power (to be coupled to the input vertical grating coupler) at wavelength 1616 nm was approximately 2 dBm (the input signal was broadband covering wavelength range 1440-1630 nm). Surprisingly, the output power at 1616 nm was approximately -55dBm and repeated attempts to optimize the coupling and minimize losses in the setup failed to improve this number. The setup in Figure 23 had a total loss of approximately 20 dB (and 30 dB

in worst case). This meant that the output power should nominally have been -18 dBm (and -28 dBm in the worst case).

Furthermore, it seemed that wavelengths in the C-band (1530-1560 nm) were passing better (i.e. experiencing lower losses) through the photonic crystal. This also did not agree with the simulations of the resonance frequency of the L3 cavity. Figure 24 shows a spectrum plot of the output of the photonic crystal as viewed on the OSA (Agilent 8164B).

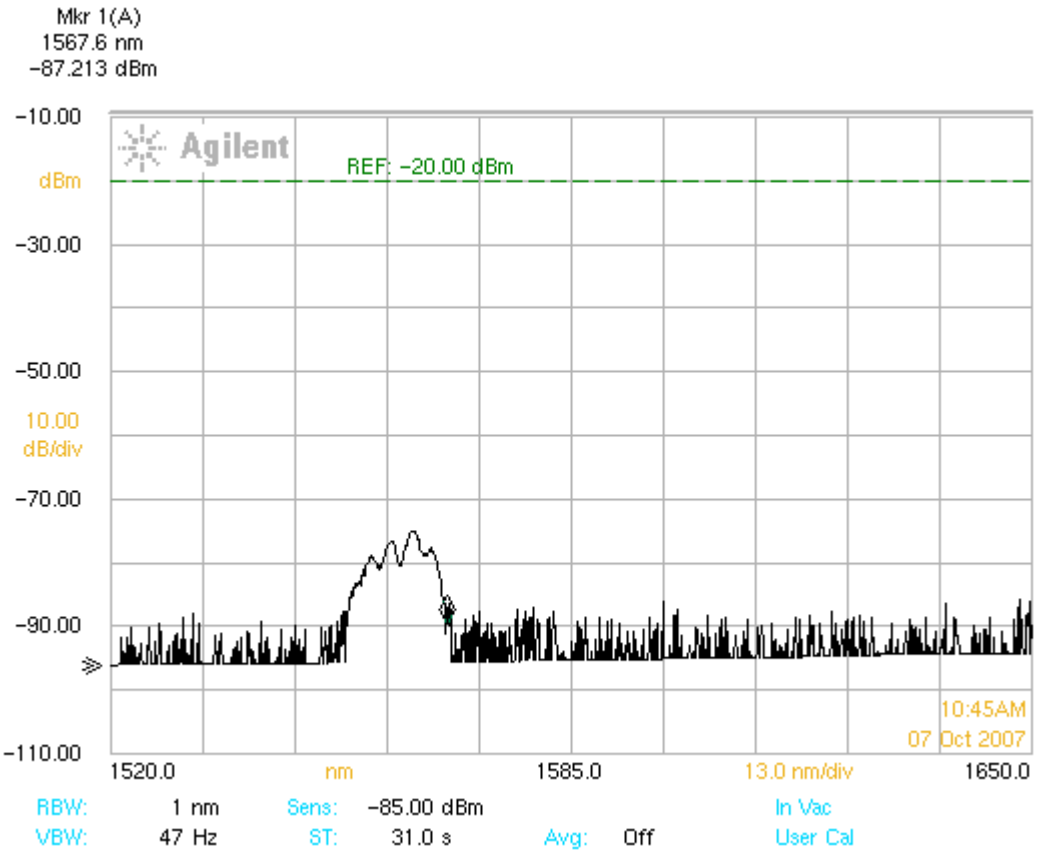

Figure 24: Output of the photonic crystal gas sensor as viewed on the OSA (Agilent 8164B). Input laser is broadband 1440-1630 nm with power of 2 dBm at 1616 nm. Wavelength in C-band (1530-1560 nm) are experiencing lower losses than other wavelengths.

Additional investigation revealed that the vertical grating couplers were designed for the C-band: i.e. they would only allow C-band wavelengths and filter out all other wavelengths This critical fact was not communicated to us and unfortunately, it was not caught by anyone before the fabrication run. This explained the results in Figure 24: C-band wavelengths were propagating through the photonic crystal while all other wavelengths were filtered.

The only solution was to remove (by cleaving) the vertical grating couplers so in-plane couple the light to the photonic crystal waveguides can be done. However, the small dimensions of the photonic crystal and the vertical couplers (roughly 10 x 10 μm) made manual cleaving impractical: the facet quality would have been very poor making coupling the light into the waveguides nearly impossible. Fortunately, CMC very kindly offered to help us deal with this situation. They were experimenting with a new laser-assisted cleaving technology for SOI devices and the photonic crystal sensors were excellent candidates for them to test their technology [Laser Cleave].

Due to cost constraints, only one of the two sections that make up the 40 design variations of the sensors could be cleaved. It was necessary to specify the exact location for the cleaving/dicing to take place. Figures 25 and 26 illustrate the dicing lines that the laser traced to perform the cleaving. The cleaving distance was 100 μm from the edges of the photonic crystal (Figure 26) which still allowed enough distance for smooth mode matching between the input fibre mode and photonic crystal waveguide mode (roughly 500 μm).

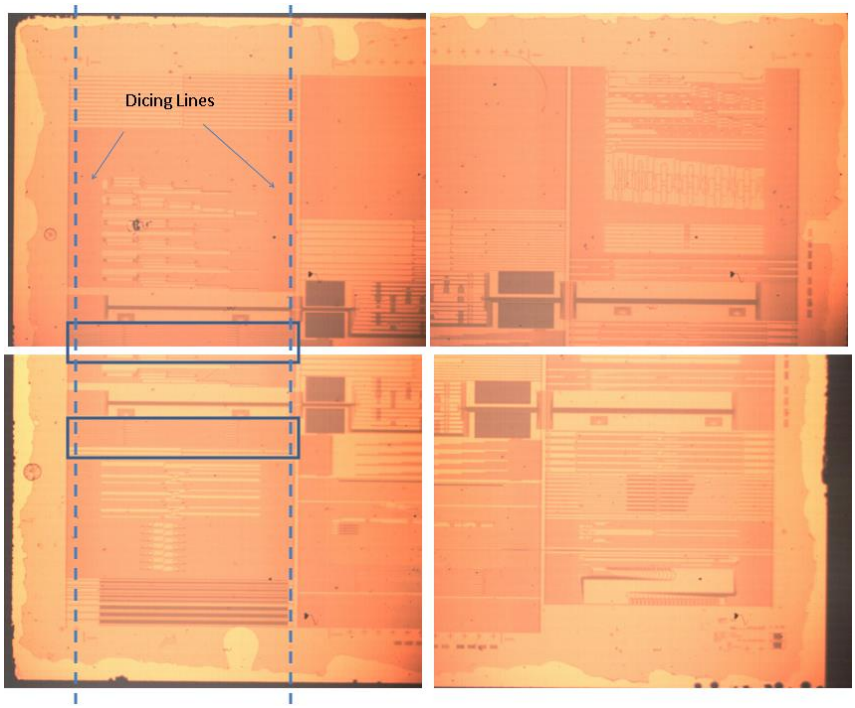

Figure 25: Microscope view of complete SOI wafer showing dicing line for section 1 (design variations 1-20, Table 9) of PhC for laser assisted cleaving.

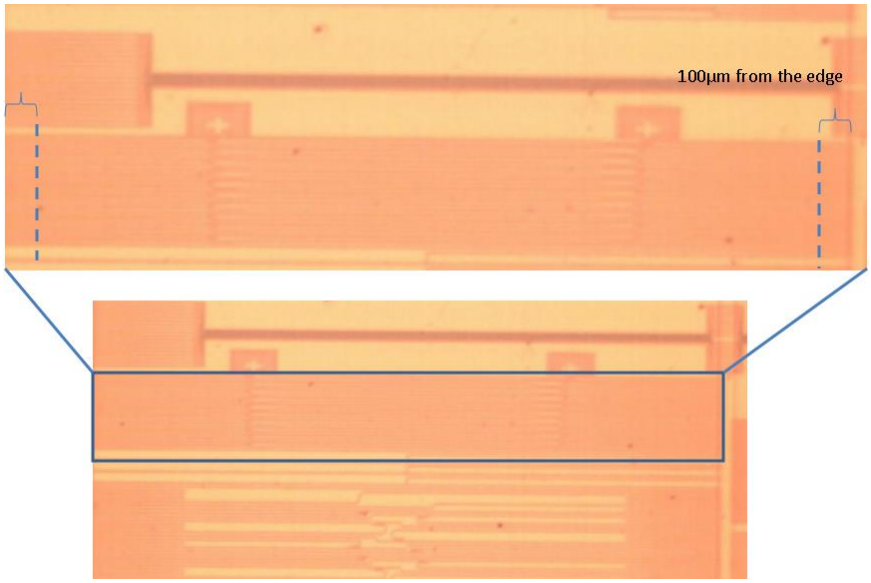

Figure 26: Enlarged view of microscope image of section 1 (designs 1-20, Table 9) of PhC chip showing the dicing lines for laser assisted cleaving.

The laser assisted cleaving was successful and in-plane coupling of broadband light (1440-1630 nm) into the photonic crystal waveguide at the home laboratory was finally achieved. Once again the results were surprising: there was no output. All attempts to detect an output failed. It seemed that no light was propagating through the photonic crystal and the waveguides. The experiments were attempted enough times to conclude that this was the case and that something is physically wrong with the photonic crystals sensors. Visual examination with precision microscopes failed to reveal any physical defects (e.g. a broken waveguide, poor facet…etc). Figures 27 to 33 show a series of microscope images of some of the fabricated photonic crystal structures.

Figure 27: Microscope view of two SOI PhC structures from Table 10. Top structure is a waveguide and bottom structure is a gas sensor.

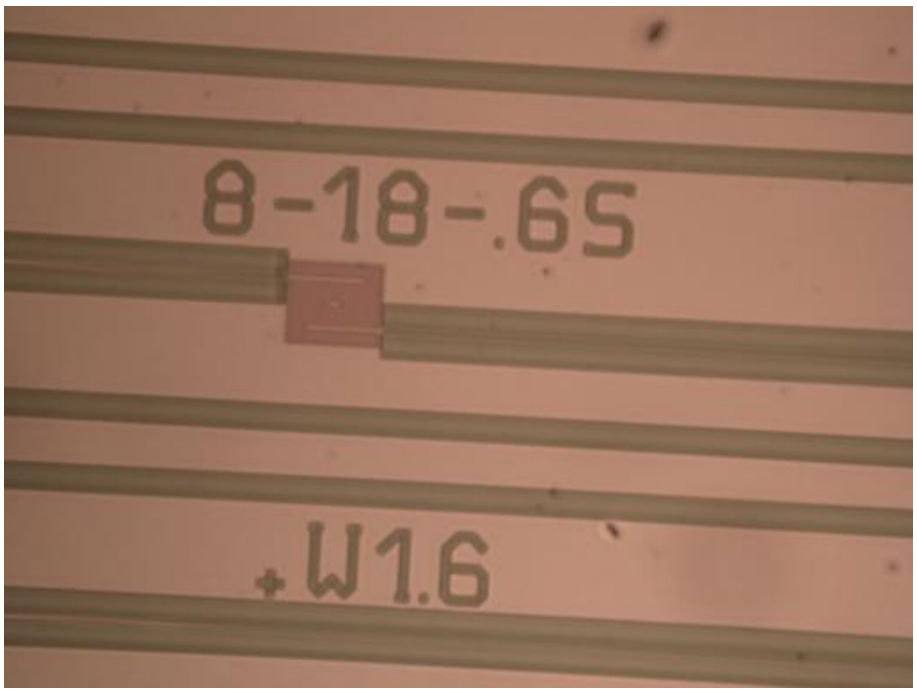

Figure 28: Microscope view of two SOI PhC structures from Table 10. Top structure is a gas sensor and bottom structure is a waveguide.

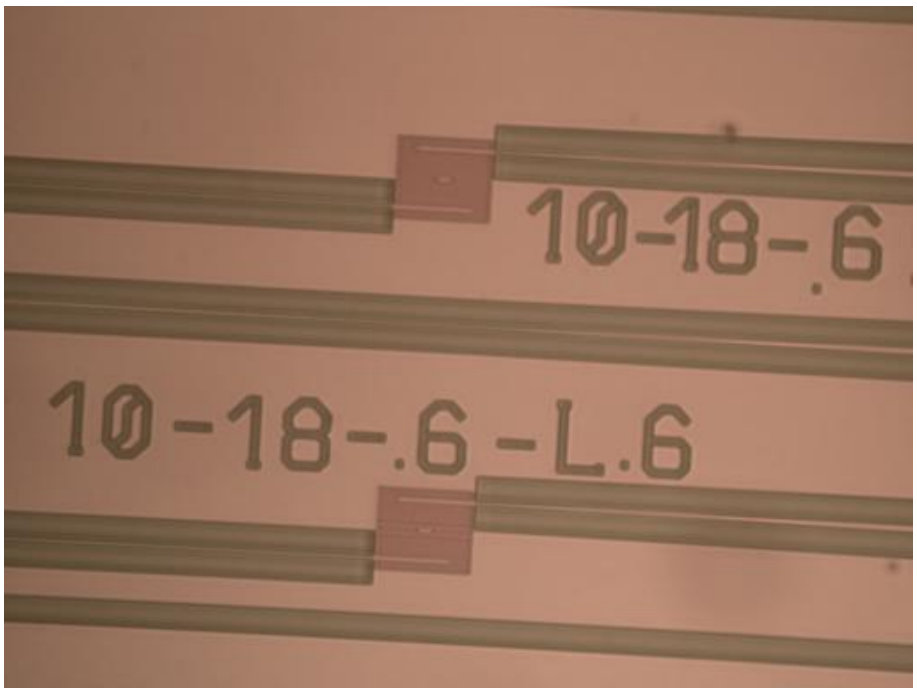

Figure 29: Microscope view of two SOI PhC structures from Table 9 (top) and Table 10 (bottom).

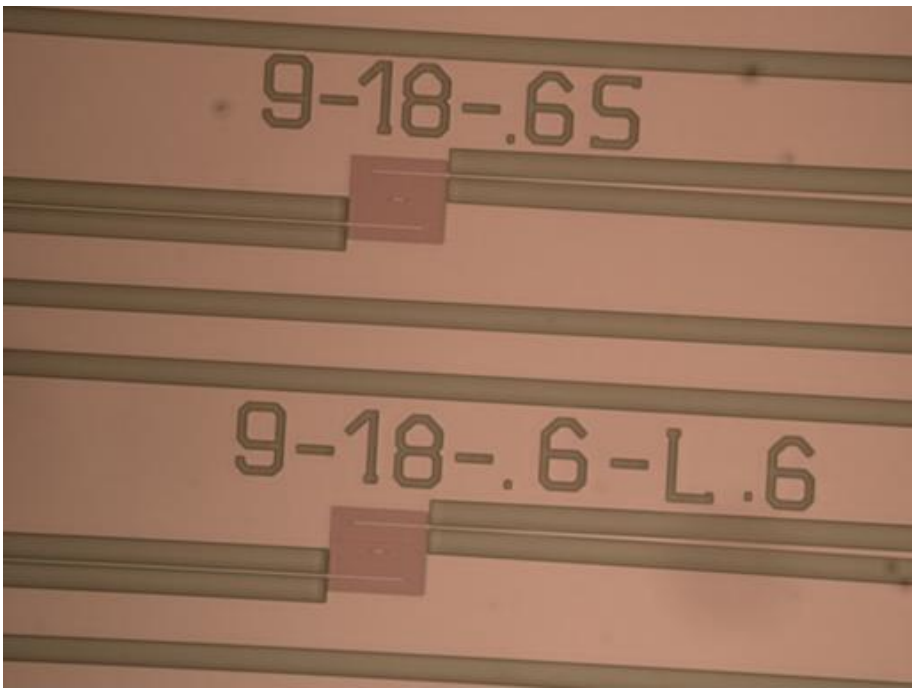

Figure 30: Microscope view of two SOI PhC structures from Table 10.

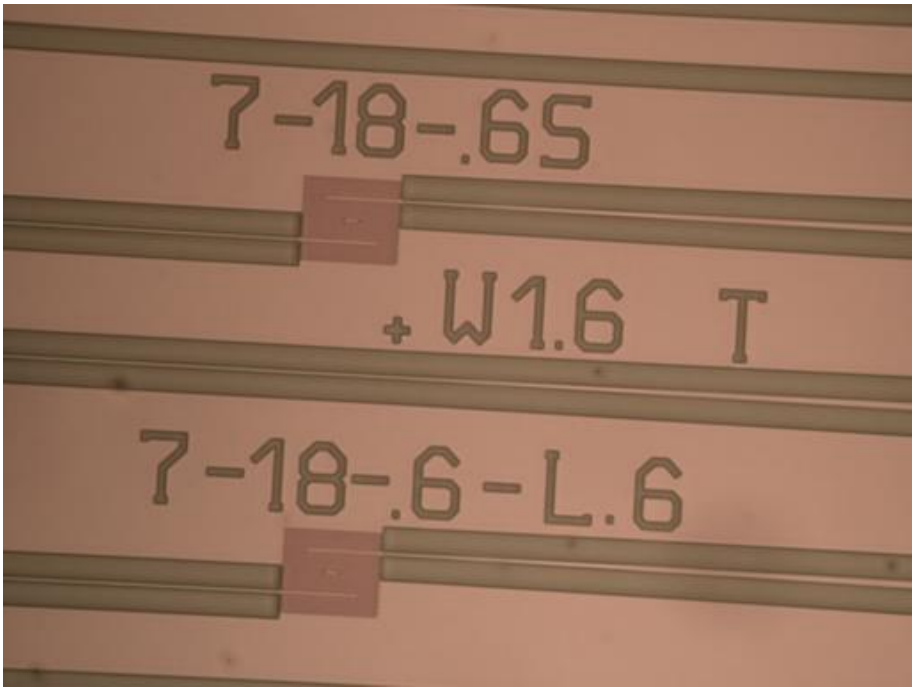

Figure 31: Microscope view of two SOI PhC structures from Table 10.

Figure 32: Microscope view of two SOI PhC structures from Table 10.

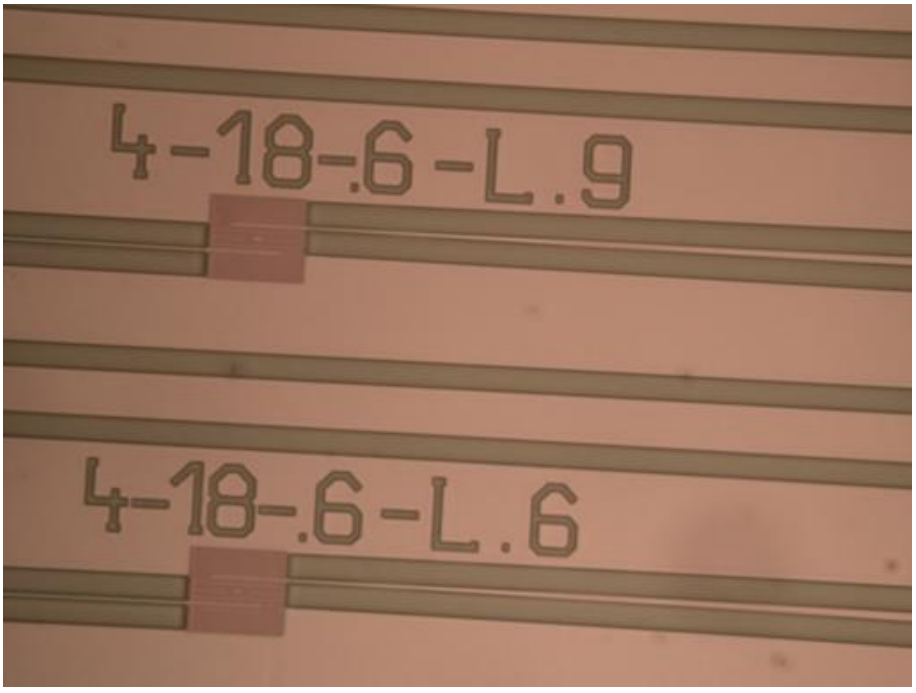

Figure 33: Microscope view of two SOI PhC structures from Table 9.

Finally, a SEM scan at National Research Council Canada, NRC (www.nrc-cnrc.ca) was performed to investigate the physical structure of the photonic crystal in order to determine if there were any fabrication errors. Figures 34 to 42 show a series of SEM scans of the photonic crystal chips.

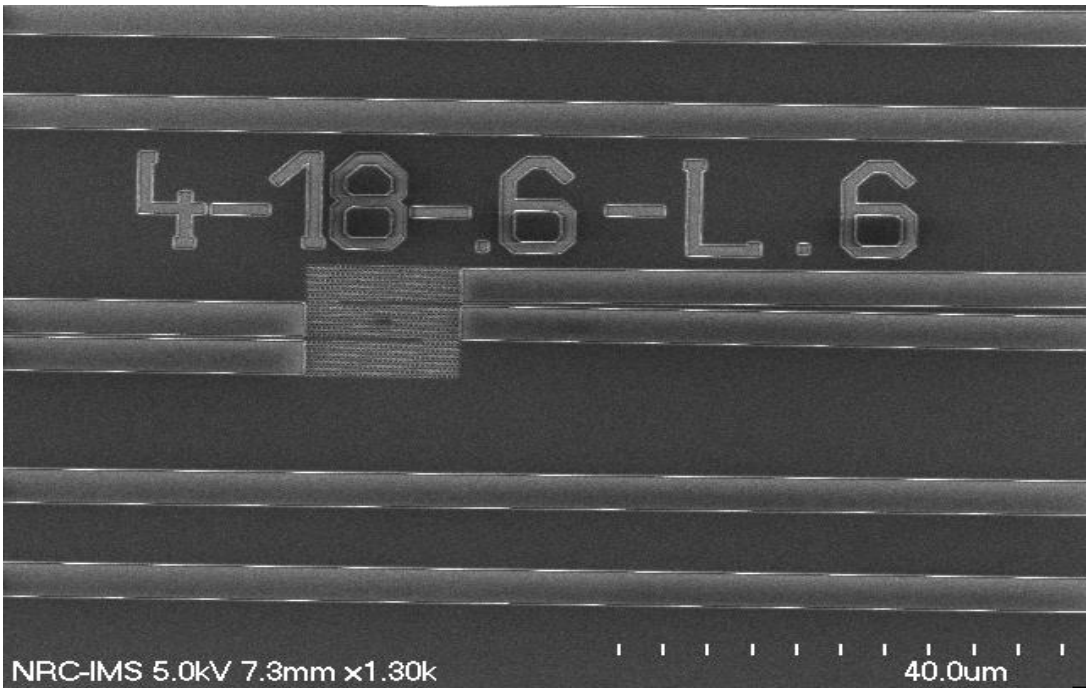

Figure 34: SEM image of SOI PhC gas sensor structure from Table 10 showing input/output tapered waveguides.

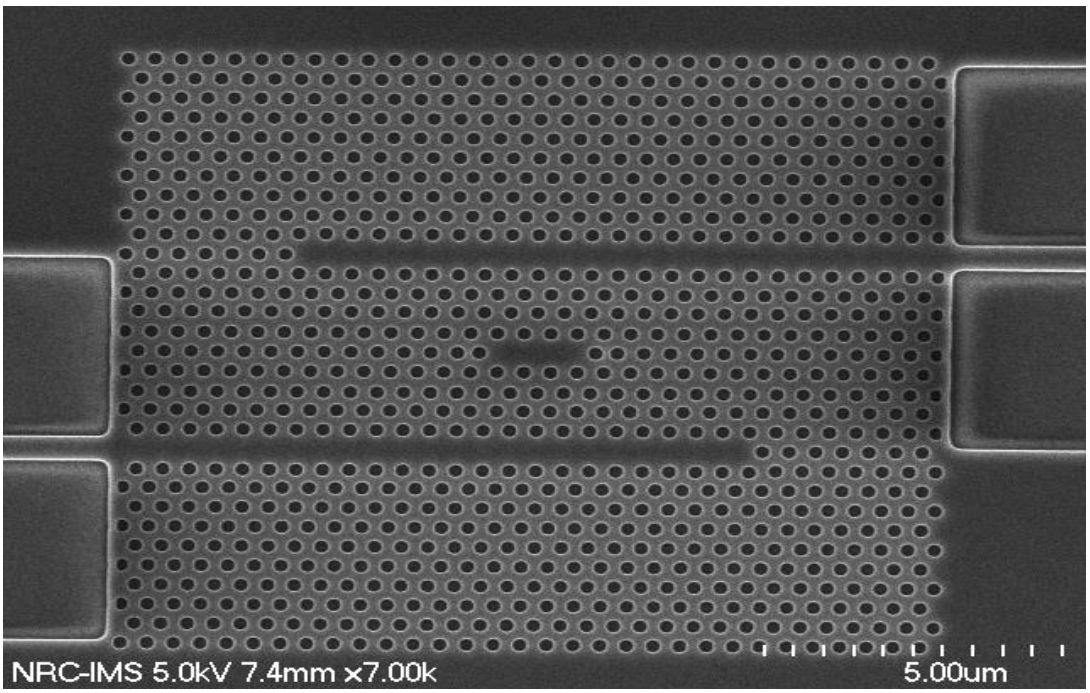

Figure 35: Enlarged SEM image of a SOI PhC gas sensor showing excellent Air hole size uniformity periodicity.

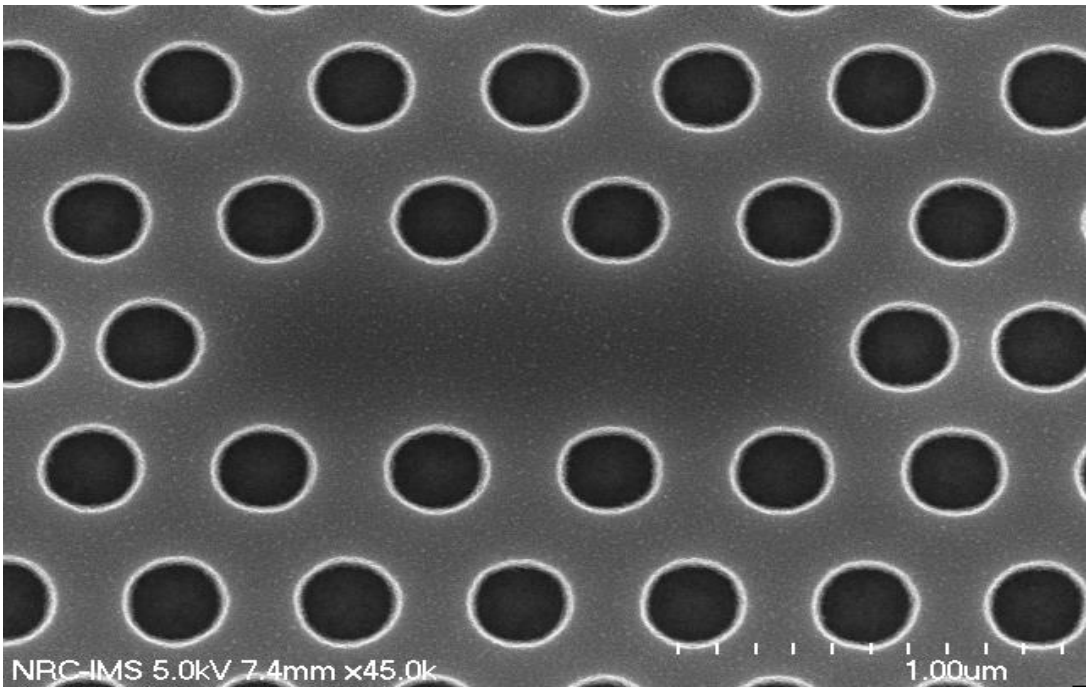

Figure 36: Enlarged SEM image showing L3 cavity of a SOI PhC gas sensor.

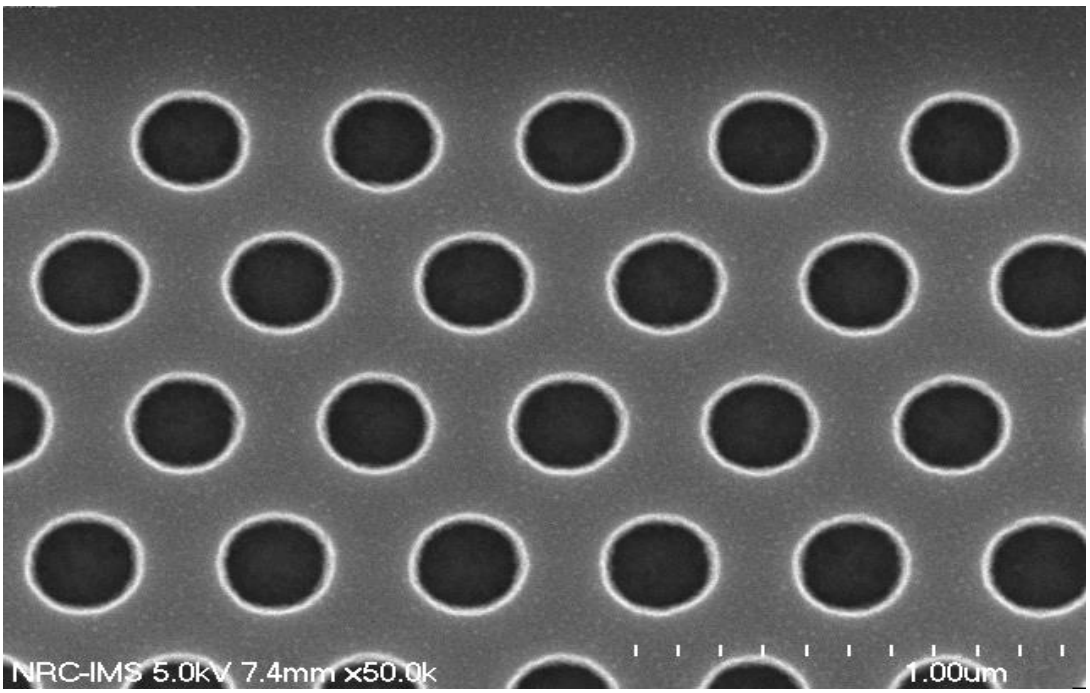

Figure 37: Enlarged SEM image of a SOI PhC structure showing excellent Air hole uniformity and periodicity.

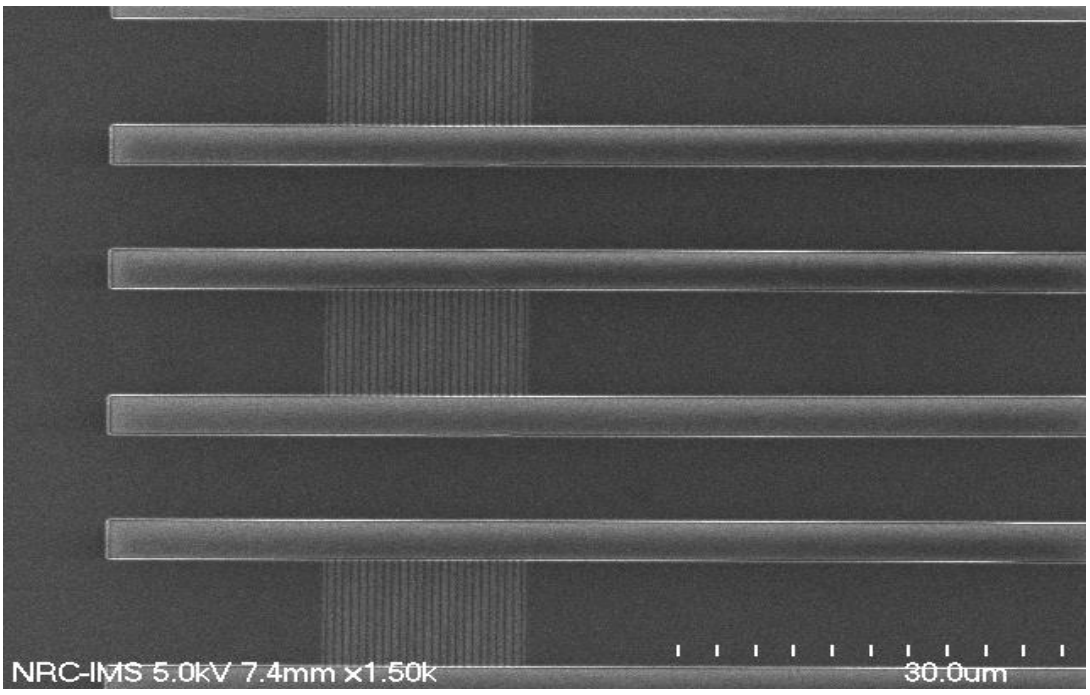

Figure 38: SEM image of vertical grating couplers. They were removed by laser assisted cleaving due to bandwidth issues.

It turns out that the SiO_2 under the photonic crystal was never removed by etching. This meant that there is no Air bridge and as a result, the photonic crystal is not symmetric but asymmetric: it has an Air/Si/SiO_2 interface instead of the symmetric Air/Si/Air interface that designed and simulated in sections 3.4.5 and 3.4.6. This further meant that all previous simulations discussed in section 3.4.6 are no longer applicable to this structure. The situation was surprising as the necessity of the etching step to remove the SiO_2 and create the Air bridge was repeatedly documented. Without the Air bridge, the photonic chip will not function and the experimental tests proved it. Furthermore, there was nothing that could be done to remedy the situation, the Air bridge had to be created during the fabrication process and that step was unfortunately missed by those concerned with fabrication.

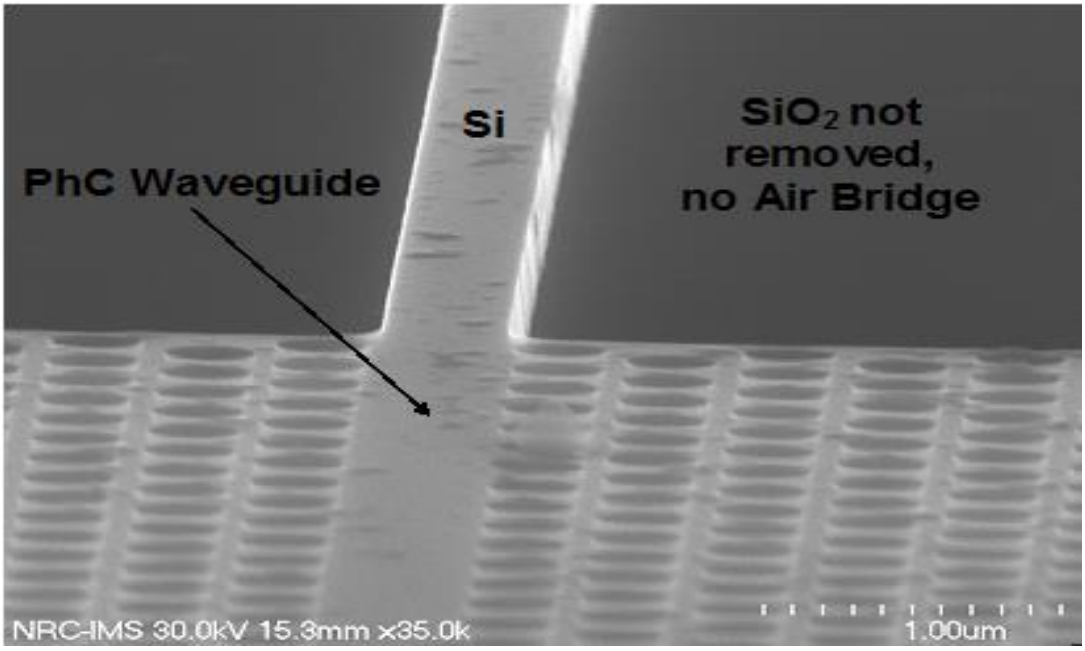

Figure 39: SEM image of SOI PhC (fabricated by IMEC) showing that the Air Bridge was not released (i.e. no Air bridge).

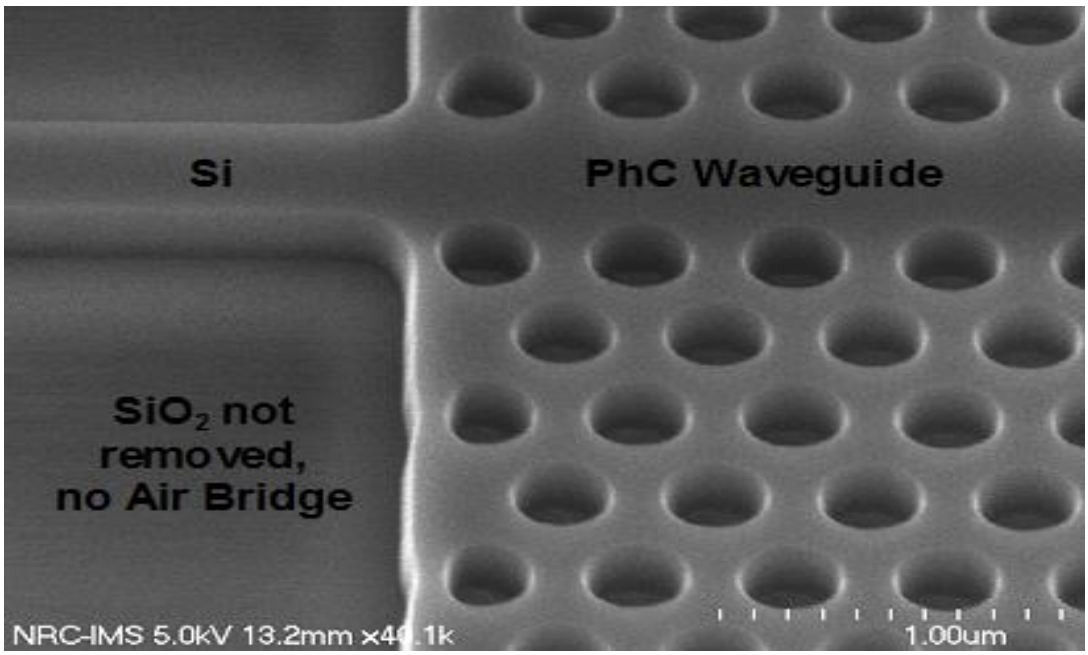

Figure 40: SEM image of SOI PhC (fabricated by IMEC) showing that SiO2 under the PhC was not removed which means there is no Air bridge.

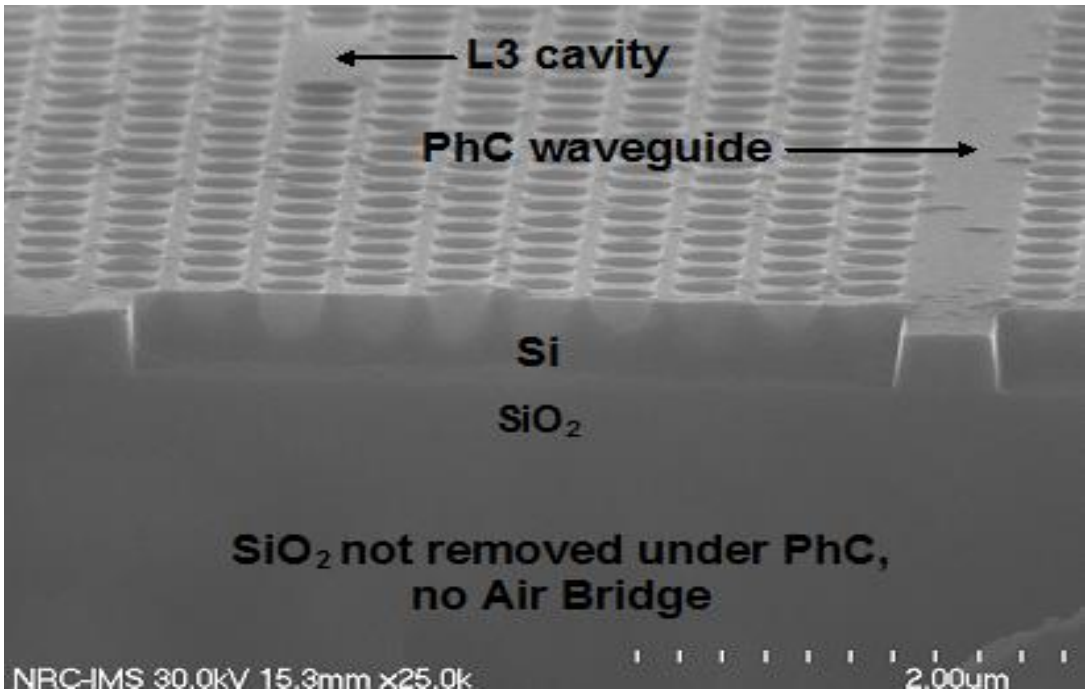

Figure 41: SEM image of SOI PhC (fabricated by IMEC) showing details of the PhC and the absence of the Air Bridge.

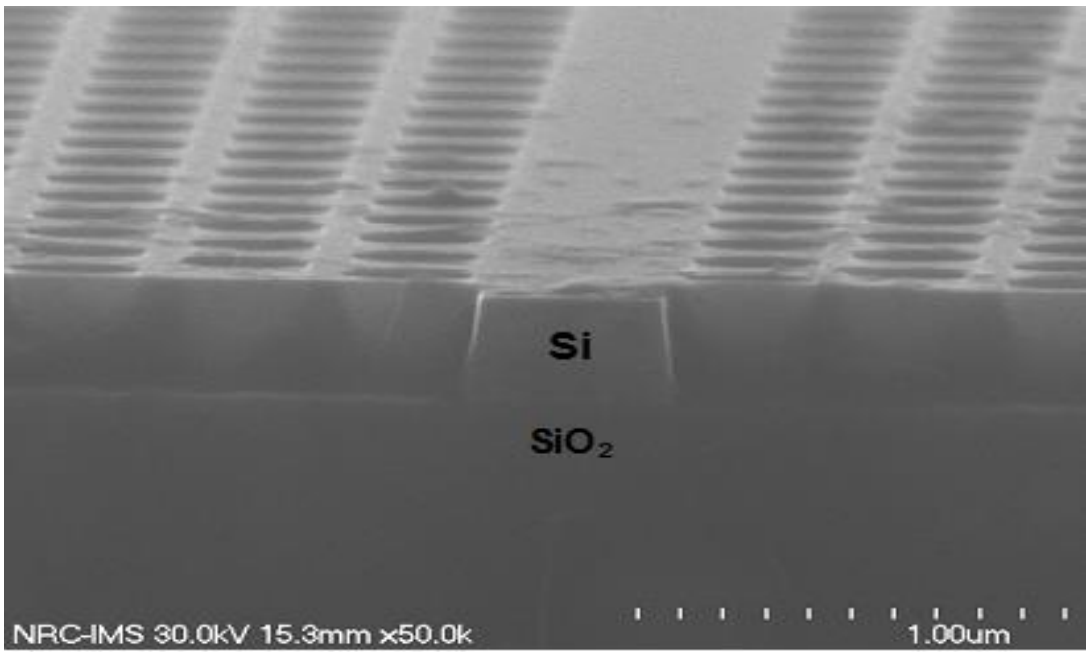

Figure 42: Enlarged SEM image of SOI PhC showing the presence of SIO_2 under the Si PhC (i.e. no Air bridge).

New photonic bandgap simulations of the fabricated asymmetric structure using CrystalWave were performed to determine the photonic bandgap of the real, fabricated structure. From Figures 43 and 44, it can be clearly seen that the photonic bandgap for the fabricated SOI structure is radically different from the photonic bandgap of the designed SOI structure (section 3.4.5, Figure 10, and Table 4). The asymmetry of the Air/Si/SiO_2 interface causes the structure to have no TM photonic bandgap and a very small TE photonic bandgap that only covers the 0.7032 to 0.7924 μm wavelength range. This makes the fabricated structures completely useless, especially given the fact that no good sources and testing equipment and fibres widely exist in this wavelength range. Table 11 gives the photonic bandgap values for the fabricated SOI photonic crystal structures.

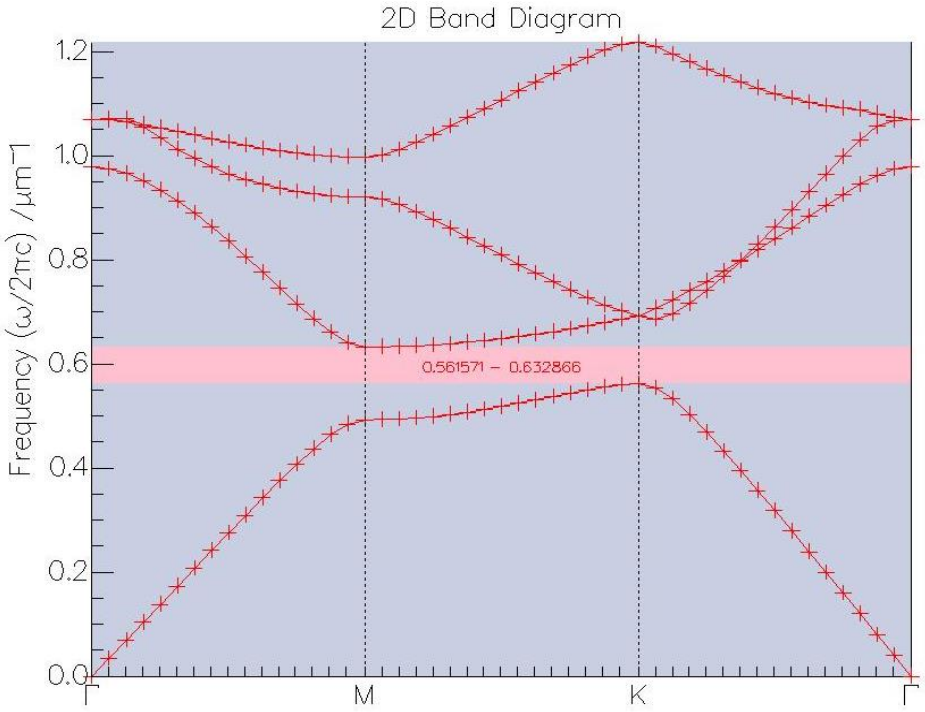

Figure 43: TE Bandgap of SOI PhC with No Air bridge and: a = 445 nm, r = 133 nm.

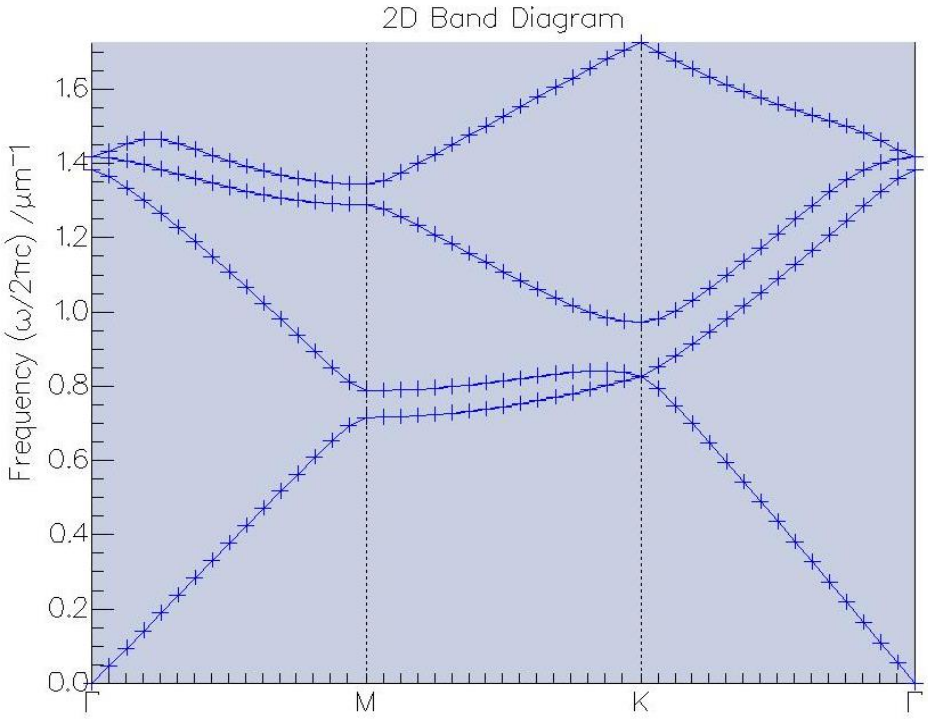

Figure 44: Bandgap of SOI PhC with No Air bridge and: a = 445 nm, r = 133 nm showing no TM photonic bandgap.

Table 11: Photonic bandgap of fabricated SOI PhC with no Air bridge, a = 445 nm, r = 133 nm.

Photonic bandgap	Normalized Frequency range	Wavelength range (μm)
TE	0.561571 to 0.632866	0.7032 to 0.7924
TM	No Bandgap exists	Not Applicable

In conclusion, the fabrication of SOI photonic crystal structures via UBC/CMC and IMEC unfortunately failed due to the aforementioned fabrication errors that occurred and in spite of documented (by both sides) communication of all the necessary simulation results, device parameters, and fabrication steps by the researcher and technical advisors involved. Furthermore, it left this research work at a near impasse as there were no other options for a rerun of the fabrication by IMEC in the near future.

Fortunately, a working relationship with the National Research Council Canada, NRC (www.nrc-cnrc.ca) had been developed at the start of this research work as they had a local fabrication centre and had published prominent research in photonic crystals. They were willing to help in fabricating a new photonic crystal with an Air bridge structure that could serve as a replacement. However, at the time, they have not yet developed a fabrication process for SOI and did not have any plans for such a development in the near future. They did however, have a well developed Indium Phosphide (InP) fabrication process and offered to fabricate the photonic crystal in InP. This was the only available option and it was pursed.

3.5 InP Multi-Gas Photonic Crystal Sensor (MG-PhC)

3.5.1 Background

Using InP as the fabrication material meant that all previous designs, simulations, and mask design for the SOI gas sensor were no longer applicable and must be repeated for InP. Furthermore, there was an initial concern that the gas sensors will not function as effectively in InP as they did (in simulation) in SOI due to the lower refractive index contrast provided by InP (with respect to Air) compared to SOI.

3.5.2 Initial Design

The device structure is very similar to the SOI gas sensor as shown in Figure 11. It is a 2D photonic crystal that uses index guiding in the vertical direction and bandgap guiding in the planar direction. Figure 45 shows a schematic side view of the InP photonic crystal and Figure 46 shows the side view of the device as simulated in CrystalWave.

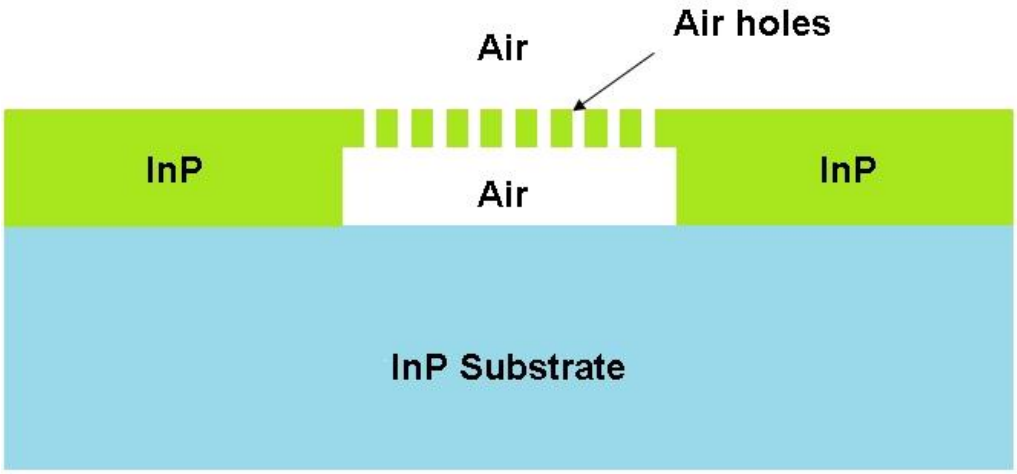

Figure 45: Side view schematic of InP MG-PhC gas sensor showing the Air bridge.

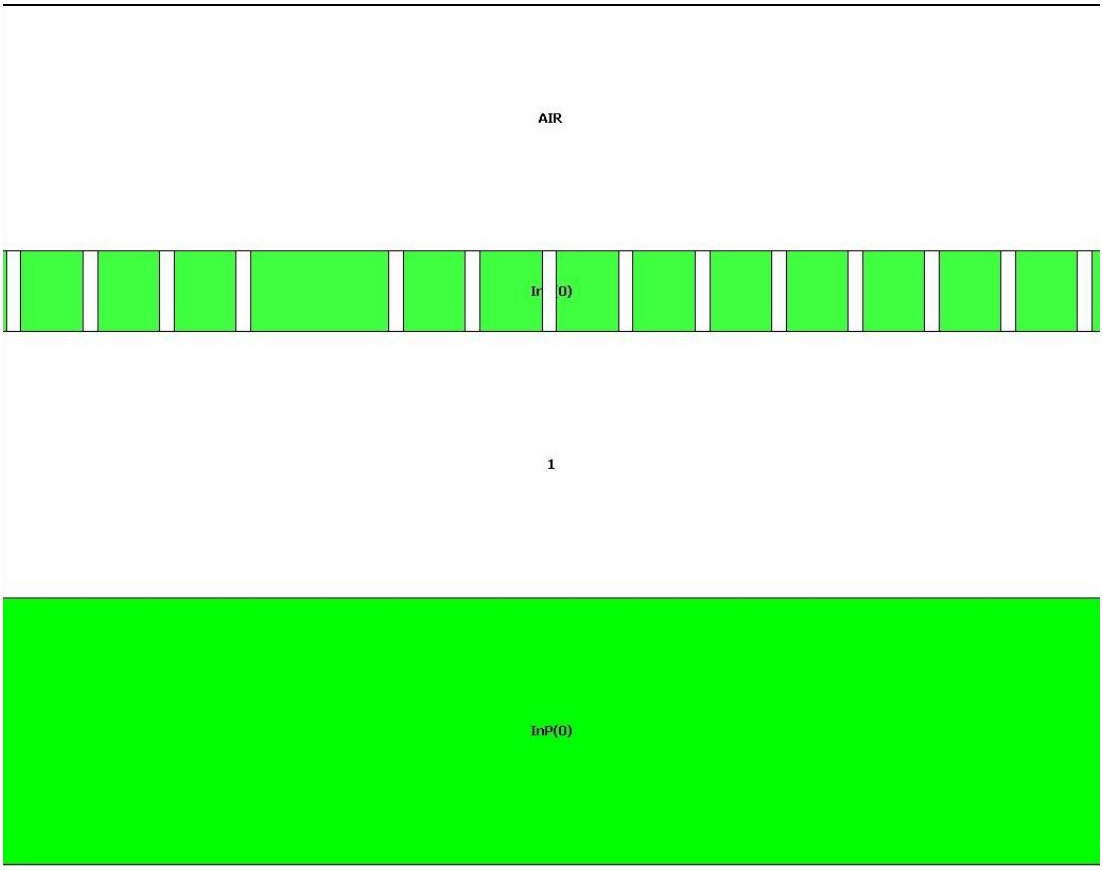

Figure 46: Side view of InP PhC in CrystalWave showing the Air bridge.

The design process discussed in section 3.4.5 was not used to calculate the initial parameters for the InP photonic crystal. InP is not as common a material for photonic crystal fabrication as SOI and there were not many graphs as those in Figure 5 that could aid in calculating the initial design parameters. Instead, a review of published papers discussing InP photonic crystals was carried out and the initial parameters for the photonic crystal design was estimated from the review [Kotlyar et al. 2004; Halloua et al. 2009]. These initial parameters are shown in Table 12.

Table 12: Initial parameters for the InP PhC.

PhC Parameter	Value
Structure	Air Bridge
Lattice constant, a	441 nm
Filling Ratio, $\frac{r}{a}$	1. 0.24 2. 0.25 3. 0.26
Slab thickness, t	300 nm
Substrate thickness	1000 nm

One of the lessons from the experimental testing of the SOI gas sensors was the importance of designing the L3 cavity resonance to be in the C-band, i.e. between 1530-1565 nm. The SOI photonic crystals had a resonance of approximately 1616 nm, i.e. in the L-band. That made it particularly difficult to find sources and couplers suited for that wavelength range which is not as commonly utilized as the C-band. Designing for a resonance in the C-band makes more sense for experimental investigation due to the abundance of testing equipment in that range which happens to be the most used wavelength range in telecommunication applications.

One of the ways to tune the resonance of the L3 cavity is to vary the Air hole radius. Several 3D FDTD simulations with varying Air hole radii (as shown in Table 12) were carried out to design a L3 cavity with a resonance in the C-band.

Figure 47 shows the photonic bandgap for a = 441 nm and $\frac{r}{a}$ = 0.25 and Table 13 summarizes all key findings of this simulation exercise. As can be observed, the parameters in Table 12 do not allow a photonic crystal with a cavity resonance in the C-band. All the simulated resonances were in the L-band which would make testing this structure quite challenging. Thus, different parameters were needed.

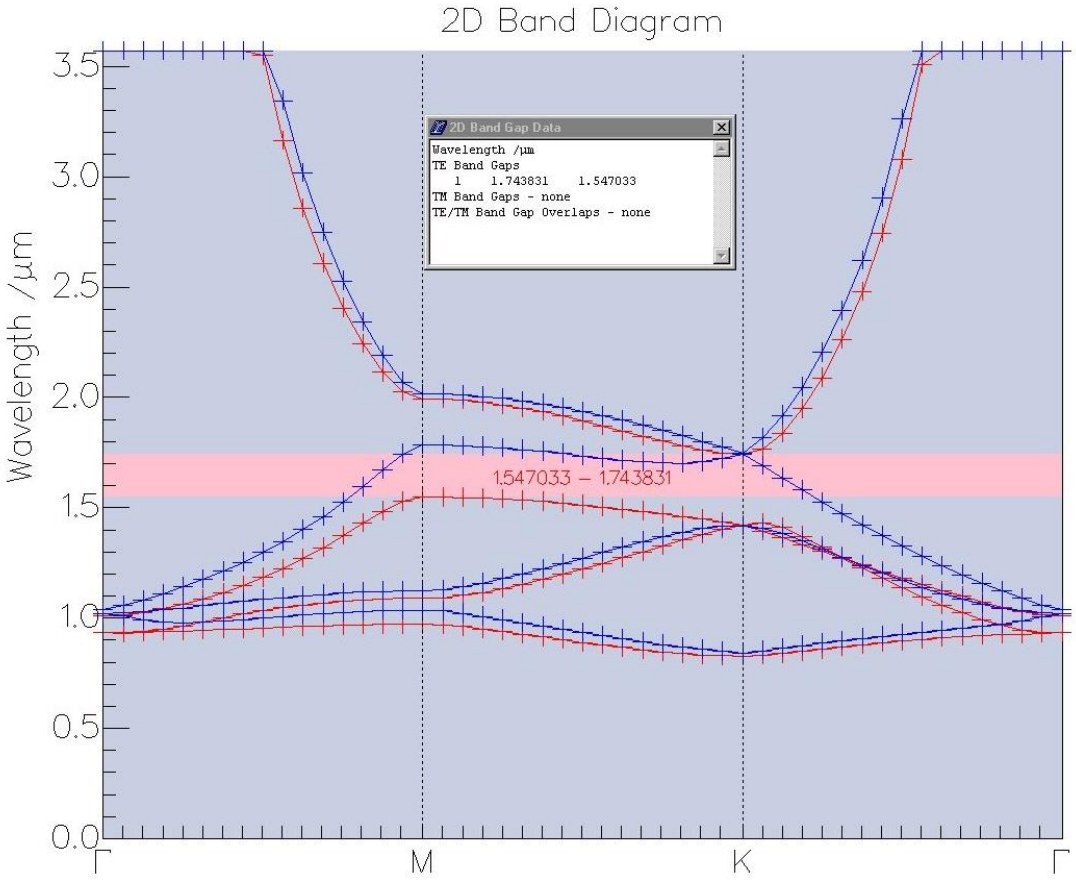

Figure 47: Bandgap of InP PhC with parameters a = 441 nm, r = 0.25a.

Table 13: Key findings of FDTD simulations for InP PhC with a = 441 nm.

Ratio	Photonic Bandgap	Resonance	Linewidth	Q-factor
$\frac{r}{a}$ = 0.24	1.58 – 1.75 nm	1653.8 nm	0.783 nm	2111.3
$\frac{r}{a}$ = 0.25	1.55 – 1.74 nm	1653.8 nm	0.783 nm	2111.3
$\frac{r}{a}$ = 0.26	1.51 – 1.73 nm	1630.4 nm	0.653 nm	2494.8

The lattice constant, a, has a significant effect on the resonance of the photonic crystal cavity and so a new value is needed to shift the resonance to the C-band. Furthermore, a NRC communication stated that the slab thickness, t, should be set to 285 nm instead of 300 nm. This was due to their fabrication process. After further literature research, the following new parameters were chosen: a = 465 nm, and $\frac{r}{a}$ = 0.36a. Figure 48 shows a top view of the InP photonic crystal gas sensor structure with these parameters as simulated in CrystalWave.

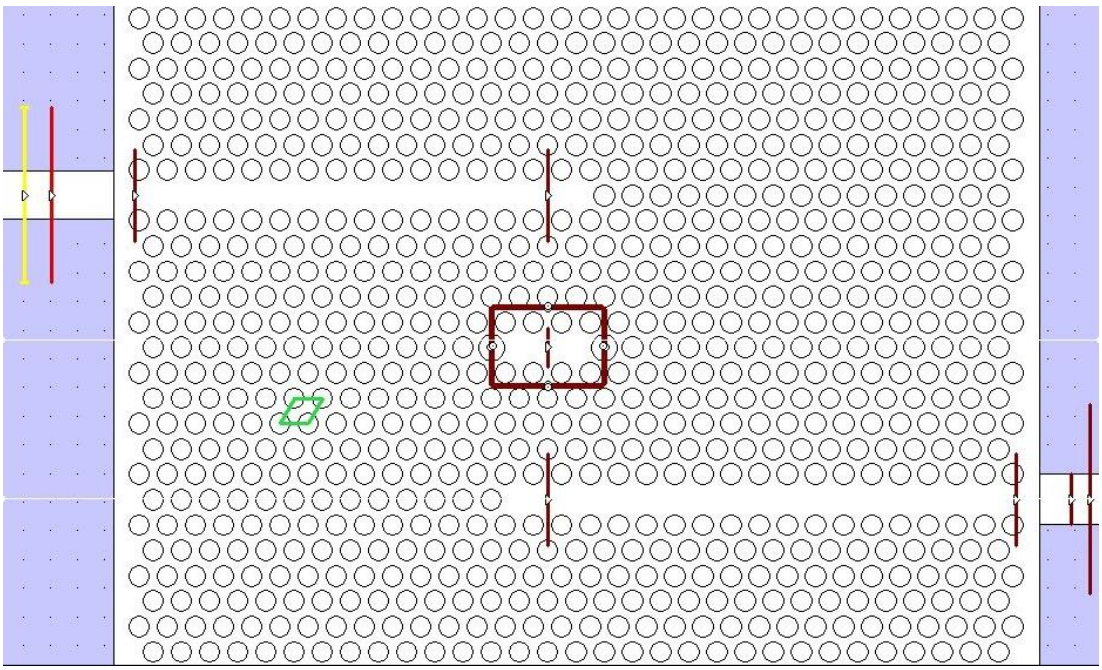

Figure 48: Top view of InP PhC gas sensor as simulated in CrystalWave, a = 465 nm, r = 0.36a.

Figure 49 shows the simulated photonic bandgap for the photonic crystal gas sensor with a = 465 nm and r = 0.36a. Clearly, there is a large TE gap that covers the C-band and therefore these parameters can be used to build a gas sensor with the desired properties. Table 14 summarizes the bandgaps for these parameters.

Table 14: Photonic bandgap for InP PhC with a = 465 nm, r = 0.36a.

Photonic Bandgap	Wavelength range (μm)
TE	1.1979 – 1.6477
TM 1	1.6647 – 1.6669
TM 2	0.9793 – 0.9805

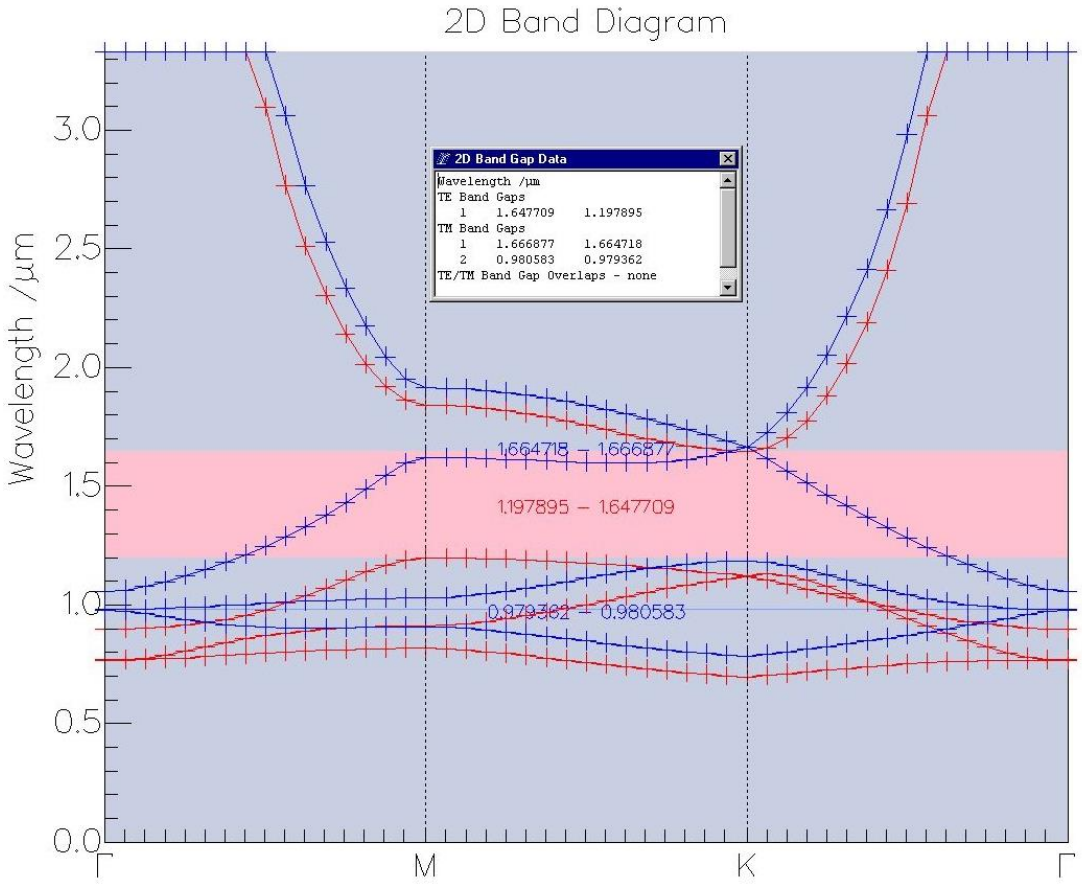

Figure 49: Bandgap of InP PhC with parameters a = 465 nm, r = 0.36a.

3D FDTD simulation were performed to determine the resonance of the L3 cavity. The simulation was run for 8000 fs (more powerful computers became available) with a grid size of $\frac{a}{16}$ and the surrounding gas was set to Air (refractive index, n = 1). The dominant simulated resonance was 1559.5 nm with a linewidth of 0.49 nm and Q-factor of 3181. Thus, the new photonic crystal parameters allowed the design of a L3 cavity with a resonance in the C-band which would make the experimental testing straightforward. The final photonic crystal parameters are summarized in Table 15.

Table 15: Final parameters for the InP PhC.

PhC Parameter	Value
Structure	Air Bridge
Lattice constant, a	465 nm
Filling Ratio, $\frac{r}{a}$	0.36
Slap thickness, t	285 nm
Substrate thickness	1000 nm

3D FDTD simulations with two different gases were performed to investigate the performance of the gas sensor. The two gases were: 1. Helium (n = 1.000035), and 2. Argon (n = 1.000281). The results however, were not promising: the simulated wavelength shift in the gas sensor was very small: 0.1 nm for Helium and no shift for Argon. This is much smaller than the shift for the SOI photonic crystal gas sensor, which was over 2 nm (Table 6). Furthermore, this low value was within the margin of error of the FDTD simulations in CrystalWave. This meant that there was no guarantee that a wavelength shift actually took place and thus the simulations do not really prove that the sensor can sense different gases.

These result were however, somewhat expected because it was kown from the start that InP has a lower refractive index than SOI. Thus, InP photonic crystals have a much lower refractive index contrast with respect to Air than SOI photonic crystals. This means that InP photonic crystals have much weaker index guiding capabilities and therefore the optical fields are not as strongly confined (in the vertical direction)

in an InP photonic crystal as they would be in a SOI photonic crystal. Since the performance of the gas sensor depends on how strongly the optical field is confined in the L3 cavity, an InP gas sensor is no where near as sensitive as a SOI gas sensor as has been confirmed by the initial simulations.

The inability to produce high quality, high aspect ratio InP photonic crystals is well documented in literature and has limited the experimental investigation of InP photonic crystals to only a handful of attempts [Kotlyar et al. 2004]. It is important to note that InP photonic crystal do work but often have poor optical properties. However, InP photonic crystals have found wide application in the creation of active photonic crystals, i.e. photonic crystals with active components (e.g. a laser or LED). This is often accomplished with a hybrid fabrication approach: InP on SOI. InP is a direct bandgap material and therefore, well suited for fabrication of active components unlike silicon (an indirect bandgap material). The SOI layer provides the sufficient refractive index contrast (high aspect ratio) to ensure strong index guiding in the vertical direction [Halloua et al. 2009].

Unfortunately, the NRC could not fabricate such hybrid photonic crystals and thus the only option available was to attempt to optimize the L3 cavity in the hopes of increasing the confinement of the optical field by increasing the L3 cavity Q-factor. A series of 3D FDTD simulations were carried out to investigate different ways to accomplish this. Table 16 summarizes the results of these investigations.

Table 16: Results of FDTD simulations for different InP PhC gas sensor structures.

$$\text{Grid size} = \frac{a}{16}.$$

PhC structure	Gas	Duration (fs)	Resonance Nm	LineWidth (nm)	Q-factor
1. a = 465 nm, r = 0.36a					
	Air	8,000	1559.5	0.49	3181
	He	8,000	1559.4	0.51	3059
	Ar	8,000	1559.5	0.49	3186
2. a = 465 nm, r = 0.36a. L3 Air hole Radius = 0.36a+0.2a					
	Air	4,000	1576.6	0.6	2614
	Air	6,000	1575.7	1.23	1238
	He	6,000	1575.6	0.98	1606
	Ar	6,000	1575.7	1.12	1556
	Air	8,000	1575.8	1.15	1367
	He	8,000	1575.9	0.97	1633
	Ar	8,000	1575.8	1.3	1200
	Air	16,000	1577.4	0.57	2737
	He	16,000	1577.2	0.64	2473
	Ar	16,000	1557.4	0.62	2565
	Air	24,000	1577.3	0.63	2509
	Ar	24,000	1577.3	0.63	2509

Different L3 cavity configurations were attempted, ranging from shifting the Air holes that define the L3 cavity outwards to increasing/decreasing the size the L3 cavity Air holes, which is another popular approach in literature for increasing the Q-factor of photonic crystal cavities.

Unfortunately, as can be seen from Table 16, none of these attempts have bore much fruit. It was not possible to increase the Q-factor for the L3 cavity in any of the simulated configurations past 3200, a low value, and much smaller than the 33,000 value which was common in the simulations with the SOI cavity (Table 7). Furthermore, the wavelength shift due to a change in the surrounding gas was never greater than 0.2 nm in any of the simulations. As discussed previously, this value is very low and within the margin of error of the FDTD simulations in CrystalWave, i.e. it could very well be the case that no shift actually happens at all and thus the sensor does not work.

Therefore, it safe to conclude that the proposed (localized cavity) photonic crystal gas sensor does ***not*** work if it is fabricated in InP and the initial suspicions about InP as a poor choice for this type of sensor proved correct. The sensor does work effectively however if it is fabricated in SOI as the simulations in section 3.4.6 proved. Therefore, a rethinking of the approach gas sensing in photonic crystals using InP (the only available fabrication platform) was needed to successfully complete the research and fortunately, the breakthrough finally came.

As discussed in section 3.3, there are several approaches to gas sensing in photonic crystals. Some of the most common approaches include: 1. refractive index resonant cavities, and 2. enhanced light-matter interactions. All research efforts up to this point focused on the resonant cavities approach, which is ineffective in low contrast material such as InP.

However, it was believed that the second approach, the enhanced light-matter interactions, may hold the key to solving the gas sensing in low contrast material dilemma. By its very nature, such an approach allows for greater interaction between the optical fields and matter and that could possibly overcome the low contrast nature of InP photonic crystals and allow for the creation of viable photonic crystal gas sensors.

Thus, the research effort evolved to consider using the slow light phenomenon in InP photonic crystals to sense gases. Such sensors will have a significant advantage over SOI based sensors as the integration of the broadband laser source (which is often made in GaAs or InP) will be far easier and more cost effective in InP sensors compared to SOI sensors. This is discussed and proven in subsequent sections of this chapter.

3.6 Slow light InP Multi-gas Photonic Crystal Sensor

3.6.1 Background

In this section, a gas sensor based on photonic crystals in InP waveguides where the gas sensing is based on the interaction between the slow light mode and the gas is introduced. At the time of writing the Thesis and to the best of our knowledge, such an approach and its experimental validation have never been reported to date. This section forms the bulk of the original contributions arising out of this research work [Awad et al. 2011].

When the refractive index of the photonic crystal waveguide changes due to a change in gas species, the slow light regime in the waveguide is affected and shifts in wavelength. Furthermore, since the slow light mode interacts strongly with the photonic crystal, it may be possible to build a more sensitive gas sensor using this approach than a gas sensor that relies on a localized resonant cavity in a photonic crystal and uses the fast mode, given the same fabrication material.

There have been very recent experimental demonstrations of enhanced light-matter interactions e.g. slow light to sense gases in photonic crystals. These approaches take advantage of the low group velocities of the slow light mode in photonic crystals to effectively increase the interaction length of the gas with the optical field [Jensen et al. 2008; Pergande et al. 2011]. These approaches can be classified as amplitude-based gas sensors: the sensing of a gas is determined by observing the amplitude change (from the reference conditions due to the reference gas, Air) in the transmission spectrum of the gas sensor due to the presence of the gas in the photonic crystal waveguide [Pergande et al. 2011].

By contrast, the proposed sensor is wavelength-based: the presence of the gas is determined by the wavelength shift of the slow light mode from the reference slow light mode in the photonic crystal i.e. the slow light mode that exists when the photonic crystal sensor is filled with the reference gas. Such an approach is potentially more robust from a practical perspective since a wavelength shift is often easier to detect than an amplitude shift.

3.6.2 Introduction to Slow Light in Photonic Crystals

Slow light with group velocity several tens to several hundreds lower than c, the speed of light in vacuum, ~ 3 x 10^8 m/s, has been demonstrated and extensively studied over the past decade with numerous theoretical and experimental demonstrations in a spectrum of published materials [Figotin and Vitebskiy 2006; Krauss 2007; Baba 2008]. There exists a variety of approaches to creating slow light but the focus here only concern slow light in photonic crystals for the purposes of this research work. Numerous applications of slow light exist including gas sensing, the design of tunable optical delay lines, efficient optical amplifiers and lasers, and quantum communication [Figotin and Vitebskiy 2006; Krauss 2007; Baba 2008].

Photonic crystals make excellent devices for exploiting the slow light phenomenon; the performance of dielectric slow light devices scales as the refractive index contrast [Krauss 2007]. Thus, potentially the gas sensor should provide superior performance in the SOI photonic crystals (which provide higher refractive index contrast) than InP photonic crystals. Nevertheless, an experimental demonstration of an effective gas sensors using InP photonic crystals utilizing the slow light mode was achieved, not possible with localized resonant cavities.

Slow light adds great functionality to a material by structuring alone. For example, it allows the enhancement of typically weak interactions in materials of interest including widely used dielectrics such as silicon and III-V materials e.g. GaAs and InP [Krauss 2007; Baba 2008]. Linear effects such as gain, thermo-optic and

electro-optic interactions scale with the slowdown factor, while nonlinear effects scale with its square [Krauss 2007].

The slow light phenomena in photonic crystals can be described using the standard ray optics approach commonly used to describe light propagation in dielectric waveguides [Krauss 2007]. Photonic crystals however, offer two additional features, not found in typical waveguides that can lead to the formation of slow light modes: 1. backscattering, and 2. omnidirectional reflection (Figure 50).

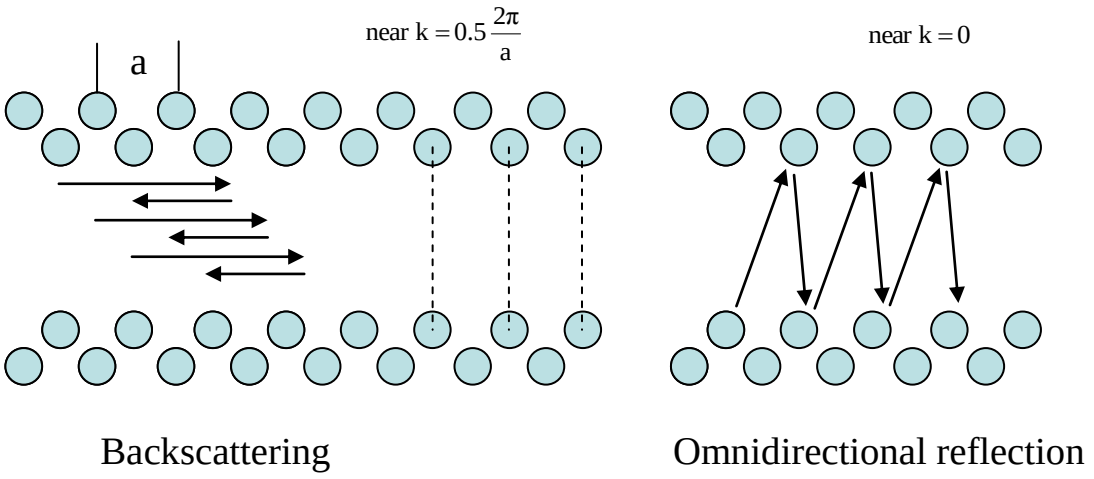

Figure 50: A schematic illustration of the two possible mechanisms for the formation of slow light modes in photonic crystal waveguides [Krauss 2007].

In backscattering, light is coherently backscattered at each unit cell of the photonic crystal, i.e. the photonic crystal acts as a 1D grating as shown by the vertical lines in Figure 50. When the forward propagating and backscattered light match in phase and amplitude, a standing wave results which can be thought of as a slow mode with zero

group velocity. This happens at the Brillouin zone boundary for $k = 0.5\frac{2\pi}{a}$. Moving away from the Brillouin zone boundary enters into the slow light regime; the forward and backward travelling components begin to move out of phase but still interact and this results in a slowly moving interference pattern referred to as the slow mode. Moving even away from the Brillouin zone boundary, the forward and backward travelling waves do not experience much interaction because the phase mismatch is too significant and the mode behaves as a regular waveguide mode dominated by total internal reflection.

The second unique feature of photonic crystal waveguides is that they have no cut-off angle. If the photonic bandgap is present, light propagating at any angle will experience reflection. Even light propagating at or near normal incidence may therefore form a mode as indicated in Figure 50. This corresponds to propagation at or near the Γ-point, i.e. $k \approx 0$. Such modes have very small forward components and thus travel as slow modes along the waveguide and for k = 0, they actually form a standing wave.

These two effects (backscattering and omnidirectional reflection) represent the limiting cases for slow light propagation in photonic crystal waveguides. The bandwidth of the slow light is ultimately limited by the Brillouin zone. For a group velocity of $\frac{c}{n_g}$, with n_g being the group index, then the maximum bandwidth can be determined as [Krauss 2007]:

$$v_g = \frac{d\omega}{dk} = \frac{c}{n_g} \qquad (37)$$

$$\Delta v = \frac{1}{2\pi}\frac{c}{n_g}0.5\frac{2\pi}{a} = \frac{c}{2n_g a} \qquad (38)$$

where:

- ω: the resonance angular frequency,
- k :the wavevector,
- v_g: group velocity,
- n_g: group refractive index,
- Δv: slow light bandwidth.

Through proper design, it is possible to control the different resonances that contribute to the formation of the slow light mode and control its slowdown factor and the bandwidth over which it occurs. Such optimization however, is limited by the size of the Brillouin zone.

The slow down factor, S, is defined as the ratio of the phase velocity to the group velocity [Krauss 2007]:

$$S = \frac{v_\phi}{v_g} \qquad (39)$$

where:

- v_ϕ: the phase velocity,
- v_g: the group velocity.

The slow down factor is an important parameter when discussing slow light in photonic crystals. Linear and nonlinear interactions in photonic crystals scale with the slow down factor [Krauss 2007]. As discussed earlier, refractive index based gas sensing is a linear process and so it will scale with the slowdown factor if the slow mode is utilized for sensing instead of the fast mode. This enhances the sensitivity of the sensor..

In a photonic crystal, a distinction must be made between the material refractive index, n_{mat} and the effective modal index, n_{eff}, illustrated in Figure 51 [Krauss 2007].

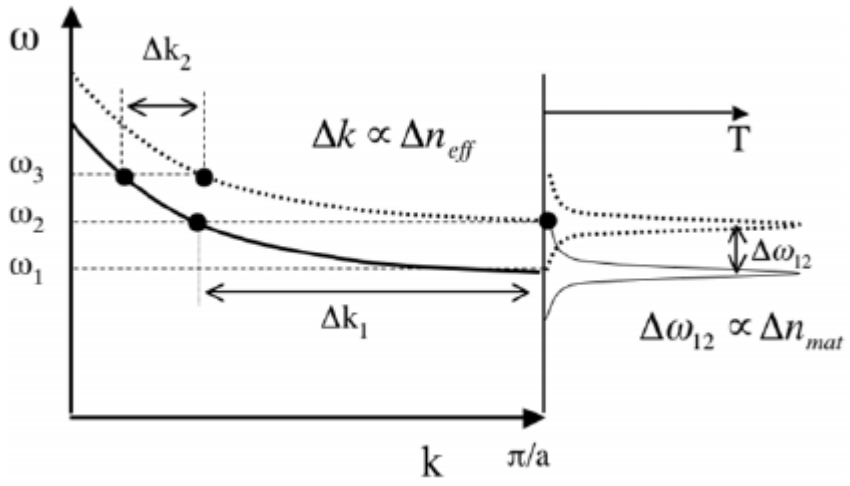

Figure 51: A schematic illustration of the difference between the effect of the material index n_{mat} and the effective modal index n_{eff} in the slow light regime in photonic crystals [Krauss 2007].

In Figure 51, the dispersion curve of a particular mode is described by the solid line. Since a mode represents a resonance condition of the photonic crystal waveguide, it may be depicted as a transmission peak (Figure 51). Now, if the material index is changed due to e.g. presence of a gas, the resonance moves accordingly. Furthermore, the corresponding change in the resonance frequency is proportional to the change in the index as discussed previously in the resonant cavity based refractive index sensors (Section 3.4). This change is indicated by the dotted line in Figure 51 expressed mathematically as [Krauss 2007]:

$$\frac{\Delta\omega}{\omega} \approx \frac{\Delta n}{n} \qquad (40)$$

$$\Delta\omega_{12} \propto \Delta n_{mat} \qquad (41)$$

However, the change in resonance frequency of a guided mode will be different than that described in Equation (41). It is actually given by the change in the effective modal index and can be derived from the wave equation as follows [Krauss 2007]:

$$c = \frac{\omega}{k} \Rightarrow \frac{c_\circ}{n_{eff}} = \frac{\omega}{k} \qquad (42)$$

$$\Delta n_{eff} = \left(\frac{c_\circ}{\omega}\right)\Delta k \qquad (43)$$

In Figure 51, the area where the dispersion curve is flat represents the slow light regime. It is clear then that Δk and consequently Δn_{eff} are much larger than in the

case of the fast light regime where the dispersion curve is steeper, i.e. $\Delta k_1 > \Delta k_2$. Thus, the slow light mode experiences a larger change in effective index than the fast mode, despite the fact that both modes experience the same change in material index, n_{mat} [Krauss 2007]. This allows the slow mode to have greater interactions with matter compared to the fast mode; thus, a cavity based photonic crystal gas sensor utilizing the slow light mode is expected to have better performance than a similar (or identical) sensor that utilizes the fast mode.

Figure 51 and Equation (43) provide a theoretical explanation for the commonly cited assertion in literature that slow light interacts more strongly with matter and thus, allows for the construction of better sensors, compared to fast light sensors [Krauss 2007; Lambrecht et al. 2007; Jensen et al. 2008; Wang et al. 2010; Pergande et al. 2011; Zaho et al. 2012; Zhang et al. 2012].

3.6.3 Sensor Structure and Theory of Operation

The sensor structure is very similar to the localized resonant cavity InP and SOI gas sensors discussed in Section 4.3 and Section 4.4. It is based on a 2D photonic crystal slab (straight) waveguide with a triangular lattice structure with Air holes in the dielectric within an Air bridge configuration. Figure 52 shows a top view schematic of the sensor as it was simulated in CrystalWave and Figure 46 shows a side view of the sensor in CrystalWave illustrating its Air bridge structure. The photonic crystal parameters were identical to the InP gas sensor of Section 4.4: the lattice constant, a = 465 nm, Air hole radius, r = 0.36a, and slap thickness, t = 285 nm (Table 15).

The sensor detects different gases based on their differing refractive indices: the presence of a gas in the photonic crystal waveguide induces a refractive index change from the reference refractive index due to, e.g. Air. This in turn, affects the band structure of the photonic crystal, which is formed by the dielectric, InP, and the surrounding gas. As different gases have different refractive indices, the band structure (and the dispersion relation) of the photonic crystal is different for each gas. This in turn, causes the slow light regime to shift in wavelength thus sensing the presence of the gas.

Such a sensor represents a new class of photonic crystal sensors that combines both the slow light regime phenomena along with the RI sensing capabilities inherent to photonic crystals. This class of sensors is referred to as slow light refractive index sensors. Furthermore, due to the theoretical discussion in Section 3.6.2, a slow light refractive index sensor has the potential to provide better performance than a comparable sensor that utilizes the fast light mode.

Figure 52: Top view of InP PhC waveguide gas sensor as simulated in CrystalWave.

3.6.4 FDTD Simulations

3D FDTD simulations in CrystalWave have been undertaken to characterize the performance of the InP photonic crystal waveguide and its viability as a gas sensor. Figure 53a shows the output of the InP photonic crystal waveguide to broadband pulse input centred at 1.55 μm (shown in Figure 53b) and Air as the surrounding medium.

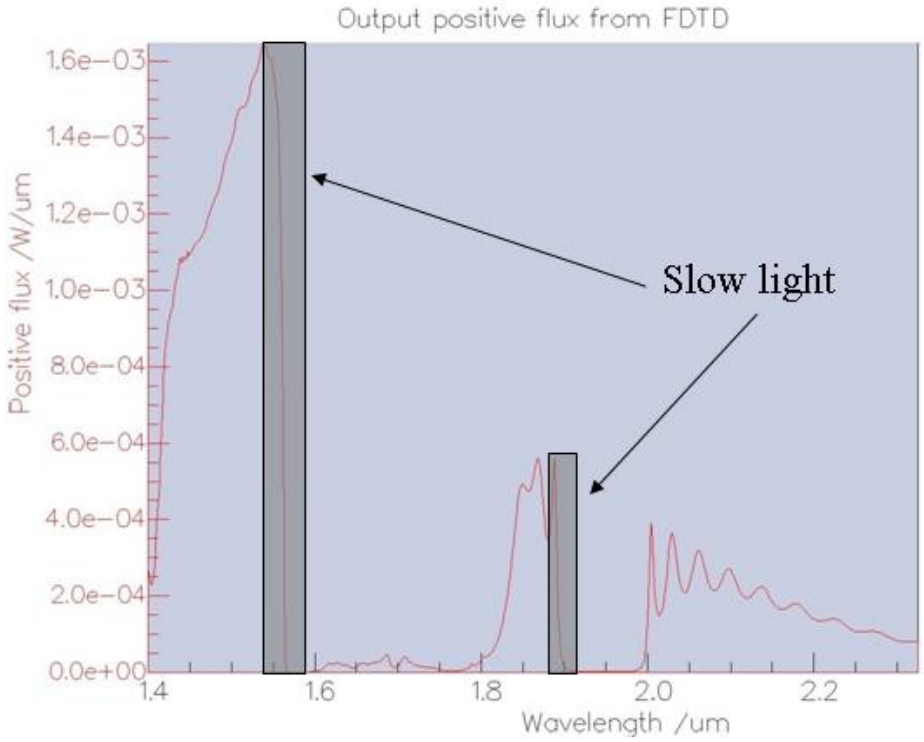

Figure 53a: CrystalWave simulated Output of InP PhC gas sensor for Air. The two slow light regions are marked with grey outlines

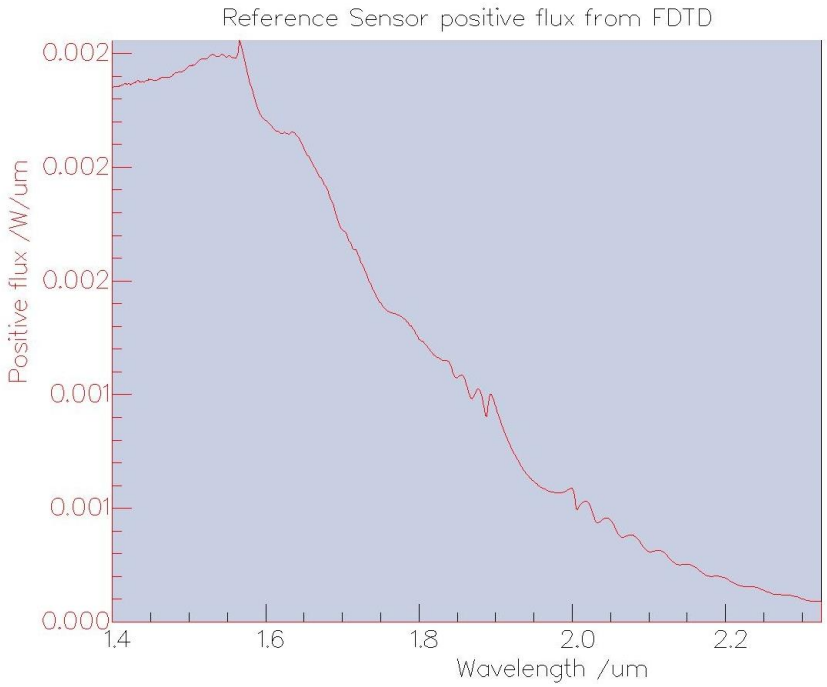

Figure 53b: Broadband input pulse used to excite InP PhC waveguide (with Air as surrounding gas).

The slow light regimes are marked with grey outlines in Figure 53a. The photonic crystal is capable of supporting at least two slow light regimes centred around 1.5 μm and 1.9 μm. From a theoretical perspective either of these two regimes can be used to sense different gases but practically, the regime in the C-band (i.e. centred around 1.5 μm) is the most practical for the purposes of building a gas sensor (and the optical sensor mote) that can be used for real world applications. Figure 53c shows a zoom-in on the C-band centred slow light regime.

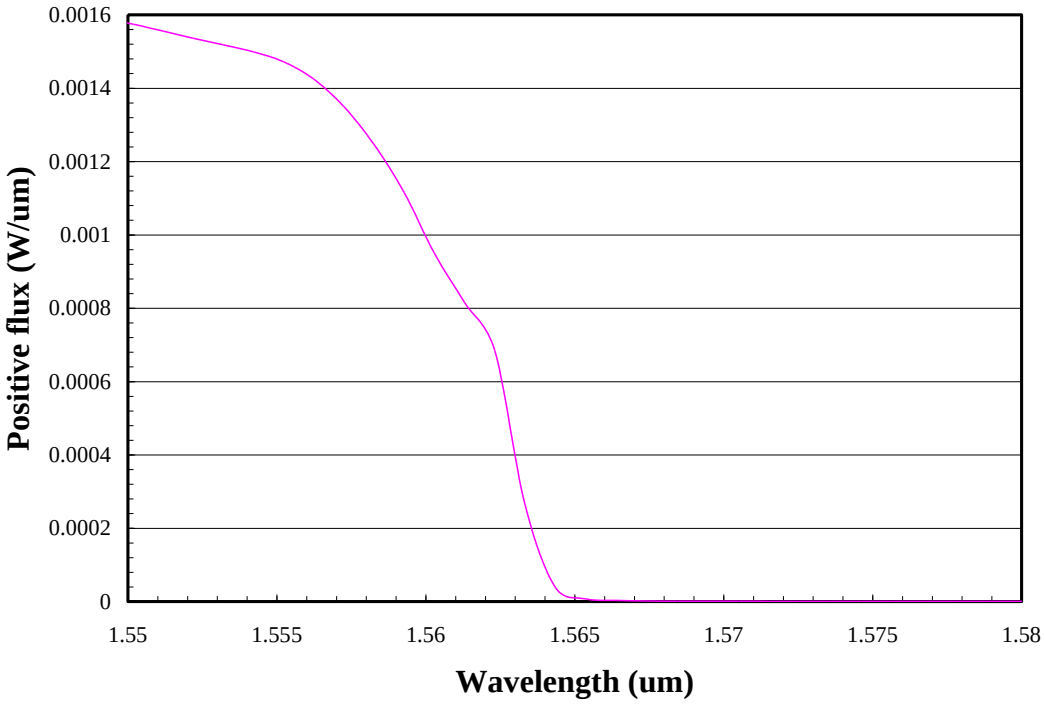

Figure 53c: Zoom-in of the C-band centred simulated slow light regime of the InP PhC gas sensor (with air as the surrounding gas).

The sensor's response to helium (He) gas was simulated and found it to be identical to Air. However, upon further investigation and correspondence with PhotonD (makers of CrystatWave) it turned out that the version of the software lacked the capabilities to accurately model the shift in the slow light regime due to a change in the surrounding medium (as opposed to the shift in resonance of a localized cavity as was done in previous sections) due to the required spectral resolution. The majority of reported values for gas sensing using InP photonic crystals (resonant cavities) reported wavelengths shifts in the range of 8 to 200 pm [Sünner, et al. 2008; Zaho et al. 2011; Passaro et al. 2012a], a resolution that was unattainable with CrystalWave given the available computing resources (it would take almost 2 weeks to simulate a single gas). Thus, an alternative simulation approach was sought to perform a theoretical analysis and investigate the properties of the proposed gas sensor. The solution was to abandon the FDTD approach and instead utilize a frequency based approach as discussed in Section 3.5.6.

However, since the sensor is RI based and has the capability to sense refractive index changes of not just gases, but liquids as well, since the latter present a significantly higher refractive indices compared to Air, e.g. refractive index of water at 1.55 μm, 25 °C is 1.318 [RefIndex 1] compared to Air's of 1.0002736, this large difference in refractive index indicates a shift in the slow light of photonic crystal sensor of several tens of nanometers, a resolution that is easily achieved by available computing capabilities using the FDTD approach. Figure 54 shows the transmission spectrums of the sensor (given parameters found in Table 17, Section 3.5.6) of Air and water.

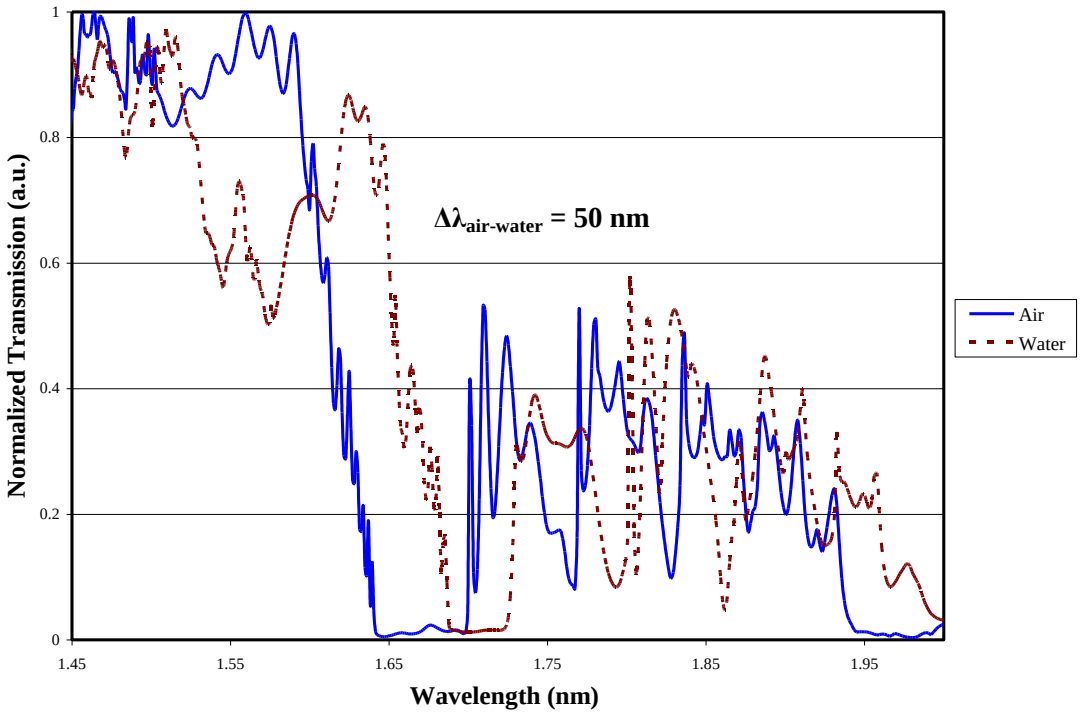

Figure 54: (normalized) Transmission spectrums of sensor for Air (solid line) and Water (dashed line).

The slow light mode of the sensor in the presence of water (i.e. immersed in it) has shifted in wavelength compared to the slow light mode of the sensor in the presence of Air. Furthermore, since $n_{Water} > n_{Air}$, the slow light mode of water shows a red shift in wavelength, i.e. lead the slow light mode of Air [Joannopoulos et al. 2008; Sünner, et al. 2008; Lai et al. 2011].

The result theoretically proves the viability of the sensor and supports the hypothesis that the slow light mode can be used to sense liquids (Section 3.5.6 proves this for gases). The shift is 50 nm, detectable with a low quality OSA. The situation will be different for gases as discussed in the next section, however the shifts simulated and experimentally verified are also detectable with high quality OSA. The simulation

parameters (Table 17) were chosen because they corresponded to the best available experimental sample and are used in the comparison with experimental results of Section 3.6.6.

3.6.5 MIT MPB Simulations: Frequency based approach.

The MIT Photonic Bands (MPB) is free software developed by Steven G. Johnson at MIT to calculate the electromagnetic bands structures (i.e. dispersion relations) of period structures including of photonic crystals [MPB]. The program computes the eigenstates of the photonic crystal in a fully vectorial and 3D approach. The eigenstates represent the harmonic modes of the Maxwell equations of the photonic crystal.

MBP is particularly suited to simulate the devices under investigation as the frequency based approach allows for a much faster simulation time and with modest computing power as well as providing the necessary spectral resolution (in pm range) to accurately investigate the sensing capabilities of the proposed sensor.

Extensive simulations of the proposed sensor using MPB were undertaken to verify the operating principle of the sensor as well as theoretically evaluating one of the sensor's most important parameter, its wavelength sensitivity. Some of the simulations were confirmed by experimental results as discussed in Section 3.5.6.

The straight waveguide sensor structure of Figure 50, Section 3.5.4, with the parameters summarised in Table 17 was simulated. These parameters corresponded

to the best available experimental sample and were chosen for comparison with experimental results.

Table 17: MPB simulation parameters for the InP PhC.

PhC Parameter	Value
Structure	Air Bridge
Lattice constant, a	441 nm
Filling Ratio, $\frac{r}{a}$	0.24
Slab thickness, t	285 nm
Substrate thickness	1000 nm

By comparing the dispersion relations of the photonic crystal sensor for different gases, the slow light wavelength shifts that the sensor experiences in the presence of various gases with respect to the reference gas, Air, were calculated; a number of gases were simulated in order to characterise sensor performance and determine its sensitivity. Table 18 summarises the various gases simulated with their refractive indices at 1.55 μm; the refractive index values were sourced from [RefIndex 1], [RefIndex 2], [RefIndex3].

Table 18: Refractive indices (at 1.55 μm) of various gases.

Gas	Refractive Index, n (RIU)	Reference
He	1.00003471	[Refindex 1]
Air	1.00027326	[Refindex 1]
Argon	1.00027787	[Refindex 1]
Ammonia (NH_3)	1.0003738	[Refindex 1]
Methane (CH_4)	1.0004404	[Refindex 2]
Methanol (CH_3OH)	1.000586	[Refindex 2]
Sulphur Dioxide (SO_2)	1.000686	[Refindex 2]
Sulphur Hexafluoride (SF_6)	1.000783	[Refindex 3]
Ethanol/Ethyl Alcohol	1.000878	[Refindex 2]
Acetone	1.00109	[Refindex 2]
Ethyl Ether	1.001533	[Refindex 2]
Benzene	1.001762	[Refindex 2]

Table 19 shows the simulated wavelength shifts of the slow light regime of the sensor due the presence of various gases. As usual, Air is chosen as the reference gas, its wavelength shift set to a value of zero picometers (pm). Figure 55 depicts the refractive index of the various gases against the simulated wavelength shifts of the (resonant) slow light mode. The data was fitted to a linear line and showed good linearity.

Table 19: Simulated responses of InP slow light sensor to presence of various gases.

Gas	Refractive Index, n (RIU)	λ shift with respect to Air (pm)
He	1.00003471	-60
Air	1.00027326	0
Argon	1.00027787	5
Ammonia	1.0003738	22
Methane	1.0004404	36
Methanol/Methyl Alcohol	1.000586	64
Sulphur Dioxide	1.000686	87
Sulphur Hexafluoride (SF_6)	1.000783	105
Ethanol/Ethyl Alcohol	1.000878	124
Acetone	1.00109	170
Ethyl Ether	1.001533	262
Benzene	1.001762	308

As expected, linear relationships exist since the slow light mode can be viewed as a particular resonance of the photonic crystal waveguide and thus will vary linearly with changes in the refractive index of the waveguide. From Figure 55, the (theoretical) wavelength sensitivity, S_λ, of the sensor according to equation 2 (i.e. the slope of the line) [Passaro 2013; Passaro et al. 2013] can be calculated as;

$$S_\lambda = \frac{\Delta\lambda}{\Delta n} = 211 \ \ nm/RIU \qquad (44)$$

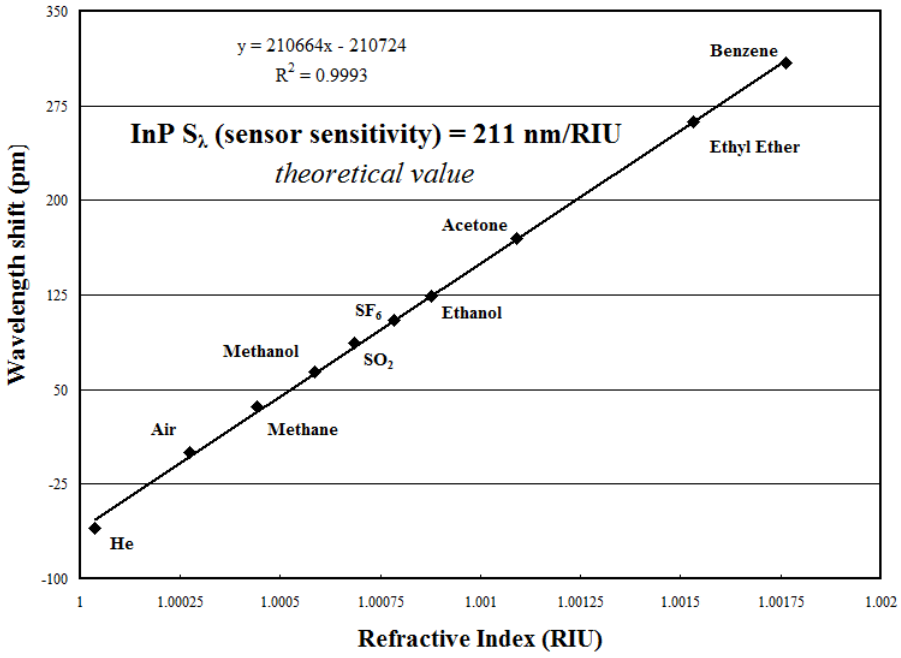

Figure 55: Theoretical wavelength shifts of InP slow light mode of sensor due to gases.

It is important to note that the wavelength shifts of the slow light mode range from 5 to 300 pm, values that are readily measurable with current technologies (Section 3.5.6) and fall within the range of expected values for photonic crystal gas sensors reported in the literature [Zhao et al. 2011; Passaro 2013]. These sensors are of the same class as the proposed sensor but do not utilize the slow light regime in sensing (Section 3.3 and Section 3.6.2). Most reported sensors utilize the localized cavity approach, using the normal/fast light regime. At this point, it is worth comparing the theoretical result to a reported sensor in literature [Sünner, et al. 2008]. This sensor is choosen to make the comparison because: 1. the same material technology, InP, 2. experimental results with similar gases, and 3. a resonant cavity. This RI photonic

sensor does not utilize the slow light to enhance light-gas interaction, rather it seeks to enhance the interaction by strongly confining the light within a resonant cavity.

The reported experimental sensitivity [Sünner, et al. 2008] was 80 nm/RIU viz. 8 pm shift in the resonance wavelength of the cavity for a change of 10^{-4} in RI. The calculated theoretical sensitivity for the sensor is 211 nm/RIU (the experimental value is estimated to be 190 nm/RIU but based on a more limited set of data points, Section 3.6.6) Thus, the proposed sensor has an almost 2.4 times better sensitivity than that reported in [Sünner, et al. 2008]. As previously discussed in section 3.6.2, this improvement is due to utilizing the slow light mode instead of a L3 cavity, which utilizes the fast light mode as the slow light interacts more strongly with matter and thus utilizing it allows us to build more sensitive sensors [Krauss 2007; Lambrecht et al. 2007; Jensen et al. 2008; Wang et al. 2010; Pergande et al. 2011; Zaho et al. 2012; Zhang et al. 2012]. Further experimental work is needed to better characterize the magnitude of the improvement.

Furthermore, slow light RI sensors in SOI technology (Section 3.4) will potentially provide better performance than a slow light RI sensors in InP, since SOI photonic crystals confine the light more strongly (due to the stronger refractive index contrast between Si and SOI). The hypothesis was validated by executing a similar set of the simulations carried out for the InP sensor (Table 19 and Figure 55) for an identical (in structure, i.e. a straight waveguide, Figure 50) SOI sensor. The parameters of the SOI sensor are presented in Table 5, Section 3.4.5.

Table 20 presented the simulated wavelength shifts of the slow light regime of the SOI sensor due the presence of various gases. As usual, Air is chosen as the reference gas, its wavelength shift set to a value of zero pm (picometers). Fig 56 plots the refractive index of the various gases against the simulated wavelength shifts of the (resonant) slow light mode of the SOI sensor. The data was fitted to a linear line and showed excellent linearity. From Fig 56, the theoretical wavelength sensitivity, S_λ, of the SOI sensor (also according to Equation 2) can be calculated as;

$$S_\lambda = \frac{\Delta\lambda}{\Delta n} = 246 \quad nm/RIU \qquad (45)$$

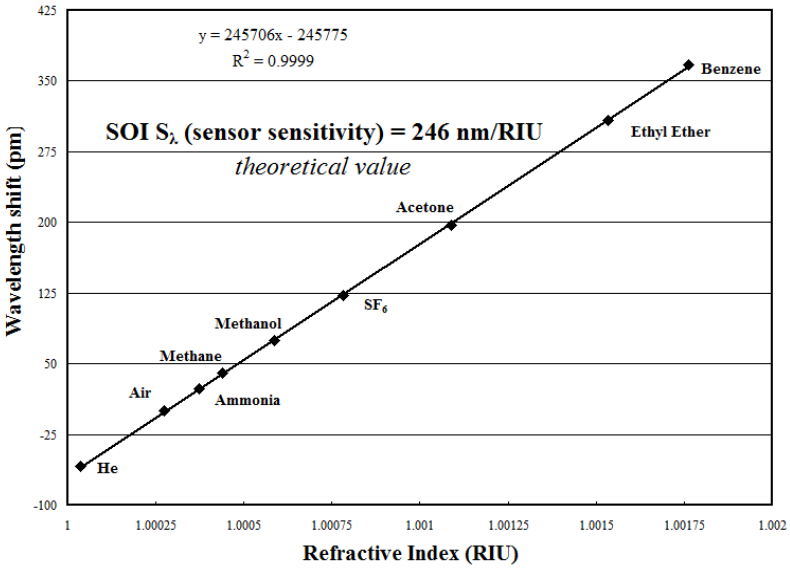

Figure 56: Theoretical wavelength shifts of SOI slow light mode of sensor due to gases.

Table 20: Simulated responses of slow light SOI sensor to presence of various gases.

Gas	Refractive Index, n (RIU)	λ shift with respect to Air (pm)
He	1.00003471	-59
Air	1.00027326	0
Ammonia	1.0003738	24
Methane	1.0004404	40
Methanol/Methyl Alcohol	1.000586	75
Sulphur Hexafluoride (SF_6)	1.000783	122
Acetone	1.00109	197
Ethyl Ether	1.001533	308
Benzene	1.001762	367

A significant improvement in the sensor's sensitivity is achieved with a SOI sensor implementation as compared to an InP device aligned with general photonic crystal waveguidng theory [Joannopoulos et al. 2008]. It is important to note however that this remains a theoretical evaluation and robust experimental work should be carried out to verify the hypothesis in practice. Access to functioning SOI photonic crystal sensors (as discussed in Section 3.4.8) was not available rendering experimental verification impossible.. However, it is well established in literature that SOI photonic crystals have considerably better performance (in particular significantly lower losses) than InP and this is due to the stronger confinement of light [Joannopoulos et al. 2008]. Thus, experimental verification to match theoretical

results is supported by reported research to date but the actual magnitude of improvement remains to be determined.

Finally, the effect of the Air hole size, r, on the sensitivity of the sensor was investigated; a range of simulations for various values of r were undertaken, Table 21 and Figure 57 showing the results. A significant improvement in the sensor's sensitivity is indicated if r is increased (provided that a photonic band gap continues to exist, verified for all values of r in the simulations). The changeable area (Air with gas) in the photonic crystal sensor with larger holes is larger than in the photonic crystal sensor with smaller holes. Thus, there is a larger refractive index change in sensors with larger r resulting in a larger sensitivity

Table 21: Effect of varying r values on InP sensor's sensitivity.

r (nm)	Sensitivity (nm/RIU)
1. 0.4a = 176	743
2. 0.24a = 106	211
3. 0.20a = 90	150
4. 0.18a = 79	120

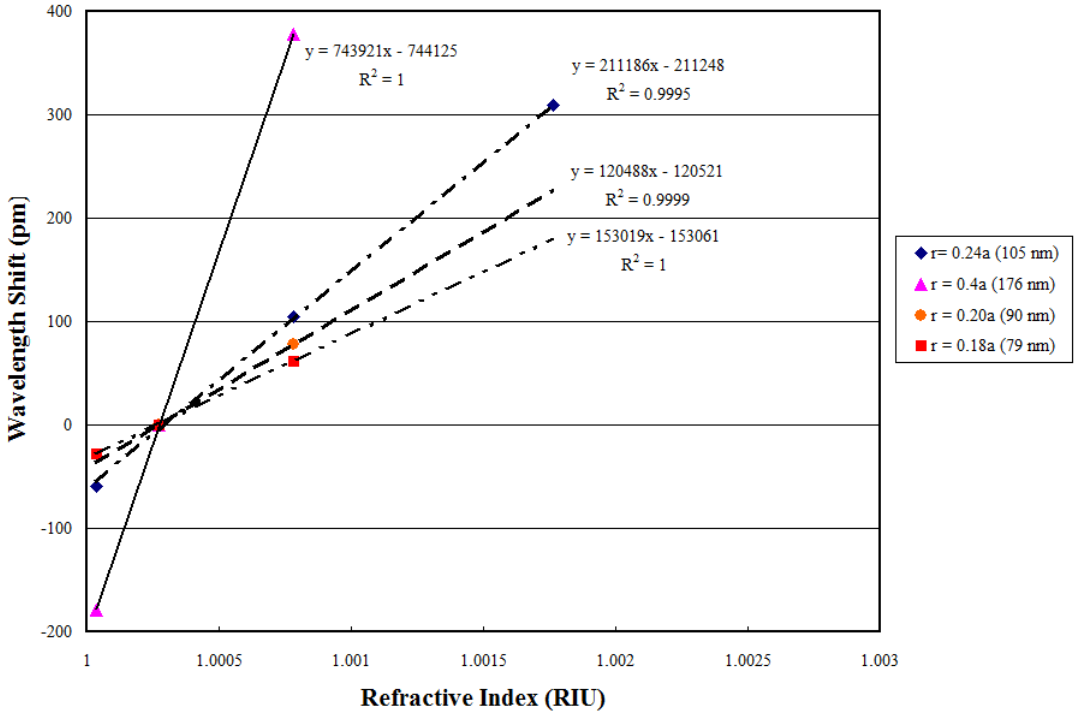

Figure 57: Theoretical wavelength shifts of InP slow light mode of sensor with varying r values due to gases.

In conclusion, two multi-gas slow light RI photonic in two different material systems (SOI and InP) have been theoretically evaluated and results indicate the wavelength shifts owing to the presence of various gases with a high sensitivity of 211 nm/RIU (InP) and 246 nm/RIU (SOI). The sensors utilizes the slow light mode of a photonic crystal waveguide for gas sensing [Awad et al. 2011; Passaro 2013; Passaro et al. 2012c]. SOI sensors have better sensitivity than InP sensors due to the tighter guiding of the waveguide modes and demonstrated that the sensitivity of the sensor can be improved by increasing the Air hole sizes (provided a band gap continues to exist). The sensors fall under the class of RI photonic crystal sensors but instead of utilizing a resonant cavity (e.g. L3 ref) for sensing, they utlize the slow light

(resonant) mode regime of a photonic crystal waveguide. Thus, the sensors are classified as slow light RI-based photonic crystal sensors.

3.6.6 Fabrication and Experimental Results

The InP photonic crystal waveguides were fabricated at NRC's fabrication centre [Mnaymneh 2011]. The fabrication ensured that the photonic crystal waveguide had a proper Air bridge structure to ensure symmetry and the formation of an appropriate photonic band gap similar to Figure 49.

A range of photonic crystal devices with different parameters were fabricated: 1. lattice constant, a = 441 and 465 nm, Air hole radius, r = 0.21a, 0.23a, 0.24, and 0.36a, and 3. slap thickness, t = 285 nm (Table 12, Table 15, and Table 17). After inspection, all experimental investigations centred on two samples with parameters captured in Table 22, and simulated in Section 3.6.5. Figures 58 depicts a SEM of the fabricated sensor, illustrating high fabrication quality.

Table 22: Parameters for InP sensor under experimental investigation. Thickness refers to slap thickness, t.

Sample	Structure	Lattice constant, a	Hole radius, r	Thickness, t
1	Air bridge	441 nm	r = 0.20a = 90 nm	285 nm
2	Air bridge	441 nm	r = 0.24a = 106 nm	285 nm

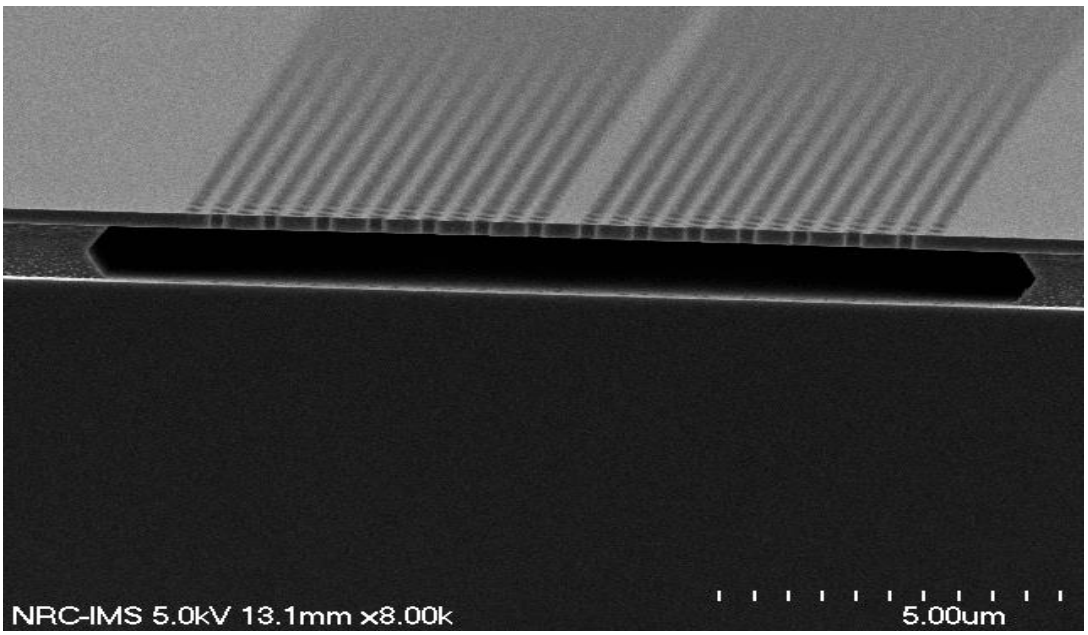

Figure 58: SEM side view scan of InP photonic crystal sensor showing the Air bridge.

Experiments were performed to confirm the operation of the proposed gas sensor. The experimental setup is shown in Figure 23 and utilized free space optics to couple the light out of the photonic crystal through a graded index (GRIN) lens fibre collimator [Thorlabs] mounted on a custom made holder (Figure 59 and Figure 60). The GRIN fibre collimator is a hybrid component: one end is a GRIN lens for free space coupling of light (from the photonic crystal sensor) and the other is a standard SMF which is connected to, e.g. an OSA. This hybrid approach (free space and fibre optics) minimizes the effects of any environmental perturbations on the setup and these critical experimental measurements. Considerable care was taken to minimize the effects of environmental perturbations: temperature of the sensor, the environment, humidity, optical table vibrations. The flow of gases (via gas meters

and specialized dispensing tubes) were strictly controlled, monitored, and kept constant over the course of the experimental runs.

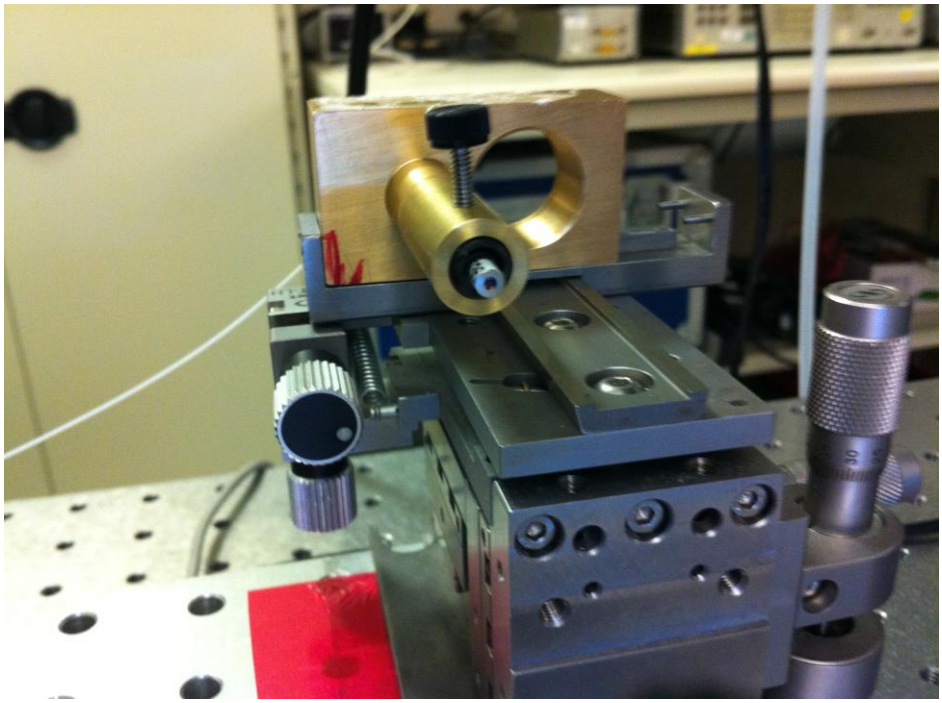

Figure 59: GRIN lens fibre collimator mounted on a special holder. One of the fibres end is free space GRIN lens and the other is connected to an OSA

The same broadband source as in Figure 23 was used, the JDS BBS 1590, which emitted between 1440nm-1630 nm. The simulation results (Section 3.6.5) indicated that the wavelength shifts were of the order of picometers (pm) necessitating the use of a high resolution OSA to accurately detect the changes; a Yokogawa AQ6370C high resolution OSA [Yokogawa] was utilised. The OSA has a high spectral resolution of 10 pm (0.01 nm), ideal for detecting the slow light shift for all the gases

of interest. The predicted slow light shifts of 60 pm for He and over 100 pm for SF6 are well within the resolution limit of the OSA.

Transmission spectrums of the photonic crystal waveguide TE mode for two gases were measured: 1) Air, with refractive index, n_{Air} = 1.00027326 [RefIndex 1], and 2. Sulphur hexafluoride (SF6), with refractive index n_{SF6} = 1.000783 [RefIndex 3]. Figure 60 shows the TE normalized transmission spectrum for Sample 1 (r = 0.2a = 90 nm) of the sensor for Air with the slow light regime marked.

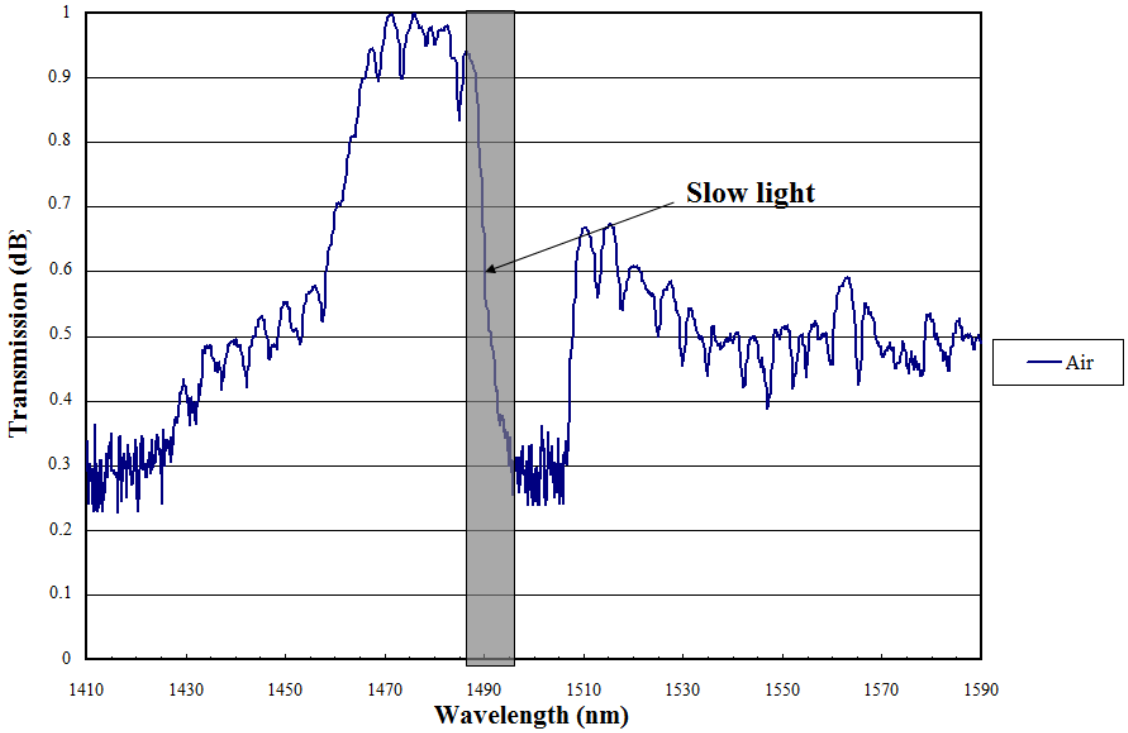

Figure 60: TE (normalized) Transmission spectrum of Sample 1 InP sensor (r = 90 nm) for Air.

The fabricated InP photonic crystals are capable of supporting a slow light mode. The slow light regime is centred around 1.49 μm as opposed to 1.56 μm as predicted by simulations in Figures 53a and 53c. This can be attributed to the fact that the actual fabricated structure had slightly different lattice constant and Air hole radius values than for the simulated one. Furthermore, the spectrum in Figure 60 is not as smooth as the simulated spectrum and exhibits a number of resonances (from, e.g. backscattered reflections, the result of fabrication imperfections). Figure 61 shows a zoom-in of the slow light regime for Sample 1 (r = 0.2a = 90 nm). Sample 2 (r = 0.24a = 106 nm) had a slow light regime centred around 1.45 μm. i.e. as the Air holes size increases, the transmission spectrum (including the slow light mode) blue shifts, in agreement with photonic crystal waveguiding behaviour which states that as the Air hole size is increased, the band structure shifts to higher energy and thus blue shifts [Joannopoulos et al. 2008]; $\lambda_{\text{slow light- r=0.20a}} > \lambda_{\text{slow light- r=0.24a}}$.

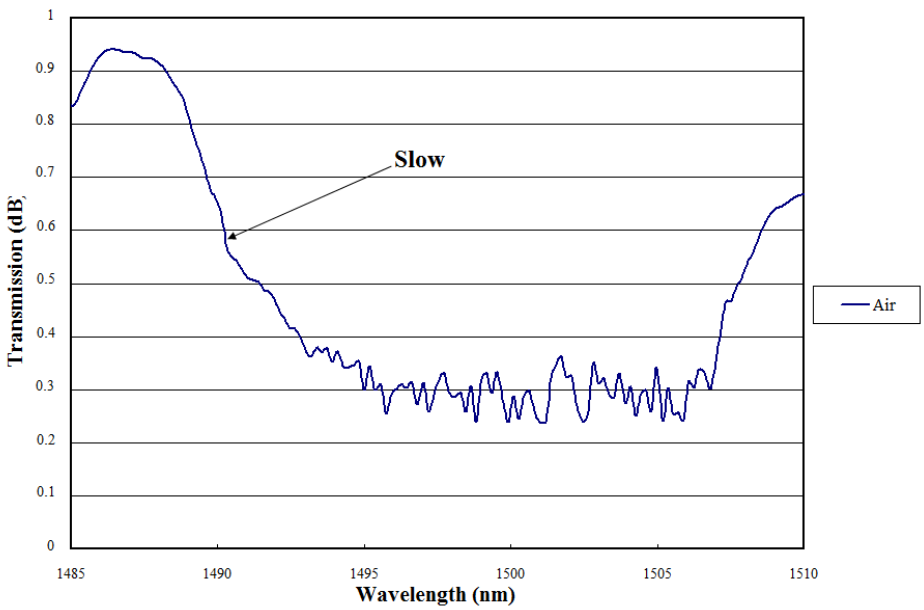

Figure 61: Zoom-in of the slow light regime of Sample 1 of InP sensor (r = 90 nm) with Air as the surrounding gas.

With the sensor initially filled with Air (to create a reference condition), a tapered hose was used to cover the photonic crystal waveguide sensor evenly with Sulphur Hexafluoride (SF6) gas from a portable cylinder and its output spectrum was measured. This experiment was performed three times for Sample 2 (r = 106 nm) resulting in six spectrums: 1. Air 1 and SF6 1, 2. Air 2 and SF6 2, and Air 3 and SF6 3. Figure 62 shows the slow light regimes of Sample 2 for Air and SF6 gases, Figure 63 shows the slow light regimes for Sample 2 for Air gas only and Figure 64 shows the slow light regimes for Sample 2 for SF6 gas only.

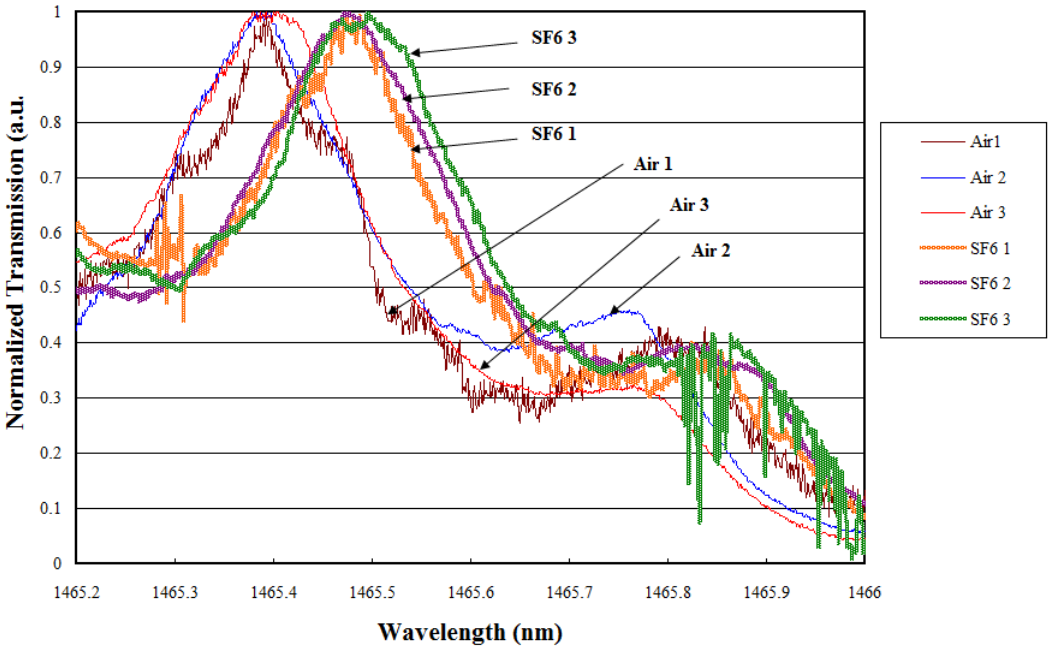

Figure 62: Normalized slow light regimes of Sample 2 of InP sensor (r = 106 nm) for Air and SF6 gases for three experimental runs.

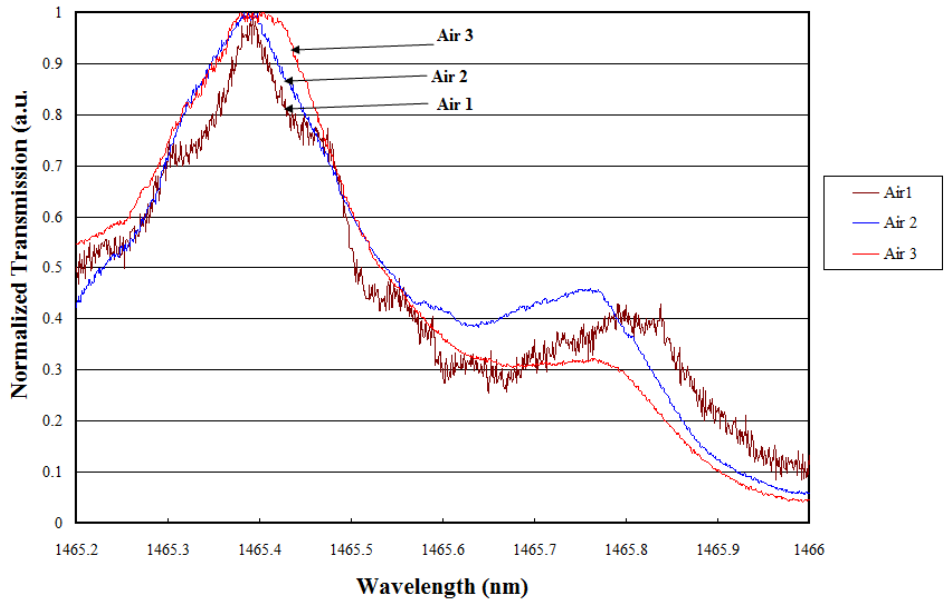

Figure 63: Normalized slow light regimes of Sample 2 of InP sensor (r = 106 nm) for Air gas for three experimental runs.

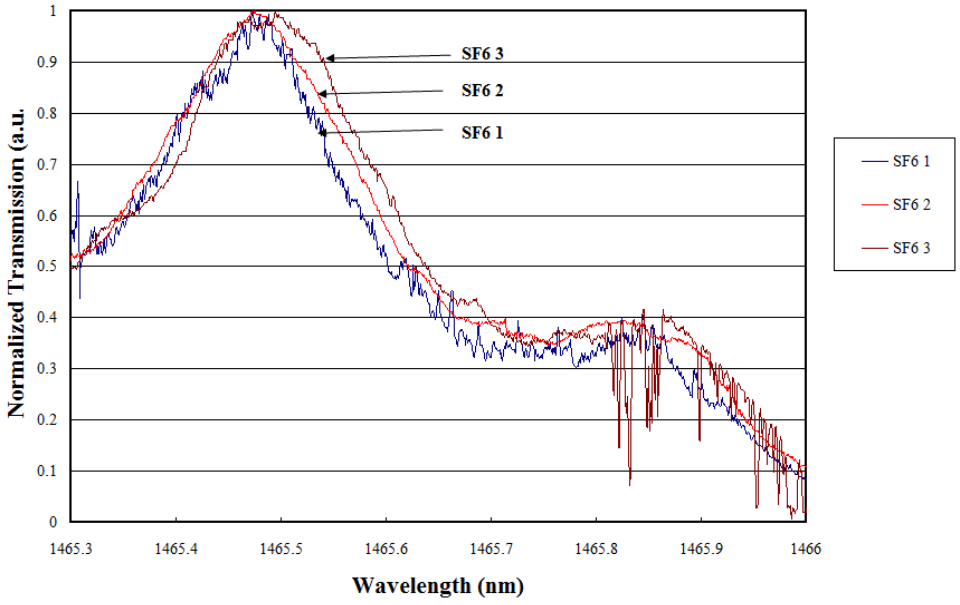

Figure 64: Normalized slow light regimes of Sample 2 of InP sensor (r = 106 nm) for SF6 gas for three experimental runs.

Figure 62 highlights a significant experimental result: there is a clear difference in wavelength profile between the slow light modes of the transmission spectra of Air and SF6. The sensor has the potential to distinguish between the presence of two gases. This result represents the first demonstration of using the slow light mode of a photonic crystal to perform gas sensing in this configuration. Furthermore, as is evident from Figure 62, the SF6 slow light mode leads that of Air since $n_{SF6} > n_{Air}$ and, again, is in accordance with photonic crystal waveguiding theory and published results for gas sensing using RI photonic crystal sensors [Joannopoulos et al. 2008; Sünner, et al. 2008; Passaro 2013; Passaro et al. 2012c].

Figure 63 and Figure 64 demonstrate an important issue common to photonic crystal sensors, their high sensitivity to environmental perturbations. The Air spectra differ slightly from each other over the course of repeated measurements as do the SF6 spectra. Similar results showing such variations of the output of photonic crystal sensors for the same gases have been commonly reported in literature. In particular, [Sünner, et al. 2008; Jágerská et al. 2010; Jágerská et al. 2010b; Liu and Salemink 2012] have reported similar experimental variations for (gas and liquid) photonic crystal sensors utilizing the fast mode, whereas [Ruperez et al. 2010] reported similar experimental variations for liquid photonic crystal sensors utilizing the slow mode.

These variations can be attributed to the high sensitivity of photonic crystal to environmental perturbations such as temperature, pressure, humidity adsorbed at the structure sidewalls, or progressive oxidation of the sample surface. These perturbations alter the guiding conditions of the photonic crystal waveguide as well

as the photonic crystal band structure resulting in the variations observed in the output of the sensor [Rindorf and Bang 2008; White et al 2008; Wolinski et al. 2008; Karnutsch et al. 2009; Jágerská et al. 2010; NAir and Vijaya 2010; Ruperez et al. 2010; Kumar et al. 2012; Zaho et al. 2012; Zhang et al. 2012].

The effect of environmental perturbations can be controlled by utilizing environmental controls such as temperature, moisture, and pressure stabilization. It is important to note that in the experiments, the output variations were quite small and did not affect the accuracy or the successful operation of the sensor. Figure 62 clearly shows that, despite variations in both the Air and SF6 individual spectra (which can be thought of as perturbations of the reference spectra, i.e. Air 1 and SF6 1), the differences between the Air and SF6 spectra are very pronounced and much larger (in wavelength) than the environmentally induced variations. The sensor is able to distinguish between Air and SF6 spectra despite environmental perturbations. It is understood that continuous environmental stabilization is needed for sensor operation, more easily achieved when the sensor is packaged and hermetically sealed.

Figures 65, Figure 66, and Figure 67 show the slow light regimes for Sample 2 (r = 106 nm) for Air 1 and SF6 1, Air 2 and SF6 2, and Air 3 and SF6 3 respectively. The wavelength shift between the Air and SF6 slow light regimes is clear and verifies the operation of the sensor. An important issue to note is that the Air and SF6 slow light spectra are not perfectly parallel to each other, i.e. the difference in wavelength is not the same but varies slightly due to the marginally different slopes of both slow light

regimes. Similar results for photonic crystals fast light (gas and liquid) sensors [Buswell et al. 2008; Dorfner et al. 2008; Robinson et al. 2008; Sünner, et al. 2008; Wolinski et al. 2008; Jágerská et al. 2010b; Wang et al. 2010; Lai et al. 2011; Scullion et al. 2011; Chakravarty et al. 2012; Liu and Salemink 2012] and slow light liquid sensors [Ruperez et al. 2010] have been reported in literature, where the profiles for the fast and slow light modes for different gases and liquids were different in shape and slope.

The explanation for this lies in the fact that the photonic crystal sensor guides light using two mechanisms: 1. Index Guiding, and 2. Band gap guiding (Section 3.2). Different refractive indices (due to different gases like Air and SF6) affect both these guiding mechanisms; the propagating mode in the photonic crystal experiences different index guiding conditions (due to the different refractive index in the cladding layer, i.e. the Air membrane around the waveguide) and the photonic band structure will also be altered by the change in the index due to the change in the surrounding gas (the change in refractive index affects the light line of the photonic crystal which results in altering the out-of-plane scattering losses [Joannopoulos et al. 2008]) . Both these effects result in different mode "profiles" or "shapes" and thus the slow light regimes for different gases will not be identical in shape and will present different slopes [Joannopoulos et al. 2008; NAir and Vijaya 2010; White et al. 2008]. However, despite these minor differences, the wavelength difference between the Air and SF6 slow light regimes is clear indicating the sensor's ability to successfully distinguish between the two gases.

Furthermore, the wavelength difference between the Air and SF6 slow light regimes for all experimental runs was consistent (estimated to be roughly 97 pm), noting that all experimental runs were performed at slightly different times viz. environmental perturbations and variations did not negatively affect sensor performance. The slow light regime is an intrinsic property of the photonic crystal waveguide and thus, despite shifts in wavelength due to environmental perturbations, the difference between one slow light regime and another is still the same because both slow light modes shift in a way to preserve the wavelength relationship between each other, provided that the measurements for both slow light regimes are performed in quick succession so as to make for a valid comparison as was the case in the experimental runs in this work.

The different slopes of the slow light modes raises the question of at what point on the characteristic should the measurement be taken to determine the wavelength difference that distinguishes between the two gases. This issue is not discussed extensively in literature as most reported photonic crystal sensors utilize cavity resonances with sharp peaks as opposed to slow light modes and so the measurements are typically taken at the peak of the resonance (e.g. Figures 13 and 14, section 3.4.6). The most logical course of action is to take several measurements along the slow light regime and produce an average as is shown in Figure 65, Figure 66, and Figure 67. It is important to note however that, even if only a single point is used as a measurement, the result is still close to the result obtained from the averaging approach e.g. for the case of Air 2 and SF6 2, the average wavelength shift

is 92 pm whereas the single measurements are 97 pm, 95 pm, and 85 pm. It is also conceivable to utilize the start of the slow light regime as a measurement point

An additional note regarding the result of Air 1 and SF6 1 is worth highlighting: it is believed that the Air 1 spectrum was distorted due to the OSA settings and this resulted in the kink in the spectrum. This kink is not present in Air 2 and Air 3 spectra and the kink does not affect the sensor's ability to successfully distinguish between Air and SF6 and the result is consistent with other experimental results (Air 2 and SF6 2; Air 3 and SF6 3).

From Figure 65, Figure 66, and Figure 67 the shift in the slow light mode of the sensor due to the presence of SF6 (from the reference conditions of Air) is measured to be: 1. 95 pm for Air 1 and SF6 1, 2. 92 pm for Air 2 and SF6 2, and 3. 105 pm for Air 3 and SF6 3 (SF6 leads Air in all cases since $n_{SF6} > n_{Air}$). The average shift over all experimental runs is thus approximately 97 pm i.e. for a $\Delta n_{Air\text{-}SF6} = 5.10 \times 10^{-4}$, a $\Delta\lambda = 97$ pm is measured (SF6 leads Air). Table 23 summarises the results.

Table 23: Summary of wavelength shift results for Air and. SF6.

Experiment	**$\Delta_{Air\text{-}SF6}$ (pm)**
Air 1 and SF6 1	95
Air 2 and SF6 2	92
Air 3 and SF6 3	105

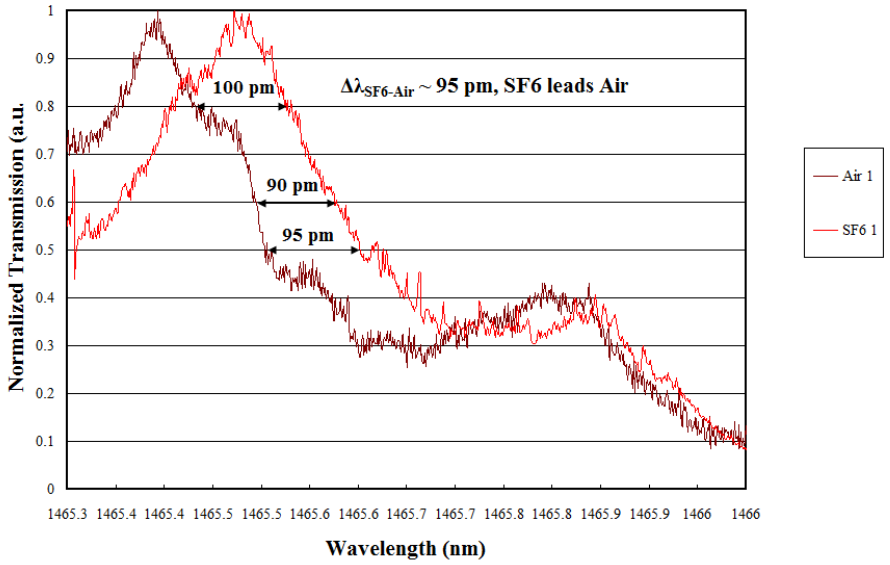

Figure 65: Normalized slow light regimes of Sample 2 of InP sensor (r= 106 nm) for Air 1 and SF6 1 gases (1st experimental run).

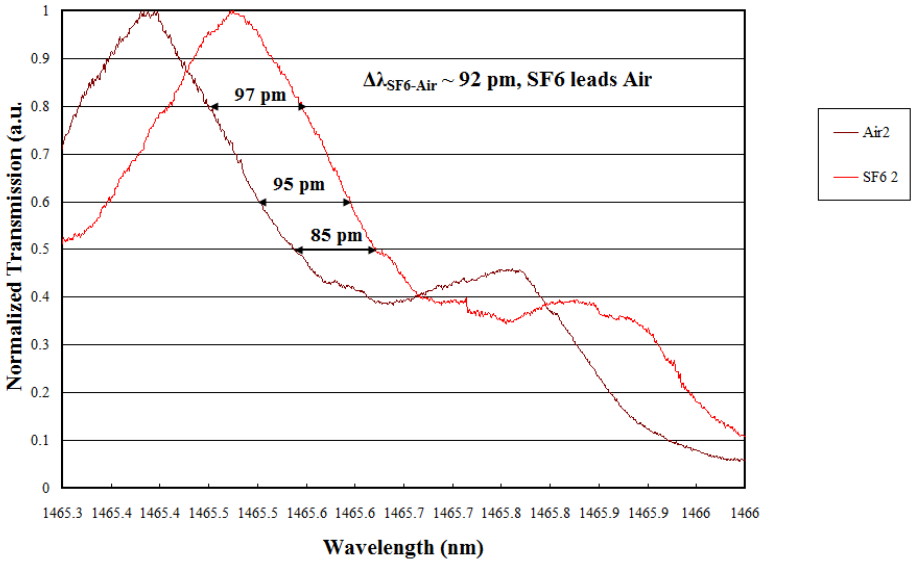

Figure 66: Normalized slow light regimes of Sample 2 of InP sensor (r= 106 nm) for Air 2 and SF6 2 gases (2nd experimental run).

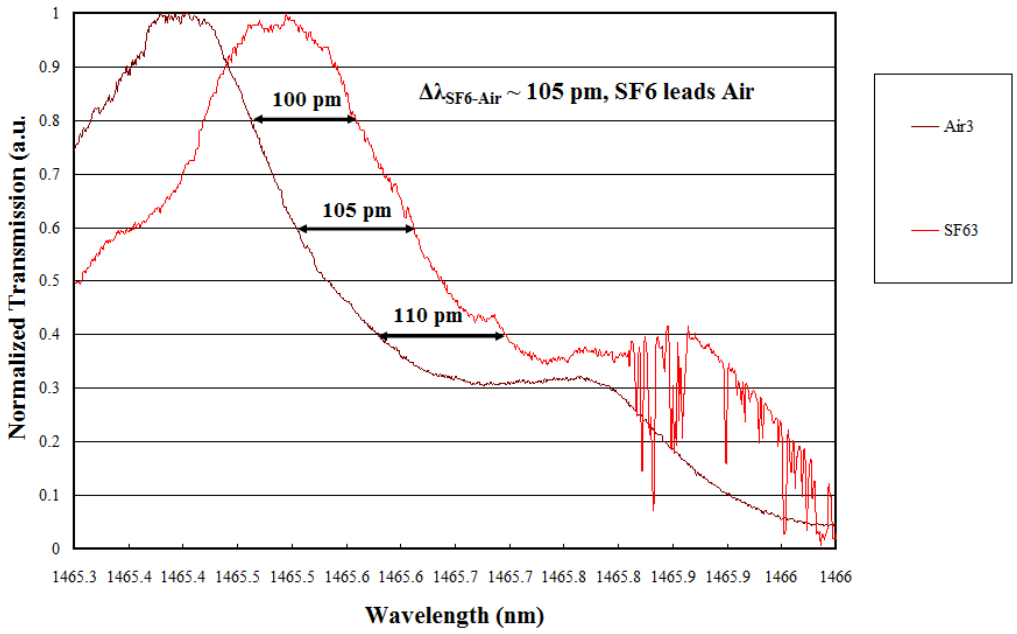

Figure 67: Normalized slow light regimes of Sample 2 of InP sensor (r= 106 nm) for Air 3 and SF6 3 gases (3rd experimental run).

A plot of the calculated experimental sensitivity is shown in Figure 68 together with the experimental wavelength sensitivity, S_λ, for the sensor according to Equation (2) (using the average value of 97 pm wavelength difference between Air and SF6):

$$S_\lambda = \frac{\Delta\lambda}{\Delta n} = 190 \quad nm/RIU \qquad (46)$$

The experimental sensitivity compares well with the theoretical sensitivity of 211 nm/RIU, given by Equation (44), both for the same Sample 2 (r = 0.24, a = 106 nm). It is important to note that the simulations were performed for many gases while the experiments were carried out for only two gases. This means that the experimental

sensitivity value is less accurate than the theoretical value owing to fewer data points to linearly fit experimental data. Due to a limit in time and lack of other gases and samples, additional experiments were not undertaken which would have increased the accuracy of the experimental sensitivity value. Nonetheless, the experimental results are in good agreement in magnitude and trend with the quantitative and qualitative theoretical results.

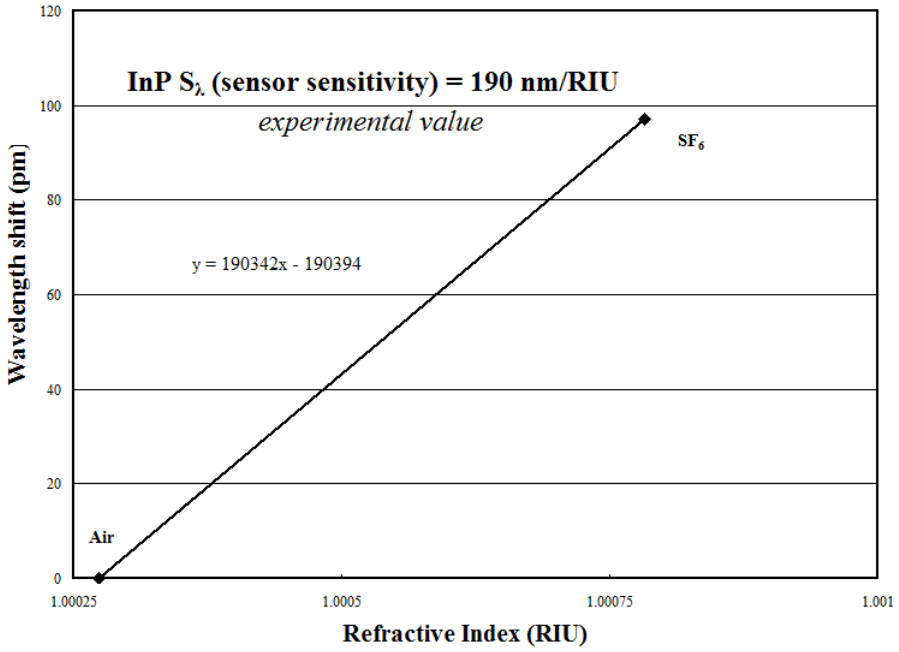

Figure 68: Experimental wavelength shifts of slow light mode of Sample 2 of InP sensor (r = 106 nm) due to gases.

In conclusion, the successful operation of the proposed gas sensor has been experimentally demonstrated and the viability of using the slow light regime in photonic crystals to sense gases even in materials that provide low refractive index contrast (with respect to Air) such as InP has been preliminarily confirmed. To the best of our knowledge, this is the first time such results have been published.

The demonstrated sensor can potentially be integrated with electronics, wireless RF and memory modules, elements which form the foundation for the development of an optical sensor mote. The preferred material system would be SOI - as opposed to InP - and the operation of a SOI sensor together with the potential to yield improved performance in terms of sensitivity has been verified through simulation.

The experimental sensitivity in [Sünner, et al. 2008] was reported to be 80 nm/RIU i.e. 8 pm shift in the resonance wavelength of the cavity for a change of 10^{-4} in RI. The theoretical and experimental sensitivity of the InP sensor under investigation (Sample 2: r= 0.24a = 106 nm) were 211 nm/RIU and 190 nm/RIU respectively. This represents a 2.4x improvement over the sensor presented in [Sünner, et al. 2008]. As discussed in Section 3.6.5, this improvement is due to utilizing the slow light mode instead of a L3 cavity, the latter utilizes the fast light mode. As slow light increase interaction more strongly with matter, harnessing it allows more sensitive sensors [Lambrecht et al. 2007; Jensen et al. 2008; Wang et al. 2010; Pergande et al. 2011; Zaho et al. 2012; Zhang et al. 2012] to be realised. However, it is important to note that the results are preliminary and additional experimental investigation is needed to further confirm the claims.

3.7 Conclusions

Based on the research to date, a novel multi-gas sensor based on SOI photonic crystal L3 cavities was proposed add theoretically analysed. These sensors are able to sense multiple gases without the need of any physical adjustment (e.g. additional filters, input sources, or chemical agents). The production run of these sensors failed

due to fabrication errors, hence the experimental validation of these sensors was not possible.

A novel multi-gas InP photonic crystal waveguide sensor was proposed, and characterised both through simulation and experiment. The sensor principle utilises the slow light regime and relies on the measurement of changes in the RI within photonic crystal waveguides. The viability of the successful use of the slow light mode to sense different gases has been initially demonstrated. These sensor implementations are also able to sense multiple gases without the need of any physical adjustment (e.g. additional filters, input sources, or chemical agents), providing a multi-functional solution useful in a wide variety of applications with almost no modifications.

All the proposed sensors are based on refractive index changes in photonic crystals. This makes these sensors susceptible to environmental changes (e.g. change in temperature and/or pressure) as such changes also affect the refractive index. Thus, the sensors require a certain level of environmental stabilization (e.g. temperature stabilization) to ensure that the refractive index changes are solely owing to the presence of a gas. This will require additional circuitry such as a TEC controller, circuitry which is widely available and exists in very small form factors (since almost all types of active devices require it). Therefore, the necessity of environmental stabilization will have a manageable cost penalty in the deployment of the proposed multi-gas sensors.

Additionally, all proposed sensors require a broadband laser source. The great majority of semiconductor laser sources are fabricated in InP or GaAs material (due to their direct band gap nature) which allows high levels of integration in the InP slow light based sensors, a significant advantage over the SOI sensors (resonant cavity or slow light based) because the integration of the laser source will be far easier in the former material system. The easy route to integration illustrates the potential attractiveness of the slow light gas sensing approach: the configuration allows the fabrication of effective gas sensors even in low refractive index contrast material while maintaining ease of fabrication.

The proposed strategy for the realisation of a multi-functional sensing platform at the outset was the ***optical sensor mote*** and these sensors are in principle format compatible to provide the critical function of the optical sensor . The proposed sensors are small in size, can be engineered to be functionally stable, and offer reasonable sensitivities to low density gas species. They were fabricated in SOI and InP and thus can be integrated with digital, Radio Frequency (RF), and power electronics on the same chip to form an enhanced ***optical-electronic sensor mote***. Therefore, the results in this Chapter are best viewed as preliminary corroboration of the viability of the proposed optical sensor mote.

The promise of multi-gas sensing adds further impetus to the optical sensor mote concept; a potential multi-functional sensing platform that can be utilized across a wide range of applications with limited need for modification. Such a solution would be of great scientific and commercial value.

An important consequence of using the slow light mode in a photonic crystal (for sensing or other applications) is its inherent lossy waveguding [Krauss 2007], seriously inhibiting their wide scale deployment. This can cause serious challenges for the wide scale deployment of these sensors. It will also negatively affect the sensor's performance (especially sensitivity) as the slow light mode will not interact as strongly with gas due to its high losses in the photonic crystal waveguide. However, a significant volume of research have been reported on the design of photonic crystal waveguides that are dispersion engineering to ensure an efficient slow light mode. [Schulz et al. 2010] provides details on how this may be achieved by special selection and design of the photonic crystal and its parameters.

Finally, Table 24 provides a comparison of the performance of the most recently reported photonic sensors including the sensors reported in the Thesis [Passaro et al. 2012c] in order to position the proposed sensor in relation to other implementations. It is important to note that, despite the fact that the photonic crystal waveguide have not been optimized for efficient slow light modes (and thus experience significant loss), the sensors sensitivity competes favourably with many of the currently published results. An improvement in performance is expected for dispersion engineering photonic crystals that are optimized for efficient slow light modes.

Table 24: Comparison of most recent photonic sensors performance [Passaro et al. 2012c; this research work].

Architecture	Gas	Operating Range	Performance
RI SOI, Slow light RI PhC. InP and SOI	Air, SF_6, He	Near-IR (1440 – 1600 nm)	3000 nm/RIU (RI SOI), 211 nm/RIU (Slow light-InP), 246 nm/RIU (Slow light- SOI), LOD ~4.5× 10^{-5} RIU
Air-slot PhC nanocavities	N_2, H_2, CO_2, Acetylene, Propane	Near-IR (1570 nm)	610 nm/RIU, LOD = 1×10^{-5} RIU
Polymer PhC dye-laser	Ethanol	--	$\Delta\lambda$> 0.01 nm, Ethanol concentration < 120 ppm
Silicon slotted microring resonant cavity	Acetylene	Near-IR (~1530 nm)	490 nm/RIU, LOD ~x 10^{-4}, Q = 5000
MEMS-tunable VCSELs (AlGaAs)	O_2, HF, N_2O, CH_4, HCl	Near-IR (~700 nm), 0.76 µm, 1.27 µm, 1.38 µm. 1.65, µm 1.75 µm	0.1-20 ppm
HR-LSPR (high resolution localised surface plasmon resonance).	He – N_2, He – Ar		$\Delta\lambda_{max}$ = 0.058 nm.
Photonic bandgap fiber (PBF)	Acetylene	Near-IR (1550)	Acetylene concentration < 2%
Hollow-core PBF	Methane	Mid-IR (3.1 – 3.4 _m)	50 ppm
Cascaded RR based on SOI slot waveguides	Methane, Ethane	Mid-IR (~3.39 _m)	224.4 µm.RIU, LOD = 1.95 x 10^{-5}

Chapter 4 Conclusion and outlook: the Optical Sensor Mote

4.1 Summary and concluding remarks

The research presented addresses a number of concepts related to sensing. The fundamental importance of optical techniques within the extensive sensing domain is discussed and the role within the area of Wireless Sensor Network (WSNs) concepts is developed. In general the latter provide a valuable set of design principles which potentially may results in significant advance in the optical sensing field, in particular due to their distributed nature, low cost, amenable to mass production, and relative ease of use and deployment (compared to existing wired solutions). This suite of design options has resulted in the deployment of WSNs in a multitude of applications, executing key functions hitherto not possible. In particular, WSNs are well suited to monitor large scale/area environments in a cost effective manner.

Nevertheless current WSNs have one major limitation namely their exclusive reliance on non-optical sensing techniques. This significantly limits their effectiveness as a sensing solution for a wide class of important environmental phenomena. Therefore, introducing optical sensing techniques within the WSN framework is attractive and enhances the functionality of current WSNs.

The monitoring of dangerous gases in (coal) mines was highlighted as a high impact practical application that potentially can be greatly served through a WSN solution,

provided that current WSN implementations can be extended to integrate key optical functionalities.

The concept of the optical sensor mote follows on from these observations: a sensor mote that integrates optical sensing as its primary sensing mechanism. The important characteristics necessary for the optical sensor mote to be a practical solution have been outlined: small form factor, ease of mass production and low cost, ability to communicate with other motes using RF technology (which is critical for cost effective deployment over a wide area), and signal processing capabilities.

The practical approach to realizing the optical sensor mote centres on the hybrid integration of integrated optics and electronics technologies on the same chip and wafer [Rubenstein et al. 2011; Wada 2008]. The key is to utilize the inherent strengths of electronics for RF communication, storage, and signal processing with the inherent strengths of integrated optics for sensing into a single sensor mote; the so-called wireless enabled optical sensor mote.

To demonstrate the viability of such a sensor mote, its two key components, the RF communication, and the optical sensing, must be experimentally demonstrated in a manner that is compatible with their eventual integration into a single device.

A WSN prototype based on the ZigBee communication protocol was demonstrated. The function of the WSN is to monitor and maintain the temperature of an environment. The prototype was built using commercial low power, low cost, and

small form factor sensor nodes. This WSN prototype serves as a practical demonstration of the communication element of the proposed ***optical sensor mote***.

Photonic crystal structures have received much research attention, the core advantage being their enhanced waveguding performance. Indeed they have been harnessed to yield a number of highly efficient and highly compact optical devices. The hypothesis was that same advantage forms the basis for multi-gas sensors. Further their potential small form factor is directly compatible with the concept of the optical sensor mote. Thus the remainder of the Thesis presents a series of theoretical and experimental investigations of photonic crystal gas sensor approaches.

A multi-gas sensors design based on SOI photonic crystal resonant L3 cavities has been proposed and theoretically analysed. Simulation indicates the promise of sensitivities as high as 3000 nm/RIU. The sensor design has the potential capability to sense multiple gases without the need for any physical adjustment (e.g. additional filters or input sources or chemical agents). The production run for these prototype sensors failed however, due to fabrication errors and the experimental validation of these sensors was not possible. Similar sensors (but single gas) have been demonstrated in literature.

A class of photonic crystal sensors referred to as slow light refractive index based sensors was proposed and the viability of which was theoretically and experimentally demonstrated. The sensors were theoretically and experimentally evaluated in InP and theoretically demonstrated in SOI., The successful use of the photonic crystal's

slow light mode to sense different gases was demonstrated for the first time. The InP sensors had a theoretical sensitivity of 211 nm/RIU) and experimental sensitivity of 190 nm/RIU (but based on a limited set of data points) for samples with r = 0.24a = 106 nm and theoretical sensitivity of 150 nm/RIU for samples with r = 0.20a = 90 nm.

The slow light based sensors exhibit superior performance in SOI compared to their InP counterparts due to the higher refractive index contrast afforded by the former material system. The SOI sensors had a theoretical sensitivity of 246 nm/RIU compared to 211 nm/RIU for InP. However, the drawback of such sensors lies in the difficulty of integrating them with the broadband laser source, most likely fabricated using InP. Furthermore, the viability of InP sensors themselves to effectively sense gases using refractive index based methods was initially proven (including SF6).

The photonic crystal multi-gas sensors serve to demonstrate the sensing element of the proposed optical sensor mote. They are of a small form factor, stable, and functional. Fabricated in either SOI and InP allows their integration with digital, RF, and power electronics on the substrate to facilitate the wireless enabled optical sensor mote. This is viewed as currently feasible given the significant and recent advances in hybrid integration of SOI, InP, and CMOS technologies [Dahlem et al. 2011; Mathine 1997; Reckziegel et al. 2008; Reisinger et al. 2002].

.

The research has contributed to the understanding of the feasibility of two key components of the ***optical sensor mote.*** Preliminary results on the sensing interaction are such that they contribute know how to the roadmap which aims to integrate multiple functions – electronic and optical – on a single material system..

4.2 Outlook and Future work

A significant amount of work remains before the demonstration of a wireless enabled optical sensor mote becomes a reality. Even though two key components have been demonstrated; WSN enabled communication and optical sensing, challenges remain in combining them into a single device. There is a great deal of research interest in the integration of electronics and optical components on a single chip. Many practical realizations have already been demonstrated and commercial applications exist. This is an important area of future work.

The experimental demonstration of SOI photonic crystal multi gas sensors based on the resonant cavities (L3) was not completed satisfactorily due to problems in fabrication. Although similar (but single gas) devices have been demonstrated this is a fruitful area of research.

Extension of the preliminary research in SOI photonic crystal waveguide slow light gas sensors is of great interest given the promising theoretical results. A rigorous experimental programme that characterises the performance of this class of sensors is a significant research topic. This is also a research opportunity for InP

implementations. The initial results presented require further corroboration under a more extensive experimental programme.

Finally, a more efficient design for photonic crystals that optimizes the slow light mode is needed to enhance the performance of this family of sensors..

References

Akahane et al. 2003 Y. Akahane, T. Asano, B. Song, S. Noda, “High-Q photonic nanocavity in a two-dimensional photonic crystal”, Nature, 425, 2003, pp. 944-947.

Ashcroft and Mermin 1976 N. W. Ashcroft and N. D. Mermin, "Solid State Physics", Holt Saunders, Philadelphia, 1976

Awad 2006 Hazem Awad, “Competitive optics circuits for all-optical signal-processing applications”, Masters Dissertation, 2006, University of Ottawa.

Awad et al. 2010 Hazem Awad et al., "Wireless enabled multi gas sensor system based on photonic crystals", Proceeding of SPIE, Vol. 7726, 2010.

Awad et al. 2011 Hazem Awad et al., “Gas Sensing using Slow Light in Photonic Crystal Waveguides”, 7th workshop on Fibre and Optical Passive Components (WFOPC), Montreal, Canada, 2011, pp. 1-3.

Baba 2008 T. Baba, “Slow light in photonic crystals”, Nature Photonics, Vol. 2, 2008, pp. 465-473.

Bandyopadhyay et al 2009 L. K. Bandyopadhyay et al., “Wireless information and safety system for mines”, Journal of scientific & industrial research, Vol. 68, 2009, pp. 107-117.

Benini et al. 2006 L. Benini, E. Farella, and C. Guiducci, “Wireless sensor networks: Enabling technology for ambient intelligence”, Microelectronics Journal, Vol. 17, Issue 12, 2006, pp. 1639-1649.

Benson et al. 2006 T. M. Benson, et al., “Micro-optical resonators for microlasers and integrated optoelectronics”, Frontiers in Planar Lightwave Circuit Technology: NATO Science Series, Vol. 216, 2006, pp. 39-70.

Bogaerts et al. 2006 W. Bogaerts et al., “Compact wavelength-selective functions in silicon-on-insulator photonic wires,” IEEE Journal of Selected Topics in Quantum Electronics, vol. 12, Issue 6, 2006.

Buswell et al. 2008 S. C. Buswell et al., "Specific detection of proteins using photonic crystal waveguides", Optics Express, Vol. 16, Issue 20, 2008, pp. 15949-15957.

Chakravarty et al. 2011 Swapnajit Chakravarty et al., "Silicon-nanomembrane-based photonic crystal nanostructures for chip-integrated open sensor systems", (invited paper) Proceeding of SPIE, Vol. 8198, International Conference on Optical Instruments and Technology, 2011.

Chakravarty et al. 2012 S. Chakravarty et al., "Slow light engineering for high Q high sensitivity photonic crystal microcavity biosensors in silicon", Biosensors and Bioelectronics, Vol. 38, Issue 1, 2012, pp. 170–176.

Chalcraft et al. 2007 A. R. A. Chalcraft et. al., “Mode structure of the L3 photonic crystal cavity”, Applied Physics letters, Vol. 90, Issue 24, 2007.

Chrostowski et al. 2010 L. Chrostowski et al., “Silicon Nanophotonics Fabrication: An innovative graduate course”, (invited paper) Proceeding of IEEE 17th International Conference on Telecommunications, Doha, 2010, pp. 544-551.

Coal Mines www.lifeslittlemysteries.com/446-why-do-coal-mines-explode.html

Dahdah 2010 Jean Dahdah, "Analysis of a photonic crystal cavity based on absorbent layer for sensing applications", Optical Society of America B, Vol. 27, No. 2. 2010 pp. 305-310.

Dahlem et al. 2011 M.S. Dahlem et al., “Electronic-photonic integrated circuits in silicon-on-insulator platforms”, Proceeding of the XXXth General Assembly and Scientific Symposium (URSI), Istanbul, Turkey, 2011, pp. 1.

Deotare et al. 2009 Parag B. Detoare et al., " High quality factor photonic crystal nanobeam cavities", Applied Physics Letters, Vol. 94, Issue 12, 2009.

Dorfner et al. 2008 D. Dorfner et al., "Silicon photonic crystal nanostructures for refractive index sensing", Applied Physics Letters, Vol. 93, Issue 18, 2008.

Dorfner et al. 2009 D. Dorfner et al., "Photonic crystal nanostructures for optical biosensing applications", Biosensors and Bioelectronics, Vol. 24, Issue 12, 2009, pp. 3688–3692.

Falco et al. 2008 A. Di Falco, et al., "Slotted Photonic Crystal waveguides and cavities for slow light and sensing applications", 5th IEEE International Conference on Group IV Photonics, 2008, pp. 228- 230.

Falco et al. 2009 A. Di Falco et al., "Chemical sensing in slotted photonic crystal heterostructure cavities", Applied Physics Letters, Vol. 94, Issue 6, 2009.

Fan and White 2011 Xudong Fan and Ian M. White, "Optofluidic microsystems for chemical and biological analysis", Nature, Vol. 5, pp. 591-597.

Feng and Jiangfeng 2010 C. Feng and S. Jiangfeng, “Study on Wireless Gas Sensor”, Proceedings of the Third International Symposium on Electronic Commerce and Security Workshops (ISECS ’10) Guangzhou, China, 2010, pp. 380-382.

Figotin and Vitebskiy 2006 A. Figotin, I. Vitebskiy, “Slow light in photonic crystals”, Waves in Random and Complex Media, Vol. 16, Issue 3, 2006, pp. 293-382.

FSM http://en.wikipedia.org/wiki/Finite-state_machine

Galisteo-López et al. 2007 J. F. Galisteo-López et al., "Slow to superluminal light waves in thin 3D photonic crystals,", Optics Express, Vol. 15, 2007, pp. 15342-15350.

Gas Refractive Index www.kayelaby.npl.co.uk/general_physics/2_5/2_5_7.html

Giancarlo et al. 2009 Editors C. Giancarlo et al., "An introduction of optoelectronic sensors, series in optics and photonics – vol. 7", World scientific publishing company, 2009.

Hall 2009a Trevor J. Hall, Private communication, 2009.

Hall 2009b Trevor J. Hall, Private communication, 2009.

Halloua et al. 2009 Y. Halloua et al., "Hybrid InP-based photonic crystal lasers on silicon on insulator wires", Applied Physics Letters, vol. 95, 2009.

Hammer and Ivanova 2009 M. Hammer, O. V. Ivanova, "Effective index approximations of photonic crystal slabs: a 2-to-1-D assessment", Optical and Quantum Electronics, Vol. 41, Number 4, 2009, pp. 267-283.

Han et al. 2011 Z. Han, X. Checoury, L. Haret, P. Bouchard, "High quality factor in a two-dimensional photonic crystal cavity on silicon-on-insulator", Optics Letters, Vol. 36, No. 10, pp. 1749-1751.

Haus 1985 H. A. Haus, "Waves and fields in Optoelectronics", Prentice-Hall, Englewood Cliff, USA, 1985.

Heatley et al. 1998 D. J. T. Heatley, et al., "Optical wireless: the story so far", IEEE Communications Magazine, Vol. 36, Issue 12, 1998, pp. 72-74, 79-82.

Hosseinibalam et al. 2012 F. Hosseinibalam et al., "Design of an optofluidic biosensor using the slow-light effect in photonic crystal structures", Applied Optics, Vol. 51, Issue 5, 2012, pp. 568-576.

IAR EW http://www.iar.com/en/Products/IAR-Embedded-Workbench/8051/

IAR vSTATE www.iar.com/en/Products/IAR-visualSTATE

Jágerská et al. 2010 J. Jágerská et. al., "Refractive Index Gas Sensing in a Hollow Photonic Crystal Cavity", 12th International Conference on Transparent Optical Networks (ICTON), Germany, 2010, pp. 1-4.

Jágerská et al. 2010b Jana Jágerská et al., "Refractive index sensing with an Air-slot photonic crystal nanocavity", Optics Letters, Vol. 35, No. 15, 2010, pp. 2523-2525.

Jamois et al. 2002 C. Jamois et al., "Silicon-Based Photonic Crystal Slabs: Two Concepts", IEEE Journal of Quantum Electronics, Vol. 38, Issue 7, 2002, pp. 805-810.

Jensen et al. 2008 K.H. Jensen , M.N. Alam , B. Scherer , A. Lambrecht , N.A. Mortensen, "Slow-light enhanced light–matter interactions with applications to gas sensing", Optics Communications, Vol. 281, 2008, pp. 5335–5339.

Joannopoulos et al. 2008 John D. Joannopoulos et al., "Photonic Crystals, Molding the flow of light", 2nd Ed, Princeton university press, 2008.

Johnson et al. 1999 Steven G. Johnson et al., "Guided modes in photonic crystal slabs", Physical Review B, Vol. 60, No. 8, 1999, pp. 5751-5758.

Kang et al. 2010 Christopher Kang et al., "Photonic crystal slab sensor with enhanced surface area", Optics Express, Vol. 18, Issue 26, 2010, pp. 27930-27937

Karnutsch et al. 2009 Christian Karnutsch et al. "Temperature stabilization of optofluidic photonic crystal cavities", Applied Physics Letters, Vol. 94, Issue 23, 2009.

Katz et al. 2006 G. Katz et al., "Cellular over optical wireless networks", IEE Proc.-Optoelectron., Vol. 153, No. 4, 2006, pp. 195-198.

Kicken et al. 2008 H.H.J.E. Kicken, et al., "Fabrication, measurement and tuning of a photonic crystal H1-cavity in deeply etched InP/InGaAsP/InP", Proceeding of International Conference on Indium Phosphide and Related Materials (IPRM), Versailles, 2008, pp. 1-4.

Kotlyar et al. 2004 M. V. Kotlyar et al., "Low-loss photonic crystal defect waveguides in InP", Applied Physics Letters, Vol. 84, 2004.

Krauss 2007 T. F. Krauss, "Slow light in photonic crystal waveguides", Journal of Physics D: Applied Physics, Vol. 40, No. 9, 2007, pp. 2666-2670.

Kumar et al. 2012 Arun Kumar et al., "Wide Range Temperature Sensors Based on One-Dimensional Photonic Crystal with a Single Defect",
International Journal of Microwave Science and Technology, Vol. 2012, 2012.

Lambrecht et al. 2007 A. Lambrech et al., "Miniature infrared gas sensors using photonic crystals", Proceeding of SPIE, Vol. 6480, 2007.

Lai et al. 2011 Wei-Cheng Lai et al., "On-chip methane sensing by near-IR absorption signatures in a photonic crystal slot waveguide", Optics Letters, Vol. 36, No. 6, 2011, pp. 984-986.

Laser Cleave www.cmc.ca/whatweoffer/make/lasercleaving.aspx

Lee and Fauchet 2007 Mindy R. Lee and Philippe M. Fauchet, "Nanoscale microcavity sensor for single particle detection" , Optics Letters, Vol., No. 22, 2007, pp. 3284-3286.

Li Junhua et al. 2011 Li Junhua et al., "Design of a photonic crystal microcavity for biosensing", Journal of Semiconductors, Vol. 32, No. 3, 2011.

Lin et al. 2012 Hongtao Lin et al., "Double resonance 1-D photonic crystal cavities for single-molecule mid-infrared photothermal spectroscopy: theory and design", Optics Letters, Vol. 37, No. 8, 2012, pp. 1304-1306.

Liu et al 2009a T. Liu et al., "Hazard monitoring in mines using fiber optic sensors", S&A IOP and OFS-20, Edinburgh, 2009.

Liu et al. 2009b T. Liu et al., "Fibre optic sensors for mine hazard detection", Journal of Physics: Conference Series 178, 2009.

Liu and **Salemink 2012** Y. Liu and H. W. M. Salemink, "Photonic crystal-based all-optical on-chip sensor", Vol. 20, No. 18, Optics Express, Vol. 20, Issue 18, 2012, pp. 19912-19920.

Mathine 1997 D. L. Mathine, "The integration of III-V optoelectronics with silicon circuitry", IEEE Journal of Selected Topics in Quantum Electronics, Vol. 3, Issue 3, 1997, pp. 952-959.

Mining http://en.wikipedia.org/wiki/Mining

Mnaymneh 2003 K. Mnaymneh, "A Theoretical Investigation of a Dual Beam Holographic Lithography Method for the Fabrication of Omnidirectional Photonic Crystals", Masters Thesis Dissertation, Carleton University, 2003.

Mnaymneh 2009 K. Mnaymneh, Private Communication.

Mnaymneh 2011 K. Mnaymneh, Private Communication.

Moseley 1997 P. Moseley, “Solid state gas sensors”, Meas. Sci. Technol. Vol. 8, 1997, pp. 223-237.

MPB http://ab-initio.mit.edu/wiki/index.php/MIT_Photonic_Bands

NAir and Vijaya 2010 R. V. NAir, R. Vijaya, "Photonic crystal sensors: An overview", Progress in Quantum Electronics, Vol. 34, Issue 3, 2010, pp. 89–134.

Niu et al. 2007 X. Niu et al., “The Design and Evaluation of a Wireless Sensor network for mine safety monitoring”, Proceedings of the 2007 IEEE GLOBECOM, 2007, pp. 1291-1294.

Passaro 2013 Editor V. M. N. Passaro, “Advances in Photonic Crystals”, InTech publishing, 2013.

Passaro et al. 2012a V. M. N. Passaro et al., "Recent Advances in Integrated Photonic Sensors", Sensors, Vol. 12, Issue 11, pp. 15558-15598.

Passaro et al. 2012b V. M. N. Passaro et al., "Photonic structures based on slot waveguides for nanosensors: state of the art and future developments", International Journal of Research and Reviews in Applied Sciences Vol. 11, Issue 3, 2012, pp. 402-418.

Passaro et al. 2012c V. M. N. Passaro et al., "A generalized approach for design of photonic gas sensors based on Vernier-effect in mid-IR", Sensors and Actuators B: Chemical, Vol. 168, 2012, pp. 402-420.

Passaro et al. 2013 V. M. N. Passaro et al., "Photonic resonant microcavities for chemical and biochemical sensing", Royal Chemical Society (RSC) Advances, Vol. 3 Issue 1, 2013, pp. 25-44.

Pavesi and Guillot 2006 L. Pavesi and G. Guillot, “Optical Interconnects: The Silicon Approach”, Springer Berlin, Heidelberg, 2006.

Pergande et al. 2011 D. Pergande et al., “Miniature infrared gas sensors using photonic crystals,” Journal of Applied Physics, Vol. 109, Issue 8, 2011.

PRN 2013a http://www.prweb.com/releases/photonic-crystal-market/component-and-module/prweb10459096.htm

PRN 2013b http://www.prnewswire.com/news-releases-test/global-markets-and-technologies-for-photonic-crystals----focus-on-the-americas-197302151.html

Qiu 2001 Min Qiu "Analysis of guided modes in photonic crystal fibers using the finite-difference time-domain method", Microwave and Optical Technology letters, Vol. 30, Issue 5, 2001, pp. 327–330

Qiu et al. 2007 W. Qiu et al., “An efficient self-healing process for ZigBee sensor networks”, International Symposium on Communications and Information Technologies (ISCIT ’07), Sydney, Australia, 2007, pp. 1389-1394.

OptoSniff http://www.optosci.com/Gas_Sensing/pdf/mt-05.pdf

Reckziegel et al. 2008 Sven Reckziegel et al, “Optoelectronic chips integrate emitters and sensors”, SPIE, 2008, http://spie.org/x25476.xml?ArticleID=x25476

Ralf Luckluma et al 2012 Ralf Luckluma et al., "Two-dimensional phononic crystal sensor based on a cavity mode", Sensors and Actuators B Vols. 171– 172, 2012, pp. 271– 277.

RefIndex 1 http://refractiveindex.info/

RefIndex 2 http://www.kayelaby.npl.co.uk/general_physics/2_5/2_5_7.html

RefIndex 3 http://www.guidechem.com/reference/dic-10664.html

Reisinger et al. 2002 Alex Reisinger et al. “Hybrid integration: Production ready”, EE Times, 2002, http://www.eetimes.com/story/OEG20020214S0037

Rindorf and Bang 2008 Lars Rindorf and Ole Bang, "Sensitivity of photonic crystal fiber grating sensors: biosensing, refractive index, strain, and temperature sensing", JOSA B, Vol. 25, Issue 3, 2008, pp. 310-324.

Robinson et al. 2008 J. Robinson, L. Chen, M. Lipson, "On-chip gas detection in silicon optical microcavities", Optics Express, Vol. 16, No. 6, 2008, pp. 4296-4301.

Roelkens et al. 2007 G. Roelkens, D. Van Thourhout, R. Baets, "High efficiency grating coupler between silicon-on-insulator waveguides and perfectly vertical optical fibers", Optics Letters, Vol. 32, No. 11, 2007, pp. 1495-1497.

Rubenstein et al. 2011 R. Rubenstein et al., "Photonic integration: Bent on disruption", www.totaltele.com/view.aspx?ID=451866, 2011

Ruperez et al. 2010 Jamie Garcia-Ruperez et al. "Label-free antibody detection using band edge fringes in SOI planar photonic crystal waveguides in the slow-light regime", Optics Express, Vol. 18, Issue 23, 2010, pp. 24276-24286

Schulz et al. 2010 S. A. Schulz et al., "Dispersion engineered slow light in photonic crystals: a comparison", Journal of Optics, Vol. 12, No. 10, 2010.

Scullion et al. 2011 M.G. Scullion et al., "Slotted photonic crystal cavities with integrated microfluidics for biosensing applications", Biosensors and Bioelectronics, Vol. 27, 2011, pp. 101– 105.

Sensor Mote a www.pcmag.com/encyclopedia_term/0,2542,t=mote&i=47249,00.asp

Sensor Mote b webs.cs.berkeley.edu/papers/hotchips-2004-motes.ppt

Sensor Mote c www.cise.ufl.edu/~helmy/cis6930/mote.ppt

Sensor Mote d http://en.wikipedia.org/wiki/Sensor_node

Shi et al. 2004 Shouyuan Shi et al., "Plane-wave expansion method for calculating band structure of photonic crystal slabs with perfectly matched layers", J. Opt. Soc. Am. A, Vol. 21, No. 9, 2004, pp. 1769-1775

Shinya, et al. 2002 A. Shinya et al., "Two-dimensional Si photonic crystals on oxide using SOI substrate", Optical and Quantum Electronics, Vol. 34, 2002, pp. 113-121.

Solli et al. 2003 D.R. Solli et al., "Experimental observation of superluminal group velocities in bulk two-dimensional photonic bandgap crystals", IEEE Journal of Selected Topics in Quantum Electronics, Vol. 9, Issue 1, 2003, pp. 40-42.

Sünner, et al. 2008 T. Sünner, et al., "Photonic crystal cavity based gas sensor", Applied Physics Letters, Vol. 92, Issue 26, 2008.

Sullivan 2000 D. M. Sullivan, "Electromagnetic Simulation Using the FDTD Method", Wiley-IEEE Press, USA, 2000.

Takano et al. 2006 H. Takano et al., "Highly efficient multi-channel drop filter in a two-dimensional hetero photonic crystal", Optics express, Vol. 14, No. 8, 2006, pp. 3491-3496.

TI CC2430 www.ti.com/lit/ds/symlink/cc2430.pdf

TI DN102 www.ti.com/lit/an/swra101a/swra101a.pdf

TI Z-Stack www.ti.com/tool/z-stack

Thorlabs http://www.thorlabs.com/newgrouppage9.cfm?objectgroup_id=1340

Tümer and Gündüz 2010 A. E. Tümer and M. Gündüz, "Design of a methane monitoring system based on wireless sensor networks", Scientific Research and Essays, Vol. 5, No. 8, 2010, pp. 799-805.

Vahala 2003 K. J. Vahala, "Optical Microcavities", Nature, Vol. 424, 2003, pp. 839-846.

Vertical Coupler 1 http://photonics.intec.ugent.be/research/topics.asp?ID=8

Vertical Coupler 2 http://photonics.intec.ugent.be/download/ocs75.pdf

Vertical Coupler 3 http://photonics.intec.ugent.be/download/pub_2811.pdf

Wada 2008 Kazumi Wada, "A new approach of Electronics and Photonics Convergence on Si CMOS Platform: How to Reduce Device Diversity of Photonics for Integration", Advances in Optical Technologies, Vol. 2008, hindawi.com/journals/aot/2008/807457

Wang et al. 2007 X. Wang et al., "Deploying a Wireless Sensor Network on the coal mines", Proceedings of the 2007 IEEE International Conference on Networking, Sensing and Control, London, UK, 2007, pp. 324-328.

Wang et al. 2008 X. Wang, Z. Xu, N. Lu, J. Zhu, G. Jin, "Ultracompact refractive index sensor based on microcavity in the sandwiched photonic crystal waveguide structure", Optics communication, Vol. 208, 2008, pp. 1725-1731.

Wang et al. 2010 Bowen Wang et al., "Photonic crystal slot nanobeam slow light waveguides for refractive index sensing", Applied Physics Letters, Vol. 97, Issue 15, 2010.

Wehrspohn 2005 R.B. Wehrspohn, "Applications of silicon-based photonic crystals", 2nd IEEE International conference on Group IV Photonics, 2005, pp. 39-41.

Wehrspohn et al. 2005 R. Wehrspohn et al., "Photonic crystal gas sensors", Proceedings of SPIE 5855, 2005, pp. 24-29.

White et al. 2008 T. P. White et al. "Silica-embedded silicon photonic crystal waveguides", Optics Express, Vol. 16, No. 21, 2008. pp. 17076-17081.

Winick 1992 K. A. Winick, “Effective-index method and couple-mode theory for almost-periodic waveguide gratings: a comparison”, Applied Optics, Vol. 31, Issue 6, 1992, pp. 757-764.

Wolinski et al. 2008 T.R. Wolinski et al., "Photonic Liquid Crystal Fibers for Sensing Applications", IEEE Transactions on Instrumentation and Measurement, Vol. 57, Issue 8, 2008, pp. 1796-1802.

WSN Applications a http://en.wikipedia.org/wiki/Wireless_sensor_network

WSN Applications b http://arri.uta.edu/acs/networks/WirelessSensorNetChap04.pdf

Xianli et al. 2011 Q. Xianli et al., “Coal Mine Gas Wireless Monitoring System Based on WSNs”, Second international conference on Digitial manufacturing and automation (ICDMA ’11), Zhangjiajie, Hunan, 2011, pp. 309-312.

Yamazoe 2005 N. Yamazoe, “Toward innovations of gas sensor technology”, Sensors and Actuators B, Vol. 108, 2005, pp. 2-14.

Yokogawa http://tmi.yokogawa.com/products/optical-measuring-instruments/optical-spectrum-analyzer/aq6370c-optical-spectrum-analyzer/

Zaho et al. 2011 Yong Zaho et al., "Research advances of photonic crystal gas and liquid sensors", Sensors and Actuators B, Vol. 160, Issue 1, 2011, pp. 1288-1297.

Zaho et al. 2012 Yong Zaho et al., "High sensitivity gas sensing method based on slow light in photonic crystal waveguide", Sensors and Actuators B, Vol. 173, 2012, pp. 28– 31.

Zhang et al. 2012 Ya-Nan Zhang et al., "Theoretical research on high sensitivity gas sensor due to slow light in slotted photonic crystal waveguide", Sensors and Actuators B, Vol. 173, 2012, pp. 505-509.

ZigBee http://en.wikipedia.org/wiki/ZigBee

ZigBee a http://www.zigbee.org/